

Magnus Moe Wahl

Rate Effects Increasing Lateral Capacity of Monopiles

Based on Spudcan Penetration Tests

Master's thesis in Civil and Environmental Engineering

Supervisor: Gudmund Eiksund

Co-supervisor: Pauline Suzuki

June 2021

Magnus Moe Wahl

Rate Effects Increasing Lateral Capacity of Monopiles

Based on Spudcan Penetration Tests

Master's thesis in Civil and Environmental Engineering
Supervisor: Gudmund Eiksund
Co-supervisor: Pauline Suzuki
June 2021

Norwegian University of Science and Technology
Faculty of Engineering
Department of Civil and Environmental Engineering



Norwegian University of
Science and Technology

Preface

This Master thesis in geotechnics is written as a part of the MSc program in Civil and Environmental Engineering at the Norwegian University of Science and Technology (NTNU). This thesis is written during the spring semester of 2021, and the extent of the work is 30 credits. This study is a continuation of a project thesis which served a preliminary study for the current master thesis. The topic of the project thesis was spudcan penetration at Dogger Bank.

The topic of the current thesis was proposed by DNV and Equinor, and the thesis is written in collaboration with DNV. Pauline Suzuki at DNV has served as external supervisor for the project, and has provided guidance through regular meetings during the semester. Necessary data has been provided by Tor Inge Tjelta at Equinor.

Trondheim, 2021-06-24

A handwritten signature in dark ink, reading "Magnus M. Wahl". The signature is written in a cursive style with a large initial 'M'.

Magnus Moe Wahl

Acknowledgment

I would like to thank my main supervisors Prof. Gudmund Eiksund and Pauline Suzuki for their continued support and guidance during this work, and for sharing their broad geotechnical knowledge with me. I also want to thank Tor Inge Tjelta for providing insight into and data from the Dogger Bank project.

I would like to express my deep gratitude towards Miguel Costas and Khoa D.V. Huynh for providing assistance beyond what could be expected. Without their help with finite element modelling, this work would not have been possible. Especially, I thank Khoa for providing the subroutine for the material model, and Miguel for sharing his workstation with me.

I want to thank Pauline Suzuki for valuable help during the writing process, and Jan Holme and Elin Linnerud Onstad for reviewing my thesis.

Magnus M. Wahl

Abstract

Large diameter monopiles are a common foundation type for offshore wind turbines. Monopile lateral capacity has become an increasingly important field of research with the growth of the offshore wind industry to provide sufficient lateral resistance against wind and wave loads transferred from the wind turbine structure. This thesis investigates if rate effects can increase the lateral capacity of monopiles in clay, as suggested by recent research.

This study has considered monopiles at the Dogger Bank Wind Farm located off the coast of England in the North Sea. The site is known to be difficult to characterise due to its complex depositional history and geological processes. Laboratory tests have shown large scatter in strength measurements, particularly in the Dogger Bank Clay units. To better understand the strength properties of the complex Dogger Bank soil, penetration tests with large spudcan foundations were performed by the wind farm developer. The spudcan tests were performed with different penetration rates, making it possible to study the effect of loading rate in Dogger Bank clay.

In this study, the spudcan tests were back-calculated using finite element analyses with the coupled Eulerian-Lagrangian method to describe large deformations, and with a soil model capable of describing strain softening and rate effects. The back-calculations were used to calibrate the rate and softening parameters of the material model, and the back-calculations gave results in reasonable agreement with measurements from the penetration tests. The rate effect parameters were verified by finite element (FE) modelling of a triaxial test. In addition, the triaxial FE model was used to study the behaviour of softening and rate effects in the material model.

The back-calculated rate effect parameters were used to study the effect of loading rate on monopile capacity in the ultimate limit state with FE-analyses. The analyses consisted of an embedded monopile which was pushed over at different rates while recording the resistance from the soil. The dimensions of the monopile, soil conditions and loading case were chosen to be representative for the Dogger Bank Wind Farm. The analyses showed a significant increase in lateral resistance due to rate effects for the considered ultimate limit state case, but also for lower loading rates. This indicates that monopile lateral capacity can be significantly increased when accounting for loading rate effects. This may be used to optimise monopile design and give significant financial savings for an offshore wind project.

Sammendrag

Monopeler er peler med stor diameter, og er en vanlig fundamenttype for offshore vindturbiner. Sideveis kapasitet av monopeler har blitt et stadig viktigere forskningsfelt med veksten av havvindindustrien for å gi tilstrekkelig sideveis kapasitet mot vind- og bølgelaster overført fra vindturbinstrukturen. Denne masteroppgaven undersøker om hastighetseffekter ("rate effects") kan øke sidevis kapasitet av monopeler i leire, som antydnet i nyere forskning.

Denne studien har vurdert monopeler fra havvindparken på Dogger Bank som ligger utenfor kysten av England i Nordsjøen. Jordforholdene i området er kjent for å være vanskelige å beskrive på grunn av områdets kompliserte avsetningshistorie og geologiske prosesser. Laboratorietester har vist stor spredning i styrkemålinger, spesielt for Dogger Bank-leire. For å forstå styrkeegenskapene til den komplekse jorden på Dogger Bank bedre, ble det utført penetrasjonstester med store spudcan-fundamenter av vindparkutbyggeren. Spudcan-testene ble utført med forskjellige penetrasjonshastigheter, noe som gjør det mulig å studere effekten av belastningshastighet for Dogger Bank-leire.

I denne studien ble Spudcan-testene tilbakeregnet ved bruk av elementanalyser med den koblede Eulerske-Lagrangiske metode for å beskrive store deformasjoner, og med en jordmodell som kan beskrive "strain softening"- og tøyningshastighetseffekter. Tilbakeregningene ble brukt til å kalibrere tøyningshastighet- og "softening"-parametere for materialmodellen, og ga resultater i akseptabel overensstemmelse med målinger fra penetrasjonstestene. Parameterne for hastighetseffekten ble validert med elementmodellering av en treaksial test. I tillegg ble elementmodellen for treaksial testen brukt til å undersøke "softening"- og hastighetseffekter i materialmodellen.

De tilbakeregnete parameterne for hastighetseffekt ble brukt til å undersøke effekten av belastningshastighet på monopelkapasitet i bruddgrensetilstanden med elementanalyser. Analysene besto av en monopel som er satt ned i sjøbunnen og som blir dyttet sideveis med forskjellige hastigheter, mens mostanden fra jorden blir målt. Monopelens dimensjoner, jordforhold og lastsituasjon ble valgt slik at de er representative for Dogger Bank havvindpark. Analysene viste en betydelig økning i sideveis kapasitet på grunn av hastighetseffekter for den betraktede bruddgrensetilstanden, men også for lavere belastningshastigheter. Dette indikerer at sideveis kapasitet av monopeler kan økes betraktelig hvis hastighetseffekter tas hensyn til. Dette kan brukes til å optimalisere dimensjonene til monopeler og gi betydelige økonomiske besparelser for et havvindprosjekt.

Contents

Preface	i
Acknowledgment	ii
Abstract	iii
Sammendrag	iv
1 Introduction	1
1.1 Background	1
1.2 Short Literature Review	2
1.3 Problem Formulation	3
1.4 Approach	4
1.5 Limitations	5
1.6 Report Structure	5
1.7 Citation from Project Thesis	6
2 Literature Review and Theory	7
2.1 Dogger Bank	7
2.2 Scale effects	9
2.3 Triaxial Test	12
2.4 Strain Rate and Softening Effects	13
2.5 Spudcan Penetration in Clay	19
2.6 Finite Element Analysis	22
2.7 Lateral capacity of Monopiles and Rate Effects	28
3 Triaxial model	32
3.1 FE-model for Triaxial Test and Model Verification	32
3.2 Triaxial Model - Soil Model Verification	37
3.3 Triaxial Model - Conclusion	43
4 Back Calculation of Spudcan Penetration	44
4.1 Dogger Bank Jacking Trials 2020	44
4.2 Geotechnical Design Parameters	47
4.3 Finite Element Model	53
4.4 Convergence Study	55
4.5 Spudcan Back-Calculation	63
4.6 Discussion of Spudcan Back-calculations	76
4.7 Summary of Back-Calculation	82
5 Rate Effects on Monopile Capacity	84
5.1 Problem Formulation	84
5.2 Comparison of Spudcan and Monopile Failure Mechanism	85

5.3 Monopile Finite Element Model	86
5.4 Geotechnical Parameters for Monopile Analysis	89
5.5 Monopile Analysis and Results	91
5.6 Discussion of Monopile Analyses	97
5.7 Summary of Monopile Analyses	101
6 Summary and Further Work	103
6.1 Thesis Summary	103
6.2 Recommendations for Further Work	105
Bibliography	108
A Spudcan Drawing	112
B Soil Data	114
s_u - and q_t -profiles	
C Miscellaneous Plots	117
Filtered and unfiltered response	
Monopile initial stresses	

List of symbols

Latin

Symbol	Explanation
A	maximum cross-sectional spudcan bearing area
A	cross-sectional area of triaxial sample
B_S	buoyancy of spudcan below bearing area, i.e. the submerged weight of soil displaced by the spudcan below D
D	depth of maximum spudcan bearing area
D_{eq}	equivalent spudcan diameter
D_p	pile diameter
D_s	soil sample diameter in triaxial test
d_c	depth factor
E	modulus of elasticity
F	compression force in triaxial test
F	external force applied to a degree of freedom
f_{rate}	factor accounting for rate effects in soil model
f_{rate}^{max}	cap for rate effects in soil model
f_{soft}	factor accounting for softening effects in soil model
H	height of soil domain in finite element model
H_{cav}	limiting depth of cavity that remains open above the spudcan during penetration
I	internal force applied to a degree of freedom
K'_0	coefficient of lateral earth pressure at rest [= $\sigma'_{h0}/\sigma'_{v0}$]
L	embedded pile length
L_0	initial sample height
ΔL	change in sample height
M	Mass matrix
N_c	bearing capacity factor
N_{kt}	empirical cone factor for undrained shear strength
N_{kt}^*	empirical cone factor for operational undrained shear strength
n	filter order for the Butterworth filter
p	mobilised earth pressure per unit length of pile
Q_V	gross ultimate vertical bearing capacity of a foundation in clay
q	deviator stress [= $\sigma_1 - \sigma_3$]
q_t	corrected cone resistance
R	radius of soil domain in finite element model
S_t	soil sensitivity [= $s_u/s_{u,r}$]
s_c	shape factor
s_u	undrained shear strength
s_{uH}	undrained shear strength at the ultimate cavity depth

Symbol	Explanation
s_u^{max}	maximum undrained shear strength in a soil profile
$s_{u,r}$	undrained shear strength of remoulded soil
$s_{u,rate}$	mobilised shear strength due to strain rate effects
$s_{u,ref}$	reference shear strength at the reference shear strain rate before softening
T	wave time period
t	time
Δt	time increment
u	displacement in a degree of freedom
\dot{u}, \ddot{u}	velocity and acceleration in a degree of freedom
V_L	structural available spudcan reaction
v	spudcan penetration rate
v_a	loading rate or velocity in finite element analysis
v_n	normalised loading rate or velocity
v_c	compression velocity triaxial test
W_{BF}	submerged weight of backfill
y	lateral pile displacement
z	depth below sea floor

Greek

Symbol	Explanation
β	shear-thinning index
$\dot{\gamma}$	maximum shear strain rate
$\dot{\gamma}_{\text{ref}}$	reference shear strain rate
γ, γ'	total and effective unit weight of soil
Δ	change in
Δt	time increment
δ_{rem}	ratio of intact and remoulded shear strength (inverse sensitivity)
$\varepsilon_1, \varepsilon_3$	major and minor principal strain
ε_a	axial strain
η	viscous property
μ	friction coefficient
ν	Poisson's ratio
ξ	cumulative plastic shear strain
ξ_{95}	cumulative plastic shear strain required for 95% remoulding
ξ_{max}	fraction of critical damping in mode with highest frequency
ρ	soil density
σ_{eq}	equivalent Tresca stress [= $\sigma_1 - \sigma_3$]
σ'_{v0}	effective overburden stress
σ_{v0}	in-situ overburden total stress
$\sigma_1, \sigma_2, \sigma_3$	ordered principal stresses
$\sigma'_1, \sigma'_2, \sigma'_3$	ordered principal effective stresses
τ	shear stress
τ_{max}	shear stress limit for interaction in FE-model
ϕ	friction angle
ω	sampling frequency
ω_c	cut-off frequency
ω_{max}	maximum eigen-frequency

List of Abbreviations

Abbreviation	Explanation
BCT	Botney Cut soil unit
CEL	Coupled Eulerian-Lagrange
CIUc	Isotropic Consolidated Undrained triaxial test sheared in compression
CPT	Cone Penetration Test
DB	Dogger Bank
DBK_U_C	Upper Dogger Bank Clay unit
DBK_U_S	Upper Dogger Bank Sand unit
DOF	Degree Of Freedom
EVF	Eulerian Volume Fraction
FE	Finite Element
FEA	Finite Element Analysis
FEM	Finite Element Method
ISO	The International Organization for Standardization
OWT	Offshore Wind Turbine
PSA	Port Side Aft
PSF	Port Side Front
RB	Rigid Body
SBA	Starboard Aft
SBF	Starboard Front
SBF	Surface deposits soil unit
SLS	Serviceability Limit State
ULS	Ultimate Limit State
UU	Unconsolidated Undrained triaxial test

List of Figures

2.1	Geographical position of Dogger Bank	8
2.2	Size effects in London clay.	10
2.3	Principle sketch of a undrained triaxial compression test	13
2.4	The effect of strain rate on undrained shear strength.	14
2.5	Different stages of spudcan penetration during pre-loading	20

2.6	Comparison of a Eulerian and a Lagrangian mesh	23
2.7	Illustration of Eulerian volume fractions for a circular part	24
2.8	Frequency response function used in the Butterworth filter	28
2.9	Pile response to lateral loading	29
3.1	FE-model used for the triaxial test discretised with Mesh2	33
3.2	Stress - strain in FE-triaxial test showing the effect of mesh density and compression velocity	35
3.3	Contour plots of σ_{eq} and ξ for different meshes	36
3.4	Stress - strain in FE-triaxial test illustrating softening and rate effects	38
3.5	Comparison of strain rate effects measured in real and in FE-simulations of a triaxial compression test.	39
3.6	Various contour plots from Triaxial FE model	42
4.1	Measured q_t and design profile for DBB-JU1	48
4.2	Spudcan model used in FE-analyses	54
4.3	FE-model with spudcan and soil domain discretised with Mesh2.	57
4.4	Load-penetration response from convergence study (1)	58
4.5	Load-penetration response from convergence study (2)	61
4.6	Measured spudcan load-penetration response and penetration rate at DBB-JU1, and response from FEA	65
4.7	Spudcan load-penetration response from FEA showing the effect of penetration rate and plots of f_{rate}	67
4.8	Load-penetration response showing the effect of S_t , ξ_{95} and N_{kt}	68
4.9	Deformed spudcan FE-model with EVF-sand	70
4.10	Deformed spudcan FE-model with contours of Tresca stresses and ξ	71
4.11	Deformed spudcan FE-model with contours of the rate and softening effect	72
4.12	Soil velocity vectors during spudcan penetration	73
4.13	Measured spudcan load-penetration response and penetration rate at DBC-JU1, and response from FEA	74
5.1	Comparison of failure mechanisms for spudcan penetration and laterally loaded monopiles	86
5.2	FE-model used for monopile pushover analysis and FE-mesh	87
5.3	Measured q_t and design profile for DBB-JU1	90

5.4	Moment versus rotation from monopile analyses with different soil domain radii	92
5.5	Monopile response to lateral loading for different pile top lateral velocities	93
5.6	Contour plot of Tresca stress for the monopile FE-analysis	94
5.7	Contour plot of cumulative plastic shear strain, ξ , for the monopile FE-analysis	95
5.8	Contour plot of f_{soft} for the monopile FE-analysis	96
5.9	Contour plot of f_{rate} for the monopile FE-analysis	96
5.10	Soil velocity vectors from FE-analysis of a laterally loaded monopile	97
C.1	Comparing filtered and unfiltered load-penetration response.	118
C.2	Initial stresses in monopile pushover FE-analysis	119

List of Tables

3.1	Meshes considered for the soil domain in the triaxial model	34
4.1	Coordinates and water depth for spudcan penetration tests.	45
4.2	Geotechnical parameters for location DBB-JU1 and soil layering	51
4.3	Shear strength profile for location DBC-JU1	52
4.4	Geotechnical parameters for location DBC-JU1 and soil layering	53
4.5	Meshes considered for the soil domain in the convergence study.	56
5.1	Geotechnical parameters and soil layering used for the monopile FEAs	91
B.1	Design q_t -profile for location DBB-JU1	115
B.2	Shear strength profile used in the convergence study	115
B.3	The s_u -profile adopted for some FE-analyses and the correct s_u -profile at DBB-JU1.	116

Chapter 1

Introduction

1.1 Background

Monopiles are large diameter piles, typically made of circular steel tubes and have relatively small embedment depth to diameter ratio compared to typical longer more flexible piles. Therefore, design methods for longer flexible piles may not be suited for monopiles. For offshore wind turbines, monopiles are the most used foundation type, and with the growth of the offshore wind industry in the last years, many monopiles have been installed and will be installed in the future. When designing monopiles, the lateral capacity is important to ensure sufficient resistance against wind and wave actions, and monopile lateral capacity has become an important area of research.

The PISA joint industry project has investigated the lateral capacity of monopiles to develop design methods suited for such piles. In the PISA project lateral loading tests were carried out in soil similar to soil typically found in the North Sea. During one of the tests in clay the loading rate was unintentionally and dramatically increased which led to a significant increase in resistance. This indicates that monopiles in clay may have significant reserves of strength for high loading rates. These reserves can be utilised in design when dimensioning for loads with a short duration, such as wave loads.

This thesis will consider geotechnical design for the Dogger Bank Wind Farm located off the coast of England in the North Sea. The Dogger Bank area has a complicated geological history which has resulted in complex soil conditions with among other fissured clay. The fissures give rise to scale effects where the soil strength becomes dependent on size of the geotechnical prob-

lem. As a results it has proven difficult to determine reliable soil strength properties at Dogger Bank. Therefore, penetration tests with large spudcan foundations have been carried out at the area to better understand the operational strength of clays relative to large foundations such as monopiles. These spudcan penetration tests also included tests with different loading rates such that the effect of loading rate could be studied. By calibrating soil models which can account for rate effects against the measured rate effects in the spudcan penetration tests, such soil models can be used to study rate effects on the lateral capacity of monopiles in finite element analyses (FEAs).

1.2 Short Literature Review

Scale effects, where the soil strength relative to e.g a foundation becomes dependent on the foundation size, have previously been described by [Marsland \(1972\)](#). This paper describes a negative scale effect where small scale laboratory tests give significantly higher shear strength than large scale plate tests in stiff fissured London clay. Dogger Bank clay has been found to contain distinct fabric features with fissures and other weaknesses ([NGI, 2020a](#)), and [DNV GL \(2020\)](#) found a positive scale effect for Dogger Bank clay where soil strength determined from large scale spudcan tests was higher than strength determined by laboratory tests. The complex soil conditions at Dogger Bank are due to a complicated geological history with periods of repeated glaciation and desiccation giving different depositional environments resulting in large soil variability, both laterally and vertically. The geological history at Dogger Bank is described in [Cotterill et al. \(2017a\)](#) and [Cotterill et al. \(2017b\)](#).

Spudcans serve as foundations for jack-up rigs, and before a jack-up can be installed, the spudcan bearing capacity needs to be evaluated. The industry standard ISO 19905 ([ISO, 2016](#)) gives requirements and guidance for jack-up installation. The standard calculates spudcan bearing capacity with formulations based on shallow foundation theory, which is not accounting for the true failure mechanism evolving under a penetrating spudcan. Newer design methods for spudcan bearing capacity in clay are proposed by [Hossain and Randolph \(2009b\)](#). Spudcan bearing capacity can also be assessed with FE-analyses, but as spudcan penetration involves large soil deformations, an FE-method capable of describing large deformations is needed. The coupled Eulerian-Lagrange (CEL) approach can be used in FEA with large deformations and has been verified to give accurate results for geotechnical problems involving large deformations, such as spudcan penetration ([Qiu et al., 2011](#); [Tho et al., 2012](#)).

Strain rate effects for clays describe how the shear strength of clays are dependent on the rate of applied shear strain. Strain rate effects have previously been described by [Dayal and Allen \(1975\)](#) and [Casacrande and Wilson \(1951\)](#), and clays typically show an increase in strength of around 5-20 % per \log_{10} -cycle increase in loading rate ([Hossain and Randolph, 2009a](#)). The lateral capacity of monopiles is also affected by loading rate. In the PISA project it was found that the strength increased with 8 and 33 % per log-cycle of increase in loading rate respectively in two different pile loading tests ([Byrne et al., 2020](#)). As the difference in the observed rate effect in these tests is large, the results can not be used to precisely quantify the effect of loading rate on monopile lateral capacity. A more thorough review of relevant literature and theory is given in Chapter 2.

1.3 Problem Formulation

The effect of loading rate for monopile lateral capacity in general and for practical applications is still uncertain with the available information of today. Specially, rate effects for monopiles in complex fissured clay found in the North Sea and at the Dogger Bank Wind Farm is unclear. Moreover, strength properties and other properties of the Dogger Bank soil is a topic of research and are difficult to precisely define.

This master thesis will discuss spudcan penetration in the challenging soil conditions at the Dogger Bank Offshore Wind Farm, and is continuing the work from the preceding project thesis. The thesis will utilise new measurements from spudcan penetration tests at Dogger Bank to quantify strain rate effects and to evaluate the operational shear strength applicable for large foundations. This information will be used to investigate if strain rate effects can increase the lateral capacity of wind turbine supporting monopiles in the ultimate limit state. The thesis will employ a finite element method using the coupled Eulerian-Lagrangian approach together with a soil model capable of describing strain softening and strain rate effects.

Objectives

The main objective of this thesis is:

- To quantify loading rate effects on the lateral capacity of wind turbine supporting monopiles, and investigate if rate effects can increase the lateral capacity in the ultimate limit state.

Secondary objectives are:

- Develop a reliable finite element (FE) model for spudcan penetration using Abaqus\Explicit with the coupled Eulerian-Lagrangian (CEL) approach and a soil model which can describe strain rate and softening effects.
- Verify the implementation of the soil model in the FE-analyses by modelling a triaxial compression test and to study the behaviour of strain softening and rate effects in the soil model.
- Calibrate softening and rate effect parameters for the soil model against spudcan penetration tests, and apply the parameters to a monopile pushover analysis.
- Study the failure mechanism of a penetrating spudcan.

1.4 Approach

The main tool for studying rate effects for monopile capacity in this thesis is the FE-software Abaqus, which will be used with the coupled Eulerian-Lagrangian method which is suited to describe large deformations. In the finite element analyses the so-called UWA soil model will be employed which can describe strain softening and rate effects.

First, the use of Abaqus with the CEL approach and the UWA-model is studied with an FE-model of a triaxial test. This model is used to learn about appropriate modelling techniques and to study the behaviour of softening and rate effects in the UWA-model. Thereafter FEA is used to back calculate measurements from spudcan penetration tests at the Dogger Bank wind farm. An FE-model is established for this purpose and verified through a convergence study. The objective of the back-calculations is to calibrate parameters for the softening and rate effect in the UWA-model suitable for the complex Dogger Bank clay. To obtain geotechnical parameters for the spudcan back-calculations CPT and laboratory data is used. The rate effect parameters obtained from the spudcan analyses are also verified in the triaxial FE-model.

In the final part, material parameters and modelling experience obtained through the spudcan back-calculations are used in monopile pushover analyses. The analyses are carried out using Abaqus and the UWA-model with a similar modelling procedure as in the spudcan analyses. In the analyses the monopile is pushed over at different lateral velocities, and the soil resistance is measured. Hence, the effect of different pushover velocities can be quantified. Furthermore,

the monopile pushover analyses are designed to model a representative monopile at the Dogger Bank Wind Farm in the ultimate limit state to study rate effects for a realistic design case. Some simplifications are adopted for the monopile analyses as the objective is not to obtain an accurate lateral resistance, but to study relative rate effects.

1.5 Limitations

This thesis is subjected to the following limitations:

- The thesis does not study in detail how drained material as sand should be accounted for in the analyses, as the main objective is to study clay behaviour. The influence of drained material on spudcan and monopile capacity is not investigated.
- The possible presence of spurious mesh dependency in the analyses due to the inclusion of strain softening in the material model is only briefly discussed.
- The UWA soil model is implemented in Abaqus with a user defined subroutine which is not written by the author, and the subroutine has not been verified for this thesis.
- The monopile analyses do not account for cyclic degradation, and the subject is only briefly discussed.
- Dynamic inertia effects are not included in the monopile analyses. Neither are the effect of suction or water flow behind the monopile.

1.6 Report Structure

The thesis is structured as follows:

Chapter 2 presents relevant literature and theory which is used in the thesis and to support the thesis.

Chapter 3 documents the triaxial analyses used to verify the UWA material model and to study the rate and softening effects available in the model. The results from the triaxial model is discussed.

Chapter 4 describes the Dogger Bank jacking trials. The FE-model used for the spudcan back-calculations is described and the convergence study for the model is presented. Next, the back-calculations are described and discussed.

Chapter 5 is describing the monopile analyses which are used to investigate rate effects for monopile capacity. The results are presented and discussed.

Chapter 6 gives a summary of the what is done during the work for this thesis and summarises the main results. Recommendations for further work is given.

1.7 Citation from Project Thesis

This master thesis is the continuation of a project thesis, and the current thesis contains some citation from the project thesis. Sections containing citation are noted in the text, and a list of the affected sections is given below.

- 2.1 Dogger Bank
- 2.5 Spudcan Penetration in Clay
- 2.6.1 Large Deformation Finite Element Modelling
- 4.1 Dogger Bank Jacking Trials 2020

Chapter 2

Literature Review and Theory

2.1 Dogger Bank

Note that the following text in this subsection (sec. 2.1) is citation from the project thesis (Wahl, 2020) preceding this master thesis. Some changes to the text have been made.

2.1.1 Site Characterisation

The Dogger Bank (DB) area is a topographical high in the middle of the North Sea, and is located between 125 km and 290 km southwest off the coast of Yorkshire, England. The location is shown in Figure 2.1(a). The water depths at the location vary between 18-63 m. This thesis will discuss the area covered by the Dogger Bank Wind Farm, which consists of three development phases, Dogger Bank A, Dogger Bank B and Dogger Bank C, covering approximately 8660 km² and shown in Figure 2.1(b) (Cotterill et al., 2017b).

Dogger Bank has a complex geological history. The formation mainly consists of core sediments from geological epoch Pleistocene, surrounded and covered by a thin layer of Holocene sediment. The Pleistocene is the time period spanning from ~ 2 580 000 to ~ 11 700 years before our time. This period contains the last epoch of repeated glaciation and ends with the last ice age. The Holocene epoch is the period succeeding the Pleistocene and is the current time epoch. During Pleistocene there were several periods of glacial progression with subsequent melting and glacial retraction in the Dogger Bank area. These processes created lakes of dammed-up meltwater with river systems. Furthermore, the sea level was also rising and sinking with the growth and shrinkage of the ice, such that the Dogger Bank rose above the sea level for periods

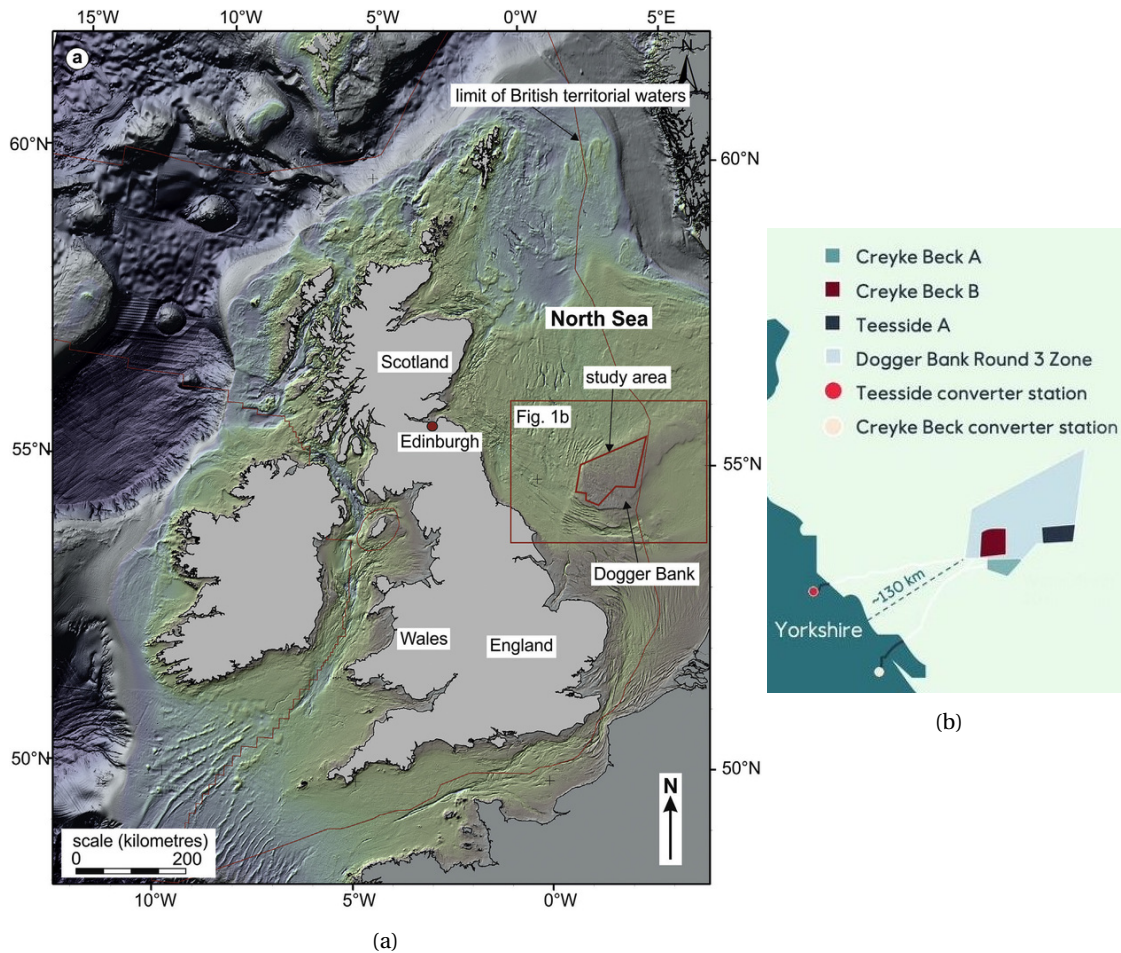


Figure 2.1: (a) shows the position of Dogger Bank. Taken from [Cotterill et al. \(2017b\)](#). (b) shows the three areas for the Dogger Bank Wind Farm. Note that the previous names of DB-A, DB-B and DB-C are used in the figure. Taken from www.equinor.com.

of time. The DB area was not fully submerged before 7 800 years ago ([Stylegar and Askheim, 2018](#)). A complex interplay between these processes including ice deformation, desiccation, erosion and sedimentation from the sea and from glacial rivers have resulted in the area known as Dogger Bank. The reader is referred to [Cotterill et al. \(2017a\)](#) and [Cotterill et al. \(2017b\)](#) for a more in-depth description of the geology at Dogger Bank.

The result of the geological processes is that Dogger Bank is made up of units of clay deformed by ice sheet movements with basins and ridges. Also, this clay has been exposed to desiccation and erosion. During DB's history other marine and glaciofluvial deposits and deposits from glacial lakes, including clay, sand and silt, have been added on top of the clay and possibly deformed further by ice movements. The outcome of this is that DB has a very variable stratigraphy, both laterally and vertically. There are signs of buried river and moraine systems. Another result from the geological history, in particular desiccation and freeze-thaw, is that the clay is fis-

sured. From experience it has been difficult to get undisturbed soil samples for laboratory testing, and for instance the fissures affect the undrained shear strength measured in triaxial tests. The measured strength is lower than what is experienced in practice (NGI, 2020a). In general, the complex geological history at Dogger Bank makes geotechnical design more complicated.

2.1.2 Offshore Wind Project

The Dogger Bank offshore wind project consists of three offshore development zones, Dogger Bank A (DB-A), DB-B and DB-C, located in British territorial waters. Together the development zones span approximately 1674 km². The zones are shown in Figure 2.1(b). The project has been in development since 2008, when the Crown Estate opened its third licence round for offshore wind, which included Dogger Bank. The project is currently owned by Equinor, SSE Renewables and Eni.

The project, when completed, will be the worlds largest offshore wind farm, and will have a combined installed generation capacity of 3,6 GW. The first zone, DB-A, is set to start production in 2023 (Dogger Bank Wind Farm, 2021).

2.2 Scale effects

Scale effects in geotechnical engineering is accounting for the fact that the engineering properties of soils, e.g. strength and stiffness, may be dependent on the size of the geotechnical problem. Scale effects is exhibited by clays with fissures and planes of weakness, and the spacing and orientation of the fissures will affect the strength experienced in the field and may differ from strength measured on small samples in triaxial cells. The reason for such scale effects is that a small sample and its failure mode is not representative for the soil structure and failure mode of a larger structure in the field.

This phenomenon has previously been described for London clay, which largely comprise of stiff fissured clay, by Marsland (1972) where strength measurements from in situ plate tests were compared to laboratory measurements on differently sized specimen. The plate tests were performed by loading $\varnothing 292$ mm plates at the bottom of boreholes of different depths and measuring the response. Thereafter, back-calculating the undrained shear strength (s_u). For laboratory testing 38 mm samples were cut from 300 mm blocks, and 98 mm samples were extracted by pushing in steel tubes. The samples were then tested in undrained isotropically consolidated

triaxial compression.

The strength measurements are plotted and compared in Figure 2.2. In the figure s_u measured from 38 mm samples is on average up to 60 % higher than s_u from in situ plate test. The strength measured from test on 98 mm samples are however, in reasonable agreement with the plate tests. The far right curve shows average intact soil strength from small penetrometer tests. The intact strength, not accounting for fissures and weaknesses in the soil, is three to four times larger than s_u from plate tests, grossly overestimating the large scale strength of the soil. Note that the lines in the figure representing the strength measured from borehole samples are regression lines, and that the true measurements showed considerable variability, whereas the plate tests show a much clearer linear trend. Furthermore, the variability in the 38 mm samples is much larger than the variability of the 98 mm samples, and the variability of the in situ plate test was less than half of the variability of the results from the 98 mm samples. This clearly demonstrates the negative size effects in London clay where small soil samples overestimate the large scale strength of the clay relevant for foundation design. Moreover, the overestimation is larger the smaller the sample is.

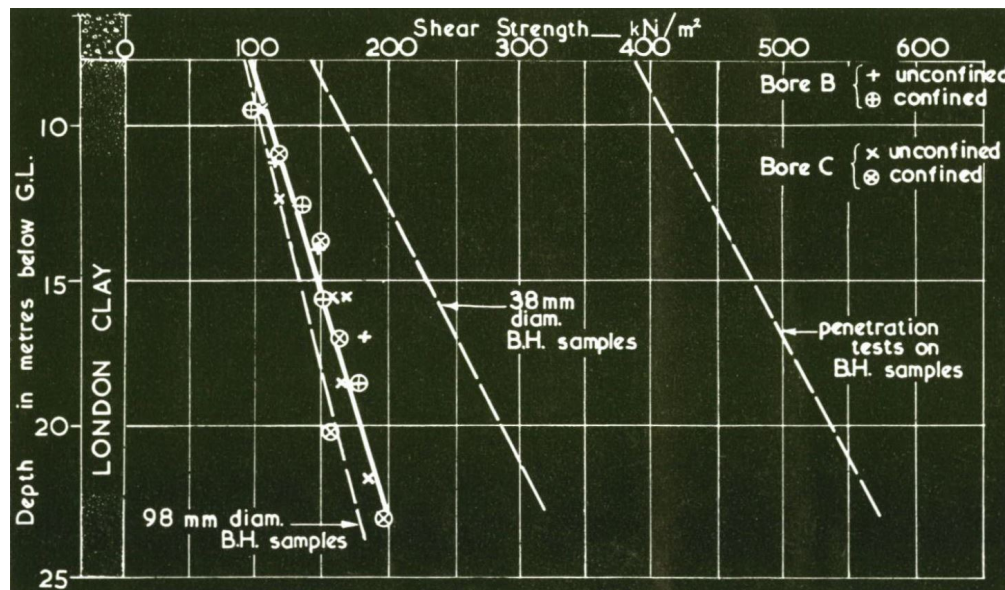


Figure 2.2: Comparing shear strength measured from plate tests, triaxial tests and small penetrometer tests illustrating size effects for London clay. Taken from Marsland (1972).

Negative scale effects has also been reported for pile design in fissured clay (Meyerhof, 1983). Here the author propose a reduction factor to be applied to s_u from triaxial tests to account for scale effects. The factor is a function of pile diameter and is decreasing for increasing pile diameter. Lunne et al. (1997) is pointing out that s_u interpreted from Cone Penetration Tests

(CPT) must be treated with caution in highly overconsolidated clays due to the possible effect of fissures. The book also gives correction for the s_u if information on the nature of the fissures are known.

The reason for these scale effects on measured shear strength is that samples with a small soil volume may not contain a good representation of the soil structure. Thus the effect of fissures and planes of weakness on the soil strength will not be accounted for in tests on small samples. The scale effect is dependent on the relation between the sheared soil volume and the fissure spacing. Because of this s_u must be defined for soil volume representative of the geotechnical problem such that all fabric features of the soil type are present in the volume which is being sheared. This is herein denoted *operational shear strength*. The reason for the reduced variability in strength parameters determined from larger in situ tests may be due to that such tests involve a larger soil volume and are therefore less affected by local variations of soil composition and parameters. Scale effects may reduce or increase the large scale strength depending on the fissure spacing or density. Large fissure spacing may reduce the large scale strength, since the weaknesses of the fissures are not captured in small scale laboratory tests but are captured in large scale tests. Whereas small fissure spacing will influence small scale laboratory tests and be less prominent in large scale tests.

A widely used method for obtaining s_u profiles in clays is to use the relation $s_u = q_n / N_{kt}$, where q_n is net cone resistance and N_{kt} is an empirical cone factor. q_n is obtained from CPTs. The N_{kt} -factor is calibrated with s_u measurements from triaxial tests. However this method is not reliable for fissured clay due to scale effects which may give wrong s_u in triaxial testing. Therefore, a cone factor for operational shear strength, N_{kt}^* should be established, calibrated against in situ tests involving a representative soil volume. Such tests can be plate loading tests or spudcan penetration tests.

The soil at Dogger Bank (DB) is largely made up of deformed clay units as shown in section 2.1, and NGI (2020a) has documented that the soil samples contain distinct fabric features with fissures, foliations, slickensides (polished surfaces), and blocky structure. These soil features give rise to size effect issues at DB, and back-calculations from spudcan penetration tests at DB documented in DNV GL (2020) found that s_u from these tests were generally higher than those from laboratory strength determinations. Thus, there is a positive scale effect where larger soil volumes give higher strength at Dogger Bank, and NGI (2020a) states the need to establish a N_{kt}^* -factor for geotechnical design at DB. DNV GL (2020) also showed that s_u determined from spudcan penetration tests had much less variability than s_u determined from triaxial testing,

thus easing geotechnical design.

2.3 Triaxial Test

Triaxial compression tests are a well known and common laboratory test for determining material parameters of soils. There are several standard test procedures where the sample can be consolidated isotropically or anisotropically and sheared in compression or extension while being drained or undrained in addition to other special triaxial tests. Herein an isotropically consolidated undrained triaxial compression test with constant confining pressure (CIUc-test) is considered, as sketched in Figure 2.3. The response for an elastic perfect-plastic soil obeying the Tresca yield criterion is described. In such a test Hooke's law gives the following relation for the elastic response (Sandven et al., 2017)

$$\Delta\varepsilon_1 = \frac{1}{E} (\Delta\sigma'_1 - \nu\Delta\sigma'_2 - \nu\Delta\sigma'_3) = \frac{\Delta\sigma'_1}{E} \quad (2.1)$$

when applying constant confining pressure, i.e. $\Delta\sigma'_2 = \Delta\sigma'_3 = 0$. E is the modulus of elasticity, $\Delta\sigma'_1$, $\Delta\sigma'_2$ and $\Delta\sigma'_3$ are changes in the principal effective stresses and $\Delta\varepsilon_1$ is change in the major principal strain. ν is the Poisson's ratio which is equal to 0,5 for undrained conditions.

A useful stress measure in triaxial tests is the deviatoric stress denoted q and is equal to $\sigma_1 - \sigma_3$, and also equal two times the maximum shear stress in the soil. Thus for an undrained clay obeying the Tresca yield criterion, q can have a maximum value of two times the undrained shear strength, $2s_u$. Furthermore, for $\Delta\sigma_3 = 0$ eq. (2.1) can be rewritten as

$$E = \frac{\Delta\sigma'_1}{\Delta\varepsilon_1} = \frac{\Delta q}{\Delta\varepsilon_1} \quad (2.2)$$

and thus the inclination in an $\varepsilon_1 - q$ plot is equal to E in the elastic range. The strain at first yield should be equal to $2s_u/E$.

During a CIUc triaxial test a plate compresses the soil. First elastic until failure thereafter plastic strains develop. Therefore σ_1 is equal to the axial stress, as indicated in Figure 2.3. σ_1 can be calculated as F/A where F is the force needed to compress the sample, and A is the sample area. The same relation holds for the strains, such that the axial strain ε_a is equal to ε_1 . Thus ε_1 can be calculated as the change in specimen height divided by the initial height of the specimen, i.e. $\Delta L/L_0$. When the sample is compressed in undrained conditions the volume strain is zero, and therefore the axial strain will change the area of the specimen. It is customary to account

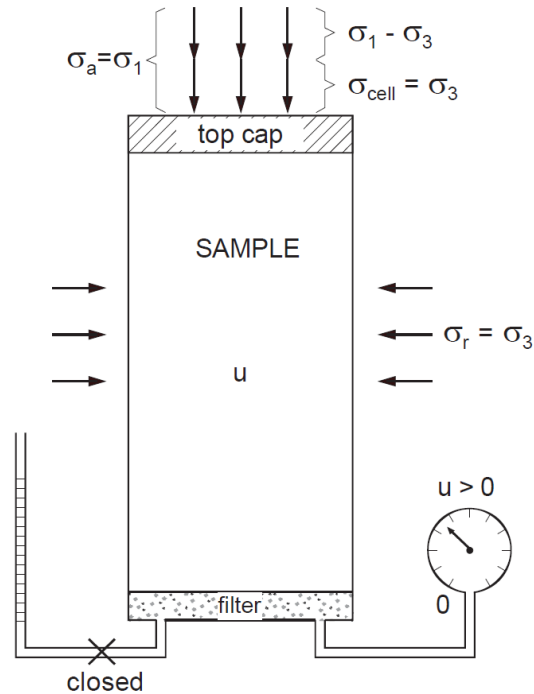


Figure 2.3: Principle sketch of a drained triaxial compression test. Adapted from [Sandven et al. \(2017\)](#).

for the change in area when calculating q , however, such corrections are not considered here.

A soil element from such a CIUC triaxial test has $\Delta\sigma_1$ parallel to the axial direction and since $\Delta\sigma_2 = \Delta\sigma_3 = 0$ the planes of maximum shear stress will be inclined 45° to the axial direction, and failure can be expected to take place in the same 45° planes. A more in-depth description of the triaxial test can be found in [Sandven et al. \(2017\)](#).

2.4 Strain Rate and Softening Effects

During spudcan penetration the soil goes through large deformations and is gradually remoulded as the soil flows around the spudcan. It is well known that the undrained shear strength of clays decreases when subjected to shear strains and remoulding. The ratio of peak or intact and remoulded shear strength ($s_u/s_{u,r}$) is termed as the sensitivity of the clay, S_t , and typically range from 2 to 5 for marine clays ([Kvalstad et al., 2001](#)). The decrease of shear strength with increasing shear strain is referred to as strain softening, and accounting for strain softening in FEA is important when modelling spudcan penetration due to the large shear strains developing as noted by [Hossain and Randolph \(2009a\)](#).

Another property of clays are the rate effect, and it describes how the shear strength of clays

are dependent on the rate of applied shear strain. In general, the measured strength of clay that is being loaded rapidly is larger than the measured strength from clay which is loaded more slowly. This is due to the differences in strain rate. Clays typically show an increase in strength of around 5-20 % per \log_{10} -cycle increase in loading rate (Dayal and Allen, 1975; Hossain and Randolph, 2009a). An early investigation of rate effects can be found in Casacrande and Wilson (1951), and an overview of later publications discussing rate effects can be found in Hossain and Randolph (2009a). This paper describes how strain rate and softening effects influences FE analyses of spudcan penetration.

The effect of strain rate on measured strength in triaxial compression and extension tests from several different Norwegian calys is plotted by Lunne and Andersen (2007), and a fitting function to the data has been proposed by Huynh et al. (2019). The plotted measurements are shown in Figure 2.4 where shear strength is plotted against strain rate from the triaxial tests. The shear strength is normalised against the maximum shear strength in tests with a shear strain rate of 4.5 %/hr. For a description of the plotted data the reader is referred to Lunne and Andersen (2007). From the figure it is evident that larger shear strain rates give higher shear strength. The proposed fitting function for the ratio of mobilised strength due to strain rate effect $s_{u,rate}$ to the reference shear strength have the following expression:

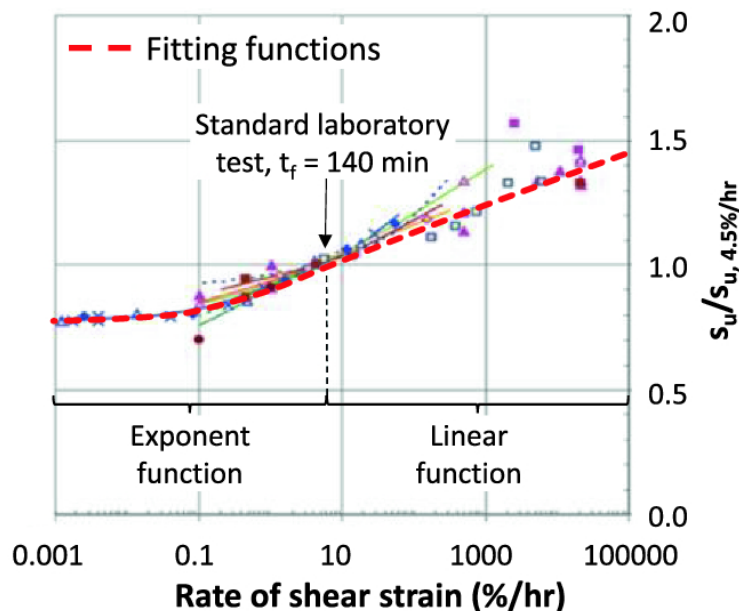


Figure 2.4: The effect of strain rate on undrained shear strength measured in triaxial testing. Both measured data and proposed fitting functions are displayed. Taken from Huynh et al. (2019).

$$\frac{s_{u,\text{rate}}}{s_{u,\text{ref}}} = \begin{cases} 0.22 \cdot \exp[-0.75|\log(\dot{\gamma}/\dot{\gamma}_{\text{ref}})|^{1.3}] + 0.78 & \text{when } \log(\dot{\gamma}/\dot{\gamma}_{\text{ref}}) < 0 \\ \min\{1, 45; 0, 11 \log(\dot{\gamma}/\dot{\gamma}_{\text{ref}}) + 1, 0\} & \text{when } \log(\dot{\gamma}/\dot{\gamma}_{\text{ref}}) \geq 0 \end{cases} \quad (2.3)$$

where

- $s_{u,\text{ref}}$ – reference shear strength at the reference shear strain rate
- $\dot{\gamma}$ – shear strain rate
- $\dot{\gamma}_{\text{ref}}$ – reference shear strain rate

Note that due to a misprint the absolute value symbol in the exponent of eq. (2.3) is not included in the paper. Equation (2.3) has been developed at NGI, and is therefore in the following referred to as the NGI rate equation.

2.4.1 Material model incorporating softening and rate effects

For this thesis a material law based on the widely used Mohr–Coulomb failure criterion with zero friction and dilatation angle, which reduces to the Tresca failure criterion, will be used. In the Tresca criterion the material behaves perfect elastic until the shear stresses reach the value of the undrained shear strength, s_u . If additional stresses are applied the material will yield and develop plastic strains. In the simplest form the criterion can be written $2\tau = \sigma_1 - \sigma_3 \leq 2s_u$, where σ_1 and σ_3 are the largest and smallest principal stress, respectively, and τ is shear stress.

To account for strain softening and rate effects the undrained shear strength is modified according to the following expression:

$$s_u = \underbrace{\frac{1}{1+\eta} \left[1 + \eta \left(\frac{\max(\dot{\gamma}, \dot{\gamma}_{\text{ref}})}{\dot{\gamma}_{\text{ref}}} \right)^\beta \right]}_{\text{Rate effects} = f_{\text{rate}}} \underbrace{\left[\delta_{\text{rem}} + (1 - \delta_{\text{rem}}) e^{-3\xi/\xi_{95}} \right]}_{\text{Softening effects} = f_{\text{soft}}} s_{u,\text{ref}} \quad (2.4)$$

where

- η – viscous property
- β – shear-thinning index
- δ_{rem} – ratio of intact and remoulded shear strength (inverse sensitivity)
- ξ – cumulative plastic shear strain
- ξ_{95} – cumulative plastic shear strain required for 95% remoulding
- $s_{u,\text{ref}}$ – reference shear strength at the reference shear strain rate before softening

This material model (eq. 2.4) is primarily developed at the University of Western Australia (UWA), and herein the model is referred to as the UWA-model. This model (eq. 2.4) was first

employed by [Kim et al. \(2015\)](#), but a similar model with a logarithmic strain rate formulation was adopted by [Zhou and Randolph \(2007\)](#). The current formulation, i.e. eq. (2.4), is based on a power-law formulation for the rate effect first proposed for fluids by [Herschel and Bulkeley \(1926\)](#) and later adopted for geotechnical use, see e.g [Zhu and Randolph \(2011\)](#).

The UWA-model modifies the undrained shear strength according to the rate of maximum shear strain, $\dot{\gamma}$, and accumulated absolute plastic shear strain, ξ . The rate effect is controlled by the viscous property, η , and shear-thinning index, β . $\dot{\gamma}$ can be defined as

$$\dot{\gamma} = \frac{\Delta\varepsilon_1 - \Delta\varepsilon_3}{\Delta t}$$

where $\Delta\varepsilon_1$ and $\Delta\varepsilon_3$ are the incremental major and minor principal strains, respectively, accumulated over the time increment Δt ([Kim et al., 2015](#)). The strain softening is controlled by δ_{rem} and ξ_{95} . δ_{rem} is the inverse sensitivity, $1/S_t$. The ductility of the material-model is controlled by the parameter ξ_{95} which is how much cumulative plastic shear strain that is required for 95% remoulding, i.e. when ξ is equal to ξ_{95} the shear strength is 5 % larger than the remoulded shear strength. Typical values for ξ_{95} has been estimated to around 10–25, i.e. 1000–2500 % shear strain ([Hossain and Randolph, 2009a](#)), although the value will be heavily dependent on the soil type considered.

To put it another way, the UWA-model can be thought of to consist of two factors, one accounting for strain softening f_{soft} and one accounting for rate effects f_{rate} , as indicated by the curly brackets in eq. (2.4). These factors then scale the reference shear strength according to the shear strain rate and accumulated plastic shear strain. f_{soft} and f_{rate} equal to one means there is no softening or rate effects, while $f_{\text{soft}} < 1$ indicates softening and $f_{\text{rate}} > 1$ indicates rate effects.

Herein the UWA-model is implemented in FE-analyses by using Abaqus\Explicit with a user-defined subroutine, VUMAT. In the subroutine the equivalent plastic shear strain, ξ , is calculated as

$$\begin{aligned} \xi &= \sum_t \Delta\varepsilon_{eq} = \sum_t \sqrt{\frac{2}{3} \Delta\varepsilon_{ij}^p \Delta\varepsilon_{ij}^p} \\ &= \sum_t \sqrt{\frac{2}{3} \left\{ (\Delta\varepsilon_{11}^p)^2 + (\Delta\varepsilon_{22}^p)^2 + (\Delta\varepsilon_{33}^p)^2 + 2 \left[(\Delta\varepsilon_{12}^p)^2 + (\Delta\varepsilon_{13}^p)^2 + (\Delta\varepsilon_{23}^p)^2 \right] \right\}} \end{aligned} \quad (2.5)$$

and the shear strain rate is calculated as

$$\dot{\gamma} = \frac{\Delta \varepsilon_{eq}}{\Delta t} \quad (2.6)$$

Where $\Delta \varepsilon_{ij}^p$ is the incremental plastic strain tensor and $\Delta \varepsilon_{eq}$ is incremental equivalent plastic strain in the von Mises yield criterion. As ξ is defined with eq. (2.5) using the equivalent plastic strain from the von Mises criterion, which is not plastic shear strain but regular strain, it may be incorrect to term ξ equivalent plastic *shear* strain. However, to be consistent ξ is still referred to as equivalent plastic *shear* strain. Note that since $\dot{\gamma}$ is calculated with eq. (2.6), $\dot{\gamma}$ will then be the plastic shear strain rate, not shear strain rate. Thus the rate effect will only be dependent on plastic strains, and can be considered as a viscoplastic effect.

The NGI rate equation (2.3) has a cap for the rate effect, f_{rate} , of 1,45, hereafter referred to as f_{rate}^{max} . This cap is not included in the UWA-model eq. (2.4), but a cap for f_{rate} has been included in the implementation of the UWA-model in Abaqus for this thesis, where f_{rate}^{max} can be set to any value. This makes it possible to set a limit for the maximum rate effect.

2.4.2 Modelling of Rate Effects in FE-Analyses

Modelling rate effects in FEA which uses explicit dynamic solution algorithms requires special considerations. Herein spudcan penetration, overturning of a monopile and a triaxial compression test will be modelled. A similarity between the physical nature of these problems is that they extend over large time in the real world, e.g the installation of a spudcan can take from several hours to over a day to complete. In explicit dynamic analyses the analysis is executed over a given time period, and the computational time is proportional to the length of the time period. Hence, it is impractical to model the true time period of which the relevant problem spans over since this would require too much computational time. Therefore it is customary to use an artificially high loading rate for such FEA, but this gives rise to two problems. 1) the increased loading rate may give unwanted dynamic effects, and therefore the prescribed loading rate must be verified to be sufficiently low to avoid such effects. 2) an artificially increased loading rate gives higher strain rates which in turn give higher strain rate effects than what would be the case in reality.

Since the rate effect is dependent on the ratio of strain rate to reference strain rate, $\dot{\gamma}/\dot{\gamma}_{ref}$, as shown in eq. (2.4), $\dot{\gamma}_{ref}$ can be changed to account for the loading rate. This is because the loading rate directly influences $\dot{\gamma}$. Thus, to overcome the above problems the following approach is

employed in this thesis. To modify $\dot{\gamma}_{\text{ref}}$ in a consistent manner, a normalised non-dimensional loading rate or velocity v_n is introduced as

$$v_n = \frac{v}{\dot{\gamma}_{\text{ref}}D} \quad (2.7)$$

where v is a loading rate, e.g. the compression rate in a triaxial test or the penetration rate of a spudcan in a field test, and D is a characteristic length of the physical problem, e.g. the diameter of a spudcan or a triaxial soil sample. Then, $\dot{\gamma}_{\text{ref}}$ can be modified such that v_n has the same value in the real world and in the FEA. First, v_n is calculated using the real physical loading rate and the reference strain rate, $\dot{\gamma}_{\text{ref}}$, taken from the relevant testing procedure used to obtain the reference shear strength, $s_{u,\text{ref}}$. For example, in typical triaxial tests $\dot{\gamma}_{\text{ref}}$ is equal to 3 %/hr (Lunne and Andersen, 2007). For the FEA, a loading rate which is sufficiently high to give an acceptable computational time while avoiding unrealistic dynamic effects is obtained, denoted v_A . Then in the FEA, v_A is used as the loading rate and kept constant, regardless of the true loading rate. Instead, $\dot{\gamma}_{\text{ref}}$ is modified to account for the real loading rate such that v_n is equal in the FE-analysis and in the reality.

As an example of how this method is applied, consider a spudcan field test where a spudcan with a diameter of 10 m is penetrated at 2 m/h and the soil has a reference shear strain rate of 1 %/hr. Thus $v/\dot{\gamma}_{\text{ref}}D$ is equal to 20. In the corresponding FE-analysis the spudcan penetration rate, v is speeded up by a factor of 100 such that v_A is equal to 200 m/h. Hence $\dot{\gamma}_{\text{ref}}$ must be increased to 100 %/hr thereby keeping $v/\dot{\gamma}_{\text{ref}}D$ equal to 20. If it is desirable to do FEA with higher penetration rates, v_A can be kept constant and instead $\dot{\gamma}_{\text{ref}}$ reduced.

This approach where v_n is used to model rate effects together with a rate dependent soil model has previously been adopted by Huynh et al. (2019) for studying T-bar penetration, by Hossain and Randolph (2009a) for studying spudcan penetration and by Chatterjee et al. (2012) for studying penetration of seabed pipelines.

2.5 Spudcan Penetration in Clay

Note that the following text in this subsection (sec. 2.5) contains citation from the project thesis (Wahl, 2020) preceding this master thesis. Parts of this text is taken from the project thesis, but some text is added or changed.

Spudcans are conically shaped footings which can function as foundations for offshore jack-up rigs. Jack-ups are typically supported by three or four truss work legs with spudcans at the bottom. The spudcans themselves may be made up of steel plates and internal stiffeners. In shape they may have a circular or rectangular cross section and a conical underside with a sharp protruding spigot. Typical spudcan diameters can be in the range from 10 m to 20 m.

When a jack-up rig is to be installed at a new location the legs of the jack-up is lowered down to the seabed. Next the jack-up is jacked out of the water simultaneously pushing the legs into the seabed. Furthermore, each leg is pre-loaded to ensure sufficient bearing capacity of the spudcan during operation. This pre-loading causes further spudcan penetration where the spudcans can penetrate from a few meters up to several tens of meters depending on the soil conditions present.

For safety and practical reasons it is important to calculate expected spudcan penetration depth and soil resistance prior to the jack-up installation. Moreover, if the strength of the soil is uncertain it is possible to back-calculate the soil strength from measured spudcan penetration resistance, which can then be used in other geotechnical design, provided a reliable relation between soil strength and spudcan penetration resistance is available.

A more in-depth description of jack-up installation and spudcan penetration can be found in [Randolph and Gourvenec \(2011\)](#), and requirements and guidance for installation of jack-ups can be found in the industry standard ISO 19905 ([ISO, 2016](#)). Furthermore, much knowledge about and previous research into spudcan penetration exists. Much of the previous research have dealt with how bearing capacity formulations for shallow foundations can be adapted for spudcan penetration, see eg. [Dean \(2008\)](#). Newer research has investigated bearing capacity formulations tailored for spudcan penetration ([Hossain and Randolph, 2009a; 2009b](#)), and a summary of previous work on this field can be found in [Hossain and Randolph \(2009b\)](#).

2.5.1 Spudcan Failure Mechanisms and Bearing Capacity

When a spudcan is penetrating a continuous bearing failure is evolving below the spudcan. In the first phase of the penetration the mechanism is similar to the mechanism described in classical shallow foundation theory with a combination of plastic rankine and prandtl zones. Also, a cavity is formed in the seabed when the spudcan is penetrating until the spudcan reaches the ultimate cavity depth and the soil starts to envelope the spudcan. Figure 2.5 is showing the different stages during spudcan penetration. After the ultimate cavity depth is reached the failure mechanism changes to a plastic flow around the spudcan. In the time between these two failure modes the failure mechanism is transitioning with some soil flow around the spudcan.

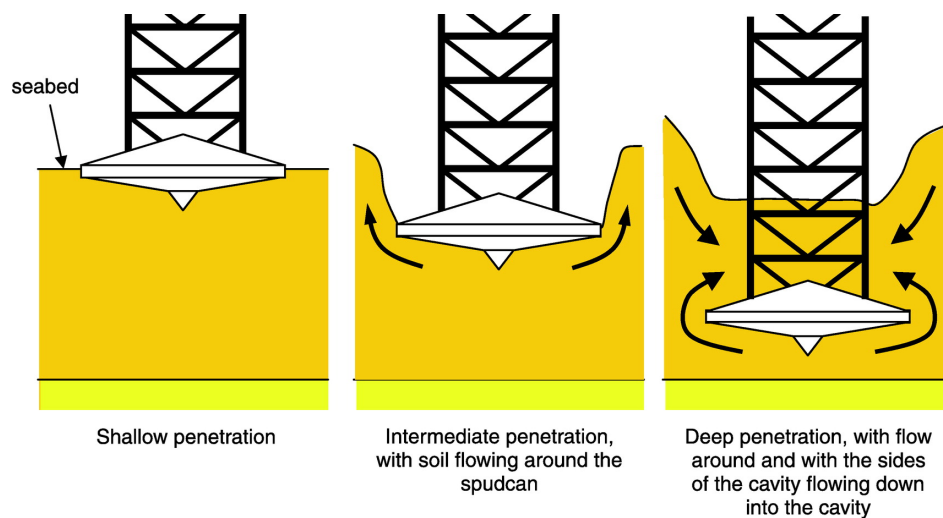


Figure 2.5: Different stages of spudcan penetration during pre-loading. Taken from [Dean \(2008\)](#).

This complicated interplay of failure mechanisms is quite different from conventional bearing capacity for shallow foundations and is not described well with formulas for shallow foundations. Nevertheless, the industry standard is to calculate spudcan penetration with formulas developed for shallow foundations ([ISO, 2016](#)). This is because bearing capacity formulas suited for continuous spudcan penetration have not yet been developed for industry use, and although formulas for shallow foundations are not designed for spudcan penetration, these formulas still give reasonably good predictions for spudcan load-penetration response.

[ISO \(2016\)](#) calculates the gross ultimate vertical bearing capacity for undrained clay Q_v in a given depth as

$$Q_v = (s_u N_c s_c d_c + \sigma'_{v0}) A \quad (2.8)$$

where

- N_c – bearing capacity factor
- s_c – shape factor
- d_c – depth factor
- σ'_{v0} – effective overburden vertical stress
- A – maximum bearing area in contact with soil

Available structural spudcan reaction V_L is then calculated as:

$$V_L = Q_V + B_S - W_{BF} \quad (2.9)$$

Where B_S is the buoyancy of the spudcan volume below the cross section with area A in the soil, and W_{BF} is the weight of the backflow on the top of the spudcan. To calculate the weight of the backflow the ultimate cavity depth needs to be found. This method for calculating spudcan penetration resistance does not account for the actual failure mechanism under a penetrating spudcan. For instance this method does not account for the tendency of softer soil to be trapped under the spudcan during penetration resulting in lower soil strength at a given depth than the expected in-situ strength (Hossain and Randolph, 2009b).

A different so-called mechanism-based approach has been proposed by Hossain and Randolph (2009b). This approach considers the true failure mechanism, and is based on finite element analyses (FEA) and centrifuge tests. From their work they were able to obtain expressions for bearing capacity factors, N_c for among other clay with increasing shear strength with depth which is adapted for the different failure mechanisms for spudcans. However these bearing capacity factors are not further discussed here. The paper also gives formulas for the maximum cavity depth, H_{cav} :

$$\frac{H_{cav}}{D_{eq}} = \left(\frac{s_{uH}}{\gamma' D_{eq}} \right)^{0.55} - \frac{1}{4} \left(\frac{s_{uH}}{\gamma' D_{eq}} \right) \quad (2.10)$$

where D_{eq} is the equivalent diameter of the spudcan, s_{uH} is the undrained shear strength at a depth H_{cav} below the seabed and γ' it the effective unit weight of the soil. Using eq. (2.10) H_{cav} can be found by iteration. Furthermore, in a later publication Hossain and Randolph (2009a) found that accounting for softening and rate effects will reduce H_{cav} with approximately 20% to 35% heavily dependent on the soil properties and the assumed rate and softening parameters.

Note that the above discussion is considering spudcan penetration in single layer undrained clay. For other soils and layer configurations spudcan failure mechanisms and bearing capacity is more complex than described herein. For example if there is strong soil overlaying a soft

soil, punch-through failures where the strong soil is pushed into the underlying soft soil subsequently reducing the bearing capacity and giving large penetration, can happen. Thus, more extensive considerations need to be used when determining the load-penetration response for a spudcan in a real case.

2.6 Finite Element Analysis

Finite elements analyses (FEA) are widely used in the work for this thesis. In the following a description of the used finite element method is described, especially attention is given to the Coupled Eulerian-Lagrangian approach used to account for large deformations. Furthermore the explicit dynamic solution method and filtration of noise is described. Different factors affecting the computational time is discussed.

2.6.1 Large Deformation Finite Element Modelling

Note that the following text in this subsection (sec. 2.6.1) contains citation from the project thesis (Wahl, 2020) preceding this master thesis. The main part of this text is taken from the project thesis, but some text is added or changed.

The conventional finite element method (FEM) used in structural and geotechnical engineering uses a Lagrangian mesh. In this approach the element nodes remain coincident with material points, and mesh boundary points remain on the material boundary during the analysis. It follows from this that if the material undergoes large deformations the mesh becomes severely distorted which leads to deterioration in solution accuracy due to problems like mesh locking and numerical instability. Thus, modelling problems involving large deformations such as spudcan penetration and pile installation with a Lagrangian mesh is difficult. An advantage of the Lagrangian mesh is that since the element and material boundary coincide, it simplifies the imposition of boundary conditions. The interface between parts and materials are also well defined in a Lagrangian mesh.

A different approach is to use an Eulerian mesh. In this approach the nodes of an element are stationary in space, whereas the material points move in space through the mesh. With this type of mesh, it will not become distorted when the material deforms and the problem of material deformations leading to large mesh distortions are alleviated. On the other hand the material boundaries will not coincide with the element boundaries, and this complicates the

imposition of boundary conditions. Furthermore, the interface between parts and materials are less precisely defined. The difference between the two mesh techniques are illustrated in Figure 2.6. The figure shows that the Lagrangian elements get distorted after the material has deformed while the Eulerian elements keep their original shape.

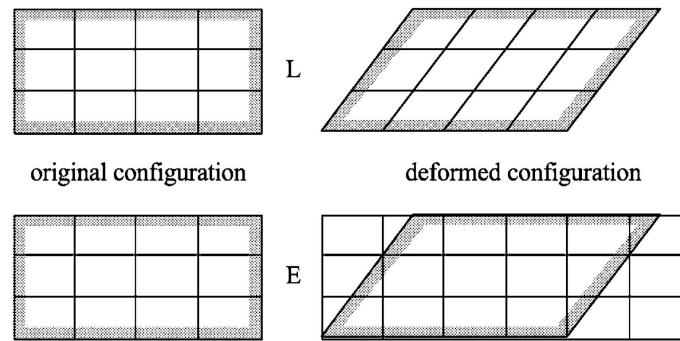


Figure 2.6: Comparison of a 2D mesh undergoing shear deformation for Lagrangian (L) and Eulerian (E) elements. Taken from [Belytschko et al. \(2014\)](#).

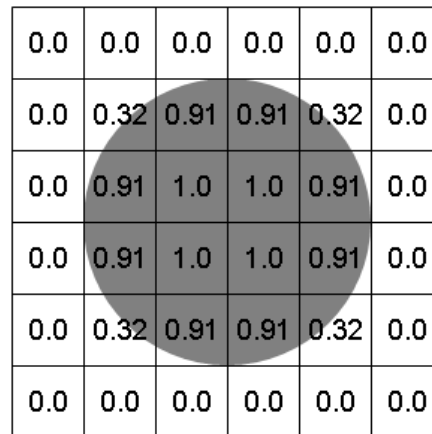
To calculate the material flow through the mesh, a two-step algorithm can be used. In an explicit FEA using an Eulerian mesh, first a typical Lagrangian calculation is performed for each time increment to obtain deformations, and the mesh and material distorts. In the next step the material flow through the mesh is calculated and the mesh is remapped to its original configuration. The analysis can then continue to its next time increment. This method is employed in the Abaqus FEA software ([Abaqus, 2019](#)). A comprehensive description of Eulerian and Lagrangian mesh formulations together with the finite element method is given in [Belytschko et al., 2014](#).

Another important difference between Eulerian and Lagrangian meshes is that the quadrature points remain coincident with material points in the Lagrangian mesh, whereas in the Eulerian mesh the material point at a given quadrature point varies with time. This makes it more difficult to track the state parameters of the material throughout the analysis, and if a constitutive model relying on state parameters are used, this needs special considerations. Abaqus offers automatic tracking of state parameters within the material, and no user intervention is needed for this.

In geotechnical problems involving soil-structure interaction a coupled Eulerian-Lagrangian (CEL) approach, which can benefit from advantages of both types of meshes, is a convenient approach. The structure is then modelled with a Lagrangian mesh, and the soil with a Eulerian mesh so that the soil can deform around the structure. With this method the Lagrangian structure occupies a void region in the Eulerian soil, and rigid body movement of the Lagrangian body through the Eulerian soil is allowed. The interaction between the Eulerian and Lagrangian

surfaces is handled by a contact algorithm that enforces no material flow into the area occupied by the Lagrangian body. Thus, the interaction between the soil and the structure can be well defined.

Eulerian elements can be fully, partially or not filled with material. In Abaqus this is handled with Eulerian volume fractions (EVF). An element which is filled has an EVF of 1 and an empty element has EVF of 0. Furthermore elements can contain several materials, and if an element has EVF sum of less than 1 the remainder of the element is filled with void-material. The void material does not have strength or mass. An illustration of how EVF is computed is given in Figure 2.7. The circular part with grey material is placed in an Eulerian mesh, and the corresponding Eulerian volume fractions to the grey material is shown for each element. Notice that when using EVF this circular part can be described by regular squared elements without using curved elements.



0.0	0.0	0.0	0.0	0.0	0.0
0.0	0.32	0.91	0.91	0.32	0.0
0.0	0.91	1.0	1.0	0.91	0.0
0.0	0.91	1.0	1.0	0.91	0.0
0.0	0.32	0.91	0.91	0.32	0.0
0.0	0.0	0.0	0.0	0.0	0.0

Figure 2.7: Illustration of Eulerian volume fractions for a circular part. Taken from [Abaqus \(2019\)](#).

For the contact formulation Abaqus\Explicit, which is used herein, uses a "general contact" algorithm to model the interaction between Eulerian and Lagrangian meshes. This algorithm uses the penalty method where an automatically calculated penalty stiffness relates the contact force between the Lagrangian structure and the Eulerian material to the penetration distance of the Eulerian material into the structure ([Abaqus, 2019](#)). This algorithm ensures that there are no Eulerian material flow into the volume occupied by the Lagrangian mesh.

The CEL approach has been used and validated for geotechnical problems in several publications. [Qiu et al. \(2011\)](#) tested the CEL approach on a benchmark bearing capacity problem and for installation of a pile. [Tho et al. \(2012\)](#) used CEL to analyse spudcan penetration, [Dutta et al. \(2015\)](#) to analyse the penetration of seabed pipelines and [Kim et al. \(2015\)](#) to analyse the in-

stallation of torpedo anchors in clay. In these publication the FEA results were validated against theoretical, numerical, or centrifugal test results or against a combination of these. They all concluded that the CEL approach gave results in good agreement with the validation data. Thus, the CEL approach is well suited for geotechnical analyses involving large deformations which are difficult to analyse with convectional Lagrangian FE-methods.

2.6.2 Explicit dynamic analysis

All finite element analyses (FEA) for this thesis are using an explicit dynamic solution method in the finite element (FE) program Abaqus. The problem is discretised in increments of time Δt_i , and the equation of motion is integrated using the explicit central difference integration rule such that the velocity solution $\dot{u}_{(i+\frac{1}{2})}$ at time $t_i + \Delta t/2$ and displacement solution $u_{(i+1)}$ at time $t_i + \Delta t$ is obtained with the following equations (Abaqus, 2019):

$$\begin{aligned}\dot{u}_{(i+\frac{1}{2})} &= \dot{u}_{(i-\frac{1}{2})} + \frac{\Delta t_{(i+1)} + \Delta t_{(i)}}{2} \ddot{u}_{(i)} \\ u_{(i+1)} &= u_{(i)} + \Delta t_{(i+1)} \dot{u}_{(i+\frac{1}{2})}\end{aligned}\tag{2.11}$$

Thus the acceleration $\ddot{u}_{(i)}$ at time t_i is used to advance the solution forward in time. The subscript i refers to the increment number in the analysis and u is one degree of freedom (DOF) in the analysis.

As the central difference method is using known quantities from the previous increment, i.e. $\dot{u}_{(i-\frac{1}{2})}$ and $\ddot{u}_{(i)}$, to advance the solution it is called an explicit method, therefore the equation of motion is only satisfied at the start of the increment and not necessarily satisfied at the end of the increment. Thus this is an approximate numerical method, but the method will provide an accurate and stable solution provided that the time increment is sufficiently small.

Abaqus is using a lumped mass matrix \mathbf{M} which makes \mathbf{M} become diagonal. The mass matrix is used to calculate $\ddot{u}_{(i)}$ as

$$\ddot{u}_{(i)} = (\mathbf{M}^{-1})_{kk} \cdot (F_{(i)} - I_{(i)})\tag{2.12}$$

where $(\mathbf{M}^{-1})_{kk}$ is an element on the diagonal in the inverted mass matrix \mathbf{M}^{-1} corresponding to the DOF u . F and I are the external and internal force applied to the DOF, respectively. As the mass matrix is diagonal, \mathbf{M}^{-1} is easily computed and this makes this method computational efficient. To initiate the solution algorithm $\dot{u}_{(-\frac{1}{2})}$ must be defined as this quantity is not explicitly

known from the initial conditions. Therefore it is obtained as

$$\dot{u}_{(-\frac{1}{2})} = \dot{u}_{(0)} - \frac{\Delta t_{(0)}}{2} \ddot{u}_{(0)} \quad (2.13)$$

The central difference method is conditionally stable meaning that the time increment must be sufficiently small to obtain a stable solution. The stability limit is calculated as

$$\Delta t \leq \frac{2}{\omega_{max}} \left(\sqrt{1 - \xi_{max}^2} - \xi_{max} \right) \quad (2.14)$$

where ξ_{max} is the fraction of critical damping in the mode with the highest frequency and ω_{max} is highest eigen-frequency in the system. However, Abaqus is equipped with a fully automatic incrementation scheme which calculates appropriate time increments during the analysis and no user intervention is required for this scheme. A more detailed description of this explicit dynamic solution method is given in the Abaqus Theory Guide (Abaqus, 2019) and in Chopra (2012).

2.6.3 Computational Time

There are several factors affecting the computational time for explicit FE-Analyses. The most prominent effect is from mesh size and density as in any other FEA, where an increased number of elements give increased computational time. Furthermore, for explicit analyses an increased number of elements giving smaller elements will also give a smaller stable time increment. This is because the element size affect the eigen-frequency of the element, and the eigen-frequency is directly linked to the stable time increment through eq. (2.14). Also for FEA using a dynamic explicit solution scheme the duration in time of each analysis step (step-time) needs to be specified. The step-time must be large enough to describe the given problem, e.g. to give the wanted spudcan penetration depth, and it is proportional to the computational time. Thus the penetration velocity of a spudcan affects the computational time, and it is approximately proportional to the inverse of the spudcan penetration velocity (Tho et al., 2012). The rigidity index (E/s_u) also affects the computational time since the stable time increment is dependent on the inverse of the rigidity index, and more time increments are needed when the rigidity index increases. Factors affecting the computational time for dynamic explicit FE-analyses are discussed in more detail in Tho et al. (2012).

2.6.4 Filtration of Noise in Finite Element Analyses

Due to the numerical scheme used in dynamic explicit analyses in Abaqus\Explicit, the results from the analyses, e.g. load-penetration response, may contain noise, and Abaqus offers several filters which can remove or decrease the amount of noise in the data. In this thesis the Butterworth filter is considered.

The Butterworth filter is one of the most widely used filters, and can be used to remove high frequency response in a dataset. See e.g. [Tseng and Lee \(2017\)](#). The filter is described by the magnitude-frequency response function $H(\omega)$ in the frequency domain:

$$H(\omega) = \frac{1}{\sqrt{1 + \left(\frac{\omega}{\omega_c}\right)^{2n}}} \quad (2.15)$$

where

- ω – sampling frequency of the data
- ω_c – cut-off frequency
- n – filter order

A plot of the frequency response function given in eq. (2.15) is shown in Figure 2.8. The figure shows that the magnitude of the frequencies above the cut-off frequency is approaching zero, and thus these frequencies are filtered out of the data. The transition from a magnitude of one to where the frequency response tends of to zero is reduced with increasing filter order. This filter can be applied to FEA results, and is integrated in Abaqus\CAE where it can be directly applied in the post-processing of results. The Butterworth filter is also described in the [Abaqus \(2019\)](#) user manual.

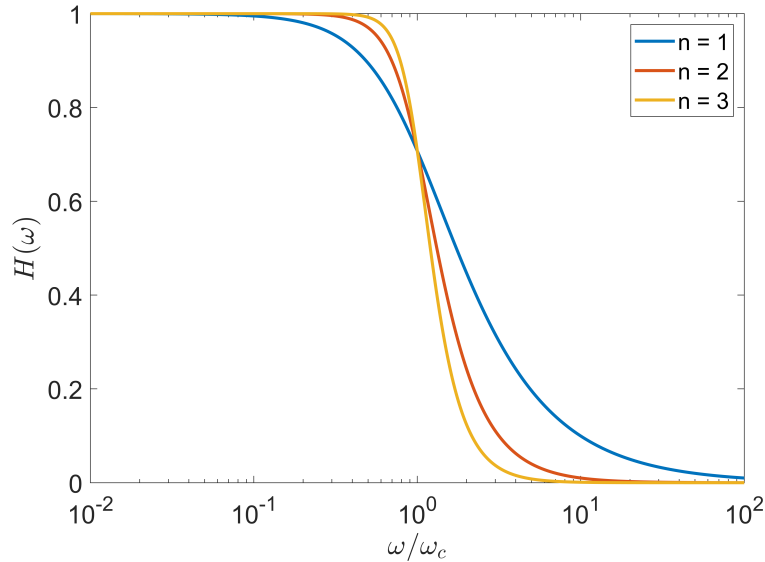


Figure 2.8: Frequency response function used in the Butterworth filter plotted for three different filter orders.

2.7 Lateral capacity of Monopiles and Rate Effects

Monopiles are large diameter piles, typically made of circular steel tubes (DNV GL, 2018), with a relatively shallow embedment depth L with typical length-to-diameter ratios (L/D_p) from 2 to 6. D_p is denoting the monopile diameter and in current monopile design D_p may be 8 m. Monopiles differ from regular slender pile design much used in the petroleum industry and for onshore foundations where the L/D_p ratio may be in the order of 40 (Byrne et al., 2020). In later years there has also been a trend of steadily increasing monopile diameters. E.g. Randolph and Gourvenec (2011) is reporting that monopile diameters can go up to 4 m, thus this literature indicates that typical diameters have doubled during the last decade.

This increase in monopile diameter is due to the steadily increasing size of offshore wind turbines (OWT) as they are continuously optimised and monopiles are the most used foundation type for OWTs (WindEurope, 2021). Monopiles offer a simple design where the tower can be supported by one monopile fabricated in one piece. Monopiles are the adopted foundation type at the Dogger Bank Wind Farm.

Pile design methodology and requirements for laterally loaded piles are described in DNV GL documents standard ST-0126 and recommended practice RP-C212 (DNV GL, 2018; DNV GL, 2019). The most common method for assessing the lateral capacity of piles is the so-called p - y method (Randolph and Gourvenec, 2011). This method uses p - y curves which gives the relation between the lateral mobilised resistance per unit length of pile from the soil onto the pile (p),

and the lateral displacement of the pile (y). However this method was principally developed for long slender piles in soft clay (Byrne et al., 2020), and special considerations are needed when such p - y curves are to be used in monopile design. DNV GL (2019) recommends that such p - y curves should be verified with alternative analyses such as FE-analyses, when applied to monopiles.

The reason that p - y curves developed for longer slender piles should not be directly applied to monopiles is due to their different response to lateral loading, as illustrated in Figure 2.9. Monopiles with a typical low L/D_p ratio will rotate more like a rigid body around a rotation point at a depth z_{crit} below the seabed, mobilising a passive earth pressure in front of the pile and an active earth pressure behind the pile, similar to a retaining wall. Whereas a longer slender pile with a large L/D_p will bend such that the lower region and tip of the pile is stationary, thus the soil resistance will be mobilised in a different manner. Due to the difference in response the current p - y methods appear to underestimate the strength and stiffness of laterally loaded monopiles (Zdravković et al., 2020a).

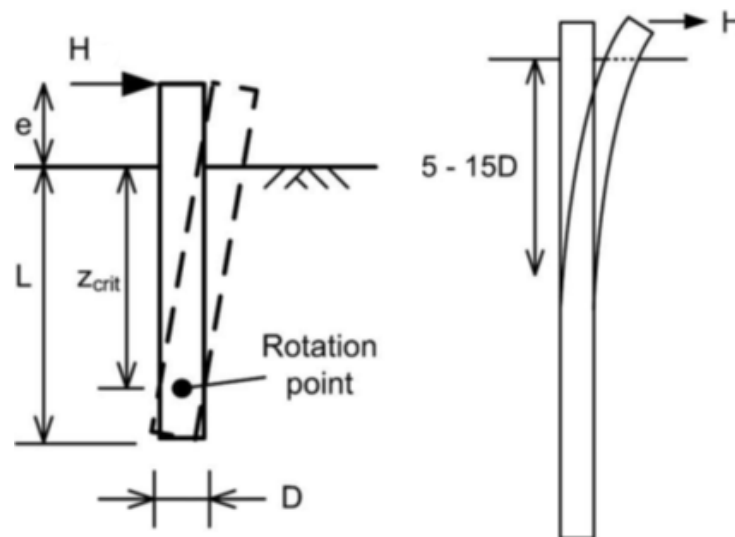


Figure 2.9: Comparison of pile response to lateral loading H for a short (left) and long (right) pile. In the figure D is referring to the pile diameter. Adapted from Randolph and Gourvenec (2011).

As monopiles have become a widely used foundation solution for OWTs, research has been carried out investigating the lateral capacity of monopiles. Recently several publications from the PISA (Pile–Soil Analysis) joint industry project was published, see e.g. (Zdravković et al., 2020a; Byrne et al., 2020; Zdravković et al., 2020b). The PISA project has studied the lateral response of monopiles and one of the main goals was to develop an enhanced p - y method

suitable for monopiles. However, the PISA p - y method is not further discussed here. In the PISA project lateral load tests were carried out on piles with L/D_p ratios relevant for monopile design which in turn were used to verify high quality FEA (Zdravković et al., 2020b). The tests were carried out onshore at two locations in dense sand and stiff clay, respectively. The locations were chosen such that the ground conditions should resemble soil conditions typically found in the North Sea. During the PISA project some investigation into how rate effects affect the lateral capacity of monopiles was also done, providing some very relevant results for this thesis.

The main objective of the PISA project was to study monotonic lateral loading of monopiles, and the field test was originally designed to have sufficiently low loading rates to avoid rate effects. However, during one of the tests in stiff clay the loading rate was unintentionally increased with a factor of 510, and resulted in a 90% increase in pile capacity, equivalent to a 33% increase in strength per log-cycle of loading rate. Therefore an additional field test was carried out where the loading rate was varied between a slow and fast rate during the test. The ratio of the fast rate to the slow rate was 260, and this resulted in a 20% load increase during the fast phases, equivalent to about 8% increase per log-cycle of loading rate. Thus a clear rate effect was observed in these test, but as the strength increase due to the rate effect differed significantly in the two tests it is uncertain how large the rate effect will be in practical applications. A more detailed description of these tests is given in Byrne et al. (2020).

Design criteria for monopiles in combined lateral and moment loading are given in DNV GL (2019). In a simplified form they read:

1. The sum of the lateral resistance over the pile length shall not be less than the design lateral load applied at the pile head.
2. The lateral displacement at the pile head shall not exceed some specified limit.

The first requirement is, as in any other design, stating that the design resistance needs to be larger than the design load. The second requirement is a more practical requirement, where the deformation tolerances are governed by visual and operational needs for wind turbines. The limiting condition for monopiles is most often governed by overall deflections and vibrations (DNV GL, 2018). Furthermore, the displacement limits are project dependent and must be assessed for the specific monopile design.

Wind turbine supporting monopiles are subjected to natural lateral wind and wave loading. These loads are cyclic in nature, and cyclic effects should be accounted for in design. Cyclic

loading on a monopile leads to the development of cyclic shear stresses in the soil, which may lead to a gradual pore pressure buildup and buildup of cyclic and permanent shear strains. This may lead to a reduced soil shear strength called cyclic degradation effects (DNV GL, 2019). In practise cyclic degradation effects on soil strength and stiffness needs to be accounted for when determining the lateral resistance of monopiles. However, cyclic degradation effects are not considered for this thesis, and the subject is not further discussed.

For design in the serviceability limit state (SLS) design criteria no. 2 is important. For example, design must ensure that the accumulated deformation after a storm or during the life time of the structure is acceptable. In such a storm requirement no. 1 can also be challenged if a particularly large wave hits the monopile. Then the structure may find itself in the ultimate limit state (ULS) where one wave may impose a lateral load exceeding the lateral capacity of the monopile. In such a design case the soil resistance may be mobilised in the matter of seconds during one wave period, which will result in significant strain rates in the soil. Therefore, it may be appropriate to include strain rate effects in the resistance instead of only considering the static resistance. As previously shown, strain rate effects may give a significant increase in the lateral capacity.

Note that currently monopile design is most often governed by SLS requirements on overall displacements, but as monopile design is continuously optimised ULS requirements may become governing. Then, if strain rate effects can be utilised in design, monopile design can be further optimised and production costs may be reduced.

Chapter 3

Triaxial model – Material Model Verification

To test the performance of the UWA soil model in the finite element method with the coupled Eulerian-Lagrange (CEL) approach, a triaxial compression test is modelled in Abaqus\Explicit. The effect of different FE-model and soil-model parameters is investigated. However, it is not sought out to model the response of a real soil, but rather to check the performance of the current FE methodology and soil model.

3.1 FE-model for Triaxial Test and Model Verification

The objective of the model is to simulate an undrained triaxial compression test on an isotropically consolidated standard 54 mm diameter clay sample. As the material is modelled as undrained and the shear strength is prescribed in the analysis, there is no need to model a confining pressure. Thus this model is principally a uniaxial test. Similar analyses have also been conducted in a Master's thesis by [Worren \(2013\)](#), but with a different soil model.

The triaxial model consists of a clay sample with a diameter of 54 mm and a height of 100 mm and a rigid bottom and top plate. The soil is modelled with 8-node linear Eulerian brick elements with reduced integration and hourglass control, named EC3D8R in the Abaqus element library. An additional layer of initially void elements are added around the soil to accommodate radial soil expansion during the test. The plates have a diameter of 80 mm, and are modelled as rigid bodies (RBs) with a Lagrangian mesh. The elements used for the plates are 8-node linear brick elements, also with reduced integration and hourglass control (C3D8R). Each plate is meshed with 4 674 elements with an average side length of 1,75 mm. The interaction between the plates and the clay is modelled as hard with a fully rough friction formulation such that no

slip will occur between the soil and the plate when they are in contact. This interaction is handled by the "general contact" algorithm available in Abaqus which uses a penalty method as described in section 2.6.1. The model and an example of an FE-mesh is shown in Figure 3.1.

During the test the Lagrangian RB top plate is given a constant vertical velocity such that the soil below is compressed and deforms in the Eulerian mesh. Furthermore, the required force on the top plate, denoted F , is measured. The bottom plate is fixed in space, and the top plate is only allowed to move vertically. The analysis is executed with the dynamic explicit solver in Abaqus. To avoid large accelerations in the initial part of the analysis an amplitude function $A(t)$ is prescribed on the vertical velocity of the plate for the first second of the analysis time t , such that the current velocity is equal to the final velocity times $A(t)$. The amplitude has the following expression:

$$A(t) = \sin\left(\frac{t\pi}{2s} - \frac{\pi}{2}\right) + 1 \quad \text{where } t \in [0, 1 \text{ s}] \text{ and } s \text{ is seconds} \quad (3.1)$$

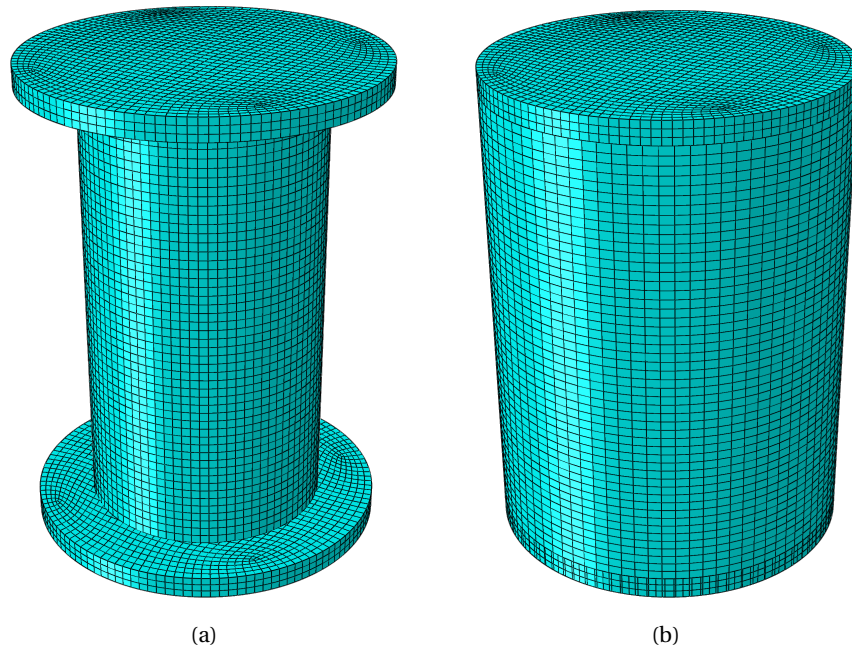


Figure 3.1: FE-model used for the triaxial test discretised with Mesh2. (a) showing clay sample and plates, and (b) showing the entire model with initial void region.

The material model used for the clay is the UWA-model as described in section 2.4.1, and is implemented in Abaqus as a user-defined material model, VUMAT. The soil density ρ was set to an artificially high value of $9 \times 10^7 \text{ kg/m}^3$ to reduce the computational time of the analysis. The stable time increment, which is proportional to the computational time, is inversely proportional to the square root of the density, thus by increasing ρ with a factor of f^2 the computa-

tional time is reduced by a factor of $1/f$ (Abaqus, 2019). This concept is known as mass scaling, and is an attractive method for analyses involving rate dependent materials since the mass scaling reduces the computational time without affecting the strain rates in the analysis. The mass scaling is believed to have an insignificant effect on the analysis results. This can partially be verified by inspecting the kinetic energy of the model.

Since a physical triaxial test is essentially quasi static in nature but a dynamic explicit solution scheme is used in the FE-modelling, care must be taken to ensure that no unrealistic dynamic effects influence the analysis results. E.g. unrealistic inertia forces from the increased soil density may give an unwanted effect on the results, but such forces will also give increased kinetic energy in the model. By checking that the kinetic energy is small compared to the internal energy of the model (i.e strain energy and plastic dissipation in the soil etc.) it can be verified that the dynamic analysis behaves like a quasi-static analysis.

First the effect of mesh density and compression velocity is investigated. For the soil material an undrained shear strength of 50 kPa, a sensitivity of 2, an elastic modulus of 10 MPa and a Poisson's ratio of 0.495 is used. The parameter of required plastic shear strain for 95 % remoulding, ξ_{95} , is set to 100 %. These material parameters are used in all triaxial FEA unless otherwise stated. No rate effects are considered for the initial analyses, i.e using η equal to zero. Three different meshes are considered and three different compression velocities. The meshes considered for the Eulerian region are tabulated in Table 3.1, and the considered compression velocities are 0,2 mm/s, 1,0 mm/s and 2,0 mm/s. A compression velocity of 1 mm/s is used for the mesh checks. The mesh for the plates is kept constant. In the post-pressing, the deviator stress q is calculated as F divided by the initial clay area, A , and the axial strain, ε_a , as the vertical displacement of the top plate divided by the initial height of the clay sample ($\Delta L/L_0$). The resulting stress (q) - strain (ε_a) curves from initial tests on mesh density are shown in Figure 3.2(a).

Table 3.1: Meshes considered for the soil domain in the triaxial model

Name	No. of elements	Average element length [mm]
Mesh1	19 656	3,0
Mesh2	65 826	2,0
Mesh3	160 512	1,5

The curves corresponding to Mesh2 and Mesh3 are practically identical, thus the model has converged for Mesh2. The response from the model with Mesh1 shows some problems. The

curve is initially horizontal which might be due to how contact between the sample and the plate is modelled. Since the element length is larger for Mesh1 than for the other meshes the plate has to move further into the top Eulerian elements before the FE-program recognises the contact between the sample and the plate. Furthermore the response in the elastic domain is not a straight line, which would be expected, but q is varying up and down before first yield. This might be because the plate-sample contact is not recognised in the first part of the analysis, thus the intended gradual acceleration of the soil sample with the amplitude function is not achieved since the plate already has a velocity when the contact is recognised. This might cause the initial oscillations in the elastic domain for Mesh1.

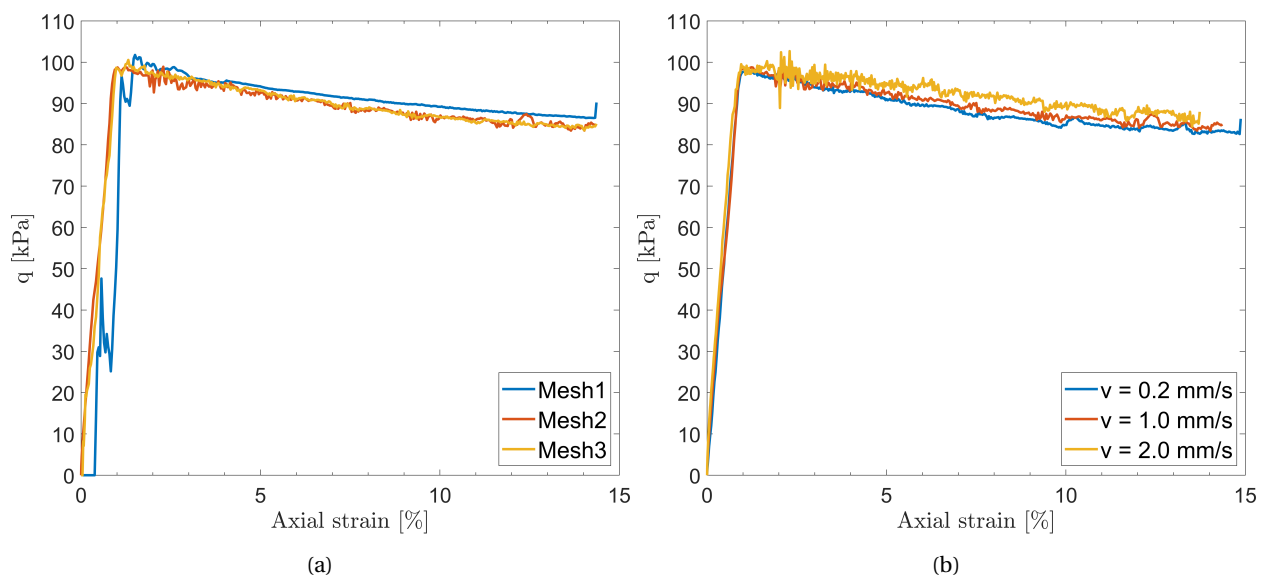


Figure 3.2: Deviator stress, q , versus axial strain, ϵ_a , obtained from FE-analyses of a triaxial compression test showing (a) the effect of mesh density in the Eulerian domain and (b) the effect of compression velocity using Mesh2.

The effect of compression velocity on the stress-strain curves is shown in Figure 3.2(b). The curves corresponding to a compression velocity of 1,0 mm/s and 0,2 mm/s are very similar, furthermore the kinetic energy in the model with a compression velocity of 1 mm/s is well below 5 % of the internal energy for most of the analysis time. Only in the first 1-2 seconds of analysis time, where the internal energy is still small, is the kinetic energy in the same order of magnitude as the internal energy. If the kinetic energy is less than 5-10 % of the internal energy, the dynamic analysis should behave as quasi-static (Abaqus, 2019). Thus using a compression velocity of 1 mm/s does not give any significant unrealistic dynamic effects and should give sufficient accuracy. Doubling the compression velocity to 2 mm/s gives in the order of 3 % higher stresses after yielding. A compression velocity of 1 mm/s will be used for further analyses.

The internal distribution of stresses and strains inside the model is also of interest to validate the model. Contour plots of equivalent plastic shear strain, ξ , and equivalent Tresca stresses, σ_{eq} ($= \sigma_1 - \sigma_3$), for the different meshes are shown in Figure 3.3. The figure shows stresses and strains after yielding and subsequent failure, and all the soil is fully mobilised with σ_{eq} at 100 kPa, which is equal to $2s_u$, or less due to softening decreasing the s_u . An exception to this is the soil close to the plate which is not mobilised due to the confining shear stresses exerted by the rough plates. By considering the contours of equivalent plastic shear strain it is evident that the failure has localised, and it is seen that the the equivalent stresses has decreased in the areas with strain localisation due to strain softening. Furthermore, there is a more pronounced failure mechanism in the two most refined meshes than in the coarsest mesh with failures and strain localisation in bands at approximately 45° . The plots from Mesh2 and Mesh3 are practically identical, thus this figure also indicate that the model has converged for Mesh2, and for the further analyses Mesh2 is used.

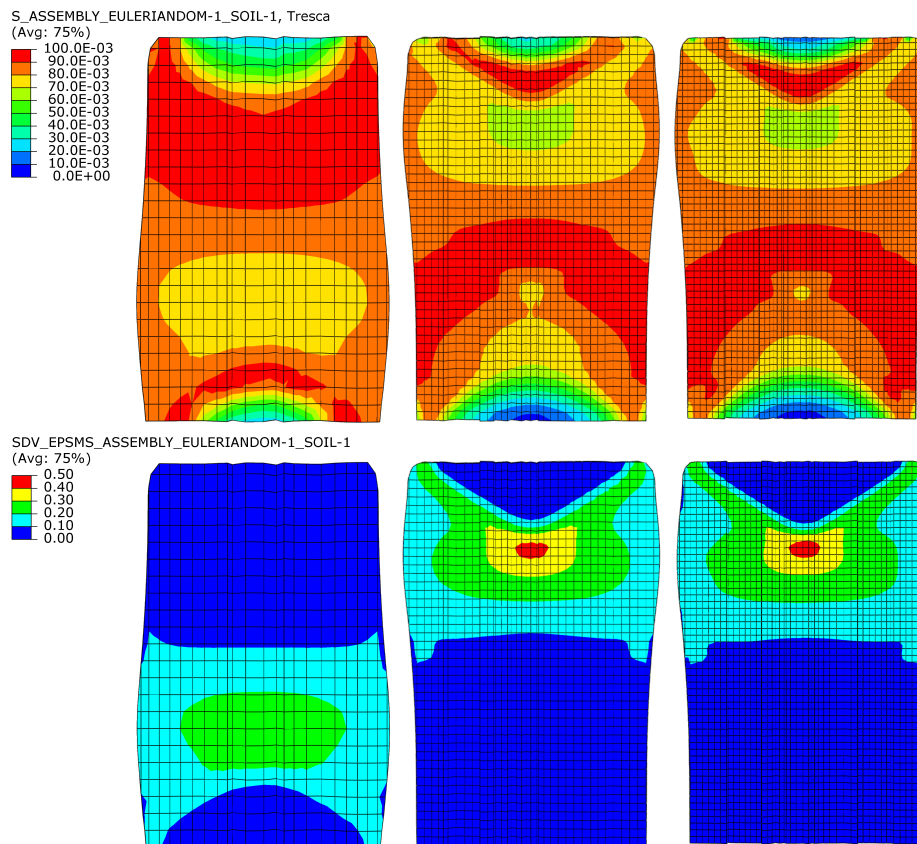


Figure 3.3: Contour plots of equivalent Tresca stresses (top row) and cumulative plastic shear strain, ξ , (bottom row) on a vertical cut trough the centre of the soil sample. Mesh1, Mesh2 and Mesh3 are shown from left to right at 9,9 % axial strain. Stresses in MPa and strains are dimensionless.

3.2 Triaxial Model - Soil Model Verification

Several analyses has been undertaken to study the performance of the softening and rate effects available in the UWA-model. In the FE-model a compression rate of 1 mm/s and Mesh2 is used. E and s_u is set to 10 MPa and 50 kPa respectively, as used in the FE-model verification.

The effect of softening is studied by considering an analysis where the sensitivity is set to a high value of 10, denoted "sensitive", and an analysis where ξ is set to a low value of 0.1, denoted "brittle". No rate effects are considered for these analyses, i.e using $\eta = 0$. The stress-strain response from these analyses are shown in Figure 3.4(a) together with a base case analysis with S_t and ξ equal to 2 and 1,0 respectively. As expected the brittle analysis shows a brittle behaviour where the resistance, represented by q , quickly reduces to almost $2s_{u,r}$ which for the brittle curve is 50 kPa. This is due to the low value of ξ_{95} , thus little plastic shear strain is required to remould the clay. In the sensitive analysis the loss of resistance is also much more pronounced compared to the base case, as expected. This is due to the low value of the remoulded shear strength, which is equal to 5 kPa for the sensitive analysis.

None of the stress strain curves softens enough for the resistance (q) to reach the remoulded strength ($2s_{u,r}$). This is because the axial strain is not large enough for the material to reach the remoulded strength or this only happens in a small part of the clay sample, thus the overall strength of the sample is not reduced to the remoulded strength. Furthermore, no area corrections are used in the calculation of q , resulting in an artificially high q value when the axial strain is increasing. This is described in more detail later in this subchapter.

In the elastic range before yielding all the curves coincide which also is expected, as the material parameters which is being varied only affect the plastic behaviour after yielding. By fitting a linear regression line to the initial elastic response the rate of increase is obtained as 10,2 MPa which should be equal to the elastic modulus, E , of the clay, see section 2.3. The prescribed value of E is 10 MPa and therefore agrees well with the measured value of 10.2 MPa. The difference may be explained by the fact that the stress strain curve is obtain by post processing of the data from the analysis, and small errors may have been introduced when q and ε_a is calculated. Additionally FEA using the CEL-method involve much complexity and the FE-solution itself may contain small errors.

To investigate the rate effect present in the UWA-model, additional analyses were undertaken where the soil sample is compressed at different rates. To model different compression

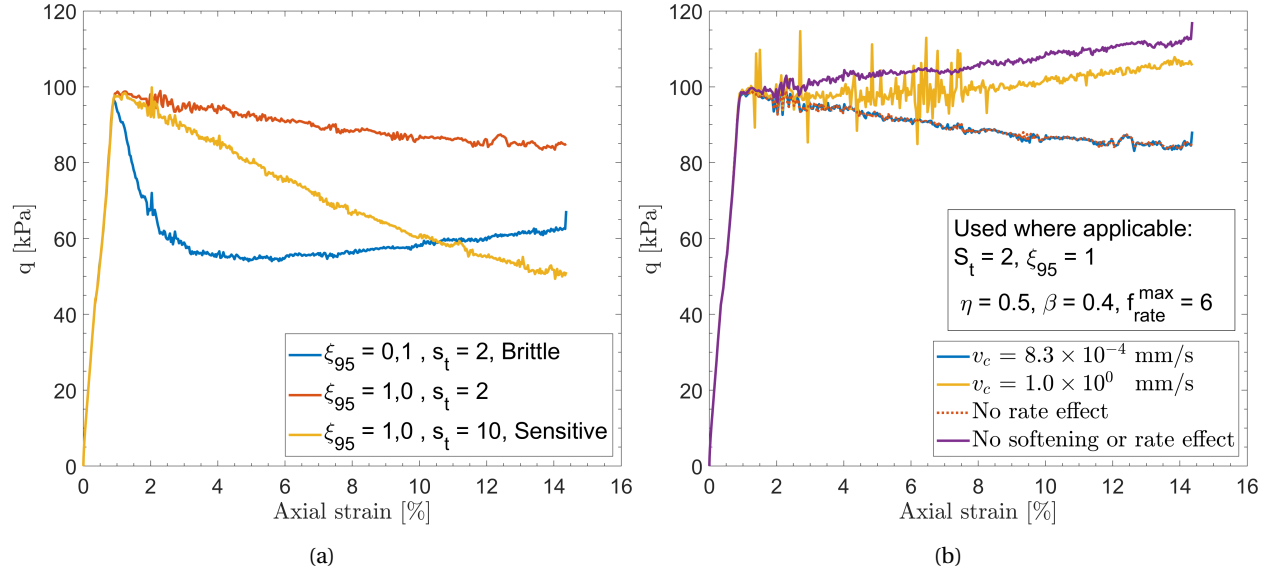


Figure 3.4: Deviator stress, q , versus axial strain, ϵ_a , obtained from FE-analyses of a triaxial compression test showing (a) the effect of the softening parameters ξ_{95} and S_t and (b) the response of rate effects.

velocities the approach described in section 2.4.2 is used where the normalised velocity, v_n , is calculated as

$$v_n = \frac{v_c}{\dot{\gamma}_{ref} D_s}$$

where v_c is the compression velocity in the triaxial test, D_s is the soil sample diameter and $\dot{\gamma}_{ref}$ is taken as 3 %/hr. The compression velocity in the FE-model is kept constant and equal to 1 mm/s, and $\dot{\gamma}_{ref}$ is modified in the FEA to model the real compression velocity as previously described. As for the parameters controlling the rate effect in the UWA-model [eq. (2.4)] η is set equal to 0,5, beta equal to 0,4 and f_{rate}^{max} equal to 6,0. These values are later used in spudcan back-calculations.

Two different compression velocities, v_c , are considered. v_c equal to $8,3 \times 10^{-4}$ mm/s, corresponding to a triaxial compression test with a strain rate of 3 %/hr denoted "the slow test", and v_c equal to 1 mm/s denoted "the fast test". The stress-strain response from these analyses are shown in Figure 3.4(b). Additionally the base case analysis with no rate effects and an analysis without softening or strain rate effects are included in the figure. The curve corresponding to the base case analysis is included in both Figure 3.4(a) and 3.4(b) and have the same orange colour.

From Figure 3.4(b) it is evident that larger compression velocities give larger resistance when strain rate effects are accounted for. The deviator stress from the fast test is increased with 26 % compared to the slow test at 14 % strain. The slow test and the tests without rate effect are

identical meaning that the slow test gave no rate effect. This is reasonable as the slow test had a compression velocity which gives strain rates in the same order of magnitude as the reference shear strain rate. Thus the elements of the model can be expected to have values of f_{rate} close to one during the analysis. Moreover, f_{rate} can be calculated by the increase in resistance for the individual triaxial tests. E.g the fast test had an approximate increase of 26 % in resistance due to rate effects which gives $f_{rate} = 1,26$, and the simulated axial strain rate is 3600 %/hr. This result can be compared to the NGI rate equation (2.3) which is based on several real triaxial tests. Both the FEA of the triaxial tests which included strain rate effects are plotted together with the NGI rate equation in Figure 3.5, and both FEA gave rate effects close the real measurements. Thus, the rate effect parameters used in the FEA give a rate effect similar to empirical measurements.

There is great deal of oscillation in the response from the fast test, which is likely due to the large rate effects present in the fast test analysis. The rate effect in an element is given by the strain rate of the soil in the element. As this analysis is using an explicit solution scheme the strain rate is calculated from the deformation in the previous time increment. If the previous increment gave a low strain rate for an element this element will get a low rate effect and strength in the next increment. Therefore, this element will tend to deform more in the next time increment, resulting in a higher strain rate and rate effect in the following increment. Thus, as the dynamic equilibrium is solved time step by time step the explicit solution goes through cycles where the resistance is under- and overpredicted giving an oscillating behaviour, caused by the nonlinear behaviour of the rate effect.

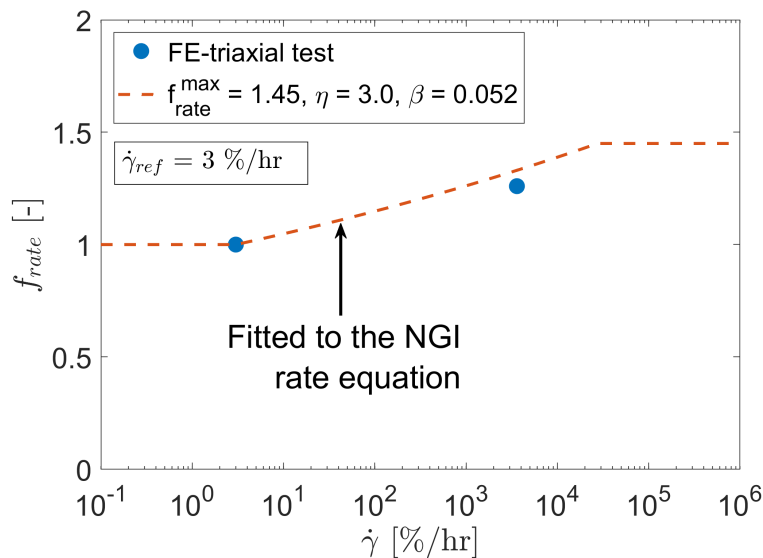


Figure 3.5: Comparison of strain rate effects measured in real and in FE-simulations of a triaxial compression test.

Another property of the fast test curve that warrants an explanation is the increasing resistance with increasing strain after the initial failure. The test with no softening or rate effects shows the same behaviour. A triaxial compression test on an elastic - perfectly plastic soil sample obeying the Tresca yield criterion, as is the case for the analysis without softening or rate effect, should have constant deviator stress of $2s_u$ after failure, see section 2.3. Thus, q should not increase with increasing strain. The reason this is the case in the current response is that when the sample is axially compressed it will expand radially as the material is incompressible, thus increasing the sample area (A). Therefore the available resistance force (Aq) will also increase. To account for this, area corrections can be used to modify A when calculating q , however this has not been done here, and it is the reason q is increasing with strain after initial failure. It has been verified that using an area correction would have given an almost constant q after the inertial failure for the test with no softening or rate effects. Therefore the other tests can be compared to the test with no softening or rate effect to evaluate how large these effects are without the comparison being disturbed by the missing area correction. The fast test with considerable rate effect shows less resistance than the test with no softening or rate effects. This is because softening is also included in the fast test thereby lowering the resistance.

To give further insight into the performance of the triaxial FE-model various contour plots from the FEA is illustrated in Figure 3.6. The contour plots are showing cumulative plastic shear strain, ξ , Tresca stresses, the softening effect as f_{soft} and the rate effect as f_{rate} for the test with no rate or softening effects, the fast test and for the brittle test. f_{soft} , f_{rate} and ξ are described in section 2.4.1. In general the deformed shape and internal stresses and strains seems to be in line with what can be expected for a real triaxial compression test. E.g. consider the test with no softening or rate effect where all the clay, except close the plates, are fully mobilised with Tresca stresses equal to $2s_u$ ($= 100$ kPa), and a symmetric failure pattern can be seen in the plot of ξ .

From the plots of ξ it is seen that the failure is localising with most of the straining developing in a shear zone for the tests which includes softening. This strain localisation is also observed in the plots of Tresca stresses. The test with no rate or softening effects has a uniform distribution of stresses while in the two other tests the stresses are lower in the regions which has strained the most due to softening reducing the material strength. This strain localisation is most prominent in the brittle test. See e.g. the plot of f_{soft} where almost all of the softening is localised in a shear zone in the top of the sample. The deformed shape of the samples also shows the strain localisation as the brittle test is bulging out only around the shear zone, while in the fast test and in the test with no softening or rate effect the deformation is more uniform over the sample

height.

The reason for this strain localisation is that when the sample starts to yield in an area increasing ξ , the material strength is reduced due to softening. This area will then have a lower strength and this area will continue to yield instead of other areas with higher strength. In other words this is a self-reinforcing effect.

Further inspection of the deformed shapes also shows that the rate and softening effect is counteracting each other since the deformed shape of the fast test, which also includes softening, is similar to that of the test with no softening or rate effects. The reason for this counteracting effect is that the softening is dependent on the accumulated plastic strain while the rate effect is dependent on the plastic strain rate. The rate effect will give the areas with high strain rate more strength and therefore they will develop less plastic strains and this material will soften less. Looking at this in the opposite way the material with much rate effect will soften as well and therefore the combined softening and rate effect will give a lower strength than what it would have had with only rate effects. Comparing the contour plot of ξ for the fast test with the same plot for mesh 2 in Figure 3.3, which is an identical analysis to the fast test except for the rate effect, it is seen that the strain localisation in the latter plot is more distinct than in the fast test.

Figure 3.6 also shows that the brittle test has a brittle behaviour with much softening. The plot of f_{soft} for the brittle test shows failure surfaces with approximately 45° inclination which should be the planes with maximum shear stress, and therefore this is as expected. For the fast test f_{rate} is plotted and shows how the strength-increase due to rate effects is distributed inside the sample. It is seen that the distribution is less uniform and more erratic because of the same reason as for the oscillating behaviour in the corresponding stress-strain curve, as described above. Some elements have f_{rate} close or equal to six, which is the maximum limit, while most of the sample has f_{rate} around one. This distribution is changing quickly between time increments. Even though a small part of the sample experiences a rate effect in a given time increment, the corresponding stress-strain curve [fig. 3.4(b)] from the analysis shows that in total the rate effect gives a considerable increase in strength for the sample as a whole. This seems reasonable because the overall strength of the sample is determined by the strength in the plane of shearing in the failure mechanism, and that seems to coincide with where there is most rate effect.

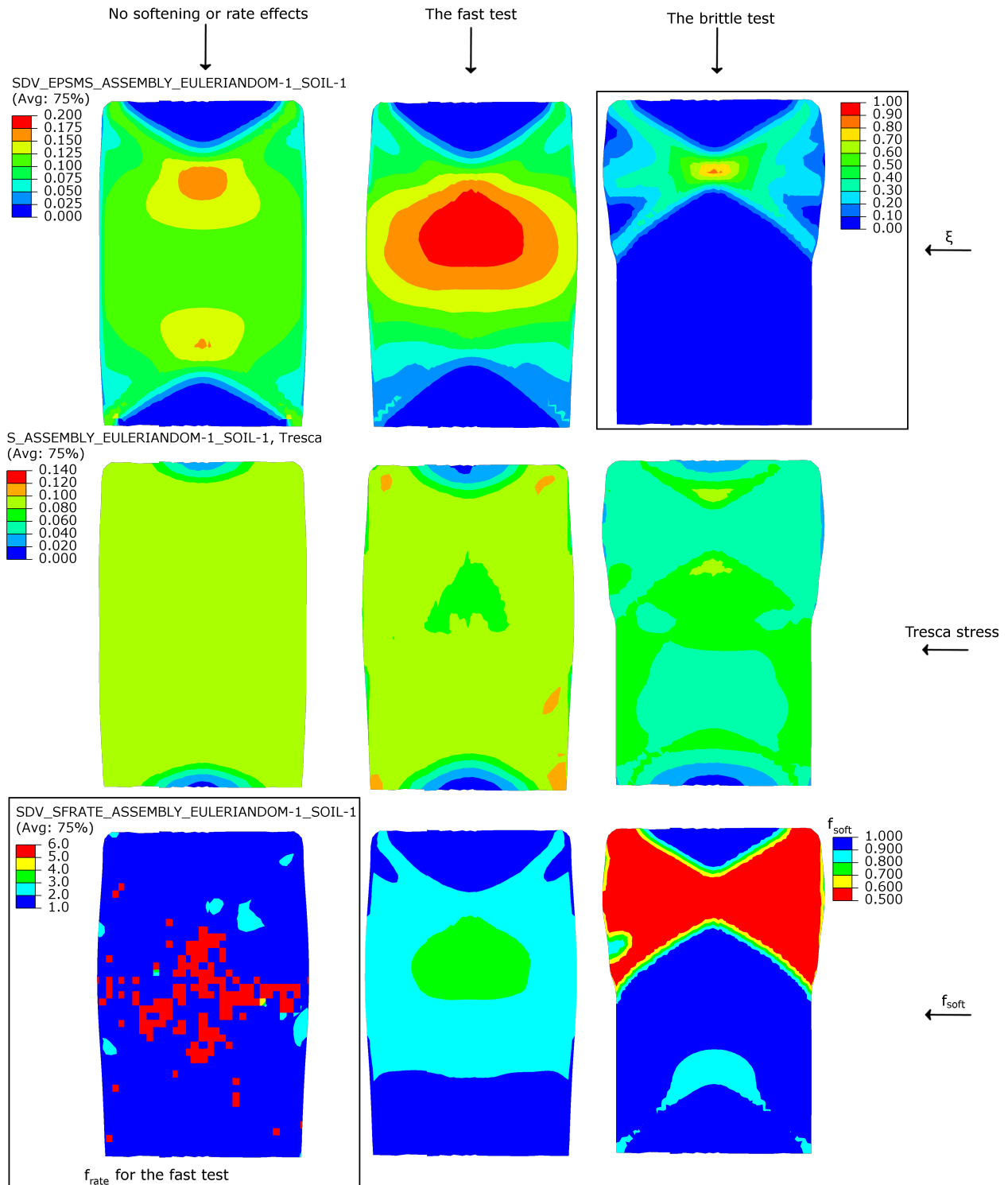


Figure 3.6: Contour plots of cumulative plastic shear strain (ξ), Tresca stress ($\sigma_1 - \sigma_3$), f_{soft} and f_{rate} from the test with no softening, the fast test and the brittle test at 9.9% axial strain. The contours are shown on a vertical cut through the centre of the soil sample. The layout of plots is indicated with arrows, and deviations from the layout are indicated with borders. Stresses in MPa.

3.3 Triaxial Model - Conclusion

This chapter describes the FE-simulations of an undrained triaxial compression test using coupled Eulerian-Lagrange (CEL) method. First an FE-model was established and a convergence study was carried out to obtain a mesh density and model compression rate which ensures that the FE-solution has converged sufficiently.

The softening effects available in the UWA-model was studied by running analyses where the sensitivity, S_t , and the parameter of required plastic shear strain for 95 % remoulding, ξ_{95} , was varied. It was found that these parameters had effects as expected and succeeded in modelling strain softening. The rate effect available in the model was studied by using a normalised compression velocity to vary the true compression velocity when rate effects were included. These analyses showed that this model was capable of accounting for rate effects, and that the rate effect behaved as expected with very little strength-increase for a slow compression velocity, and a considerable strength-increase for a large compression velocity. Furthermore, rate effect parameters calibrated against spudcan penetration tests were found to give a rate effect similar to rate effects observed in physical triaxial tests when applied to the FE-model. This indicates that using a normalised compression velocity to account for rate effects is a valid approach.

The presented results also showed that the rate and softening effect is counteracting each other and may prevent excessive strain localisation. Failure planes with an approximate 45° inclination were observed in the results, and the over all deformed shape of the samples seems to be as expected in a real triaxial test.

Some abnormalities were observed in the results, but explanations for these are given. Especially a missing area correction for the sample area and the contact formulation used to model the contact between the clay and the plates are reasons for some deviations in the results.

In general the UWA-model has been verified to work as expected to model strain rate and strain softening effects when used together with the finite element method and the CEL approach.

Chapter 4

Back Calculation of Spudcan Penetration

This chapter describes back-calculations of spudcan penetration tests from two locations at Dogger Bank (DB), where FEM is used with the Coupled Eulerian-Lagrange approach. First, the spudcan jacking trials carried out at Dogger Bank are described. Next, geotechnical parameters used in the analyses are discussed. Furthermore, a convergence study is undertaken to obtain a reliable FE-model for spudcan penetration, and this model is then used to back-calculate the spudcan penetration test. In the back calculations, the UWA soil model is used to account for softening and strain rate effects. The goal of this work is to obtain a framework for an FE-model together with reliable soil model parameters which can later be transferred to an FE-model of an overturning monopile.

Note that NGI have done similar back-calculations for the same spudcan tests as considered here, but strain rate effects were not considered in these back-calculations. The resulting report (NGI, 2020b) has been taken into account during the spudcan back-calculations for this thesis.

4.1 Dogger Bank Jacking Trials 2020

Note that the following text in this subsection (sec. 4.1) contains citation from the project thesis (Wahl, 2020) preceding this master thesis. The main part of this text is taken from the project thesis, but some text is added or changed.

Eight jacking trials were performed at six locations at the Dogger Bank development area in July 2020. The main objective of the trials was to better understand the operational undrained shear strength in fissured clays relative to large foundations such as for spudcan penetration and wind turbine supporting foundations. This is to complement the uncertainty in measured

strengths in the laboratory due to fissures in the clay. The jacking trials were carried out with the Vole Au Vent jack-up rig operated by Jan de Nul. Vole Au Vent is equipped with four legs and spudcans. The maximum pre-load on each leg that could be achieved with an empty ship was approximately 12 200 tonnes [≈ 120 MN] per leg.

Under normal spudcan pre-loading the spudcan load is increased stepwise, and additional load is added when the penetration rate reduces to a certain level, and is thus load-controlled and not displacement-controlled. However, the jacking system on Vole Au Vent was capable of continuous penetration such that a penetration rate could be held approximately constant, which was used to do fast penetration tests. For more detailed reports on the Dogger Bank jacking trials the reader is referred to the experience report by [Equinor \(2020\)](#) and the Jacking report by [Jan De Nul \(2020\)](#).

This thesis will look at results from two of the test sites, namely location DBB-JU1 and DBC-JU1, located at Dogger Bank B and Dogger Bank C, respectively. Both locations include fast penetration tests which is used to study rate effects in spudcan penetration. Coordinates and water depths for these locations are given in table [Table 4.1](#).

Table 4.1: Coordinates and water depth for spudcan penetration tests.

Location	Easting [m]*	Nothing [m]*	Water depth [m]
DBB-JU1	417690.9	6087693.8	28
DBC-JU1	477800.5	6105924.2	28

* Coordinate reference system UTM zone 31N, WGS 84.

The spudcans on the Vole Au Vent jack-up rig used for the penetration tests have a rectangular cross-section with maximum dimensions of 13,92 x 8,96 m, and maximum bearing area A of 123,5 m². The equivalent diameter of the spudcans D_{eq} , calculated as $\sqrt{4A/\pi}$, is 12,54 m. The underside of the spudcans has a conical tip with height of 0,8 m. The overall height of the spudcans are approximately 4,2 m. Detailed spudcan drawings are presented in [Appendix A](#). The four legs of the rig are named according to their position in relation to the rig:

- PSF – Port Side Front
- PSA – Port Side Aft
- SBF – Starboard Front
- SBA – Starboard Aft

4.1.1 Jacking Procedure

The jacking procedure for both locations were similar. First all jack-up legs were lowered until touchdown and pre-loaded with 39-59 MN to allow the rig to come out of the water. In both locations the SBF and PSA legs were loaded incrementally in a conventional way with load steps of 4,9 MN (500 tonnes), where the next load step was added when the penetration rate settled. Normal procedure for Jan de Nul is to add the next load step when the penetration rate drops below 15 cm per 15 min.

Also at both locations, the PSF and SBA tests were done as fast penetrations where the legs were penetrated as fast as possible until maximum pre-load of 122,6 MN was reached. The test ended when the penetration rate settled below 15 cm per 30 min. In addition DBB-JU1 featured cyclic tests where the PSA leg was subjected to cyclic loading at 11,5 m and 12,5 m depth and the SBF leg in depths of 13,5 m and 14,5 m. The results of the cyclic tests are not considered in this thesis.

Different data logging frequencies were used at these locations. At DBB-JU1 data, e.g. penetration depth and leg force, was recorded approximately every 5th seconds, whereas at DBC-JU1 data was recorded every 55th seconds. Note that at DBC-JU1 two spudcan penetration tests were done where the second one was re-jacking in existing footprints. The first jacking in undisturbed soil is considered herein.

4.1.2 Accuracy of measurements

Regarding accuracy of the measurements [Equinor \(2020\)](#) gives information with respect to accuracy provided by Jan De Nul. Total accuracy in measured loads for one leg is estimated at 5%. The depth measurements are based on bathymetry data and GPS position, thus the accuracy is dependent on the accuracy of the bathymetry data and GPS system. Jan de Nul states that the leg depth relative to the vessel is accurate to ± 20 cm. However, zero penetration depth can be estimated by identifying for which depth the spudcan is in full contact with the sea-bottom, i.e. when the the maximum bearing area, A , is in contact with soil, and from where the penetration resistance starts to increase.

4.1.3 Presentation of Penetration Depth

When the spudcan is penetrating, the term penetration depth can be ambiguous. Penetration depth can be taken as the penetration depth of the tip of the spudcan or it can be taken as the penetration depth of the maximum cross-sectional spudcan bearing area, hereafter denoted D , i.e the depth of the spudcan above the conical tip. As mentioned above, D equal to zero can be identified from the load-penetration measurements as from which depth the resistance starts to increase significantly. Minor corrections to the measured penetration depth have been made to ensure that zero penetration depth is correctly identified, and in the following presentation of measured spudcan load-penetration response, D will be plotted as the depth coordinate.

4.2 Geotechnical Design Parameters

The geotechnical design parameters used in the back-calculations are presented in the following. To obtain geotechnical parameters for the FE-model CPT data and lab-test data documented in the geotechnical interpretation report for Dogger Bank B (NGI, 2020a) are used. The two locations considered herein are DBB-JU1 and DBC-JU1, as described in section 4.1. Soil unit classification at these locations are given in NGI (2020b) and are advised by the British Geological Survey. These soil units are consistent with the soil units described in the geotechnical interpretation report (NGI, 2020a). For further descriptions on the soil unit classification the reader is referred to NGI (2020b).

4.2.1 Location DBB-JU1

For interpretation of soil layering and strength, measurements from 5 CPTu tests are used. At the locations one CPTu measurement was carried out at each of the 4 jack-up legs in addition to one in the centre of the location. The lateral soil variability at Dogger Bank is large and the zone of influence is small for a CPT compared to a spudcan. Therefore an average corrected cone resistance, q_t , profile is used to determine soil layering and strength, which is assumed to be more representative for a spudcan. The average profile was made by calculating an average q_t from the five CPTus at each depth. Based on this average profile and the individual profiles a design profile was established. These q_t -profiles are plotted in Figure 4.1, and show that there is considerable scatter. The design q_t -profile is tabulated in Appendix B, Table B.1.

All CPTs show high q_t values in different depths which indicates sand pockets. As the sand

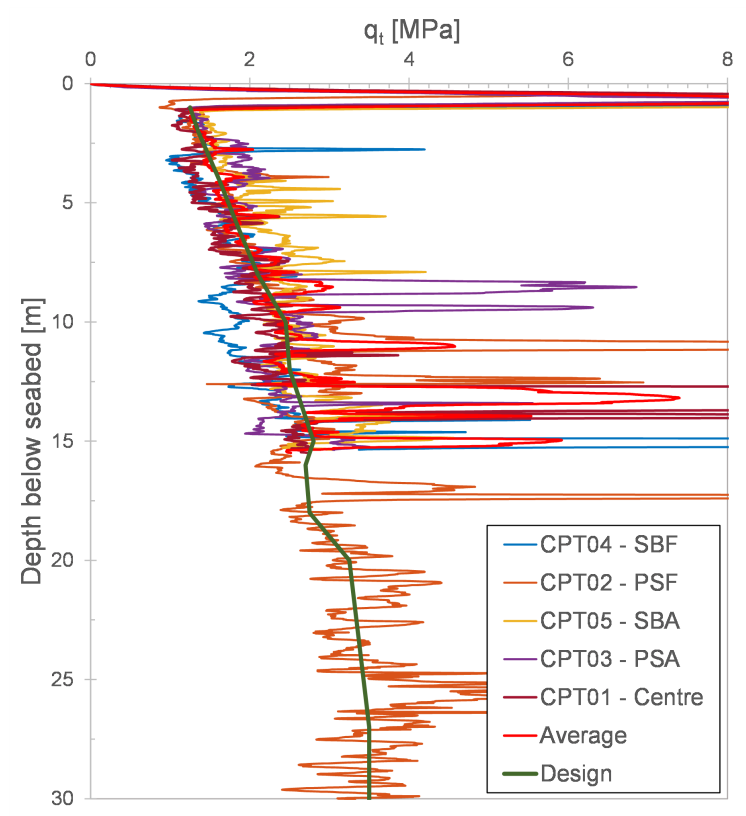


Figure 4.1: Measurements from CPTs, average q_t -profile and design q_t -profile. The legend indicates the CPT locations in relation to the jack-up legs.

pockets are located at different depths it is assumed that these pockets are only local and do not form layers. Furthermore, it is assumed that the sand pockets are small compared to the spudcan and therefore can be neglected when determining the design profile. An exception is the first meter in the soil profile where all CPTs show higher values which indicates that there is a 1 m thick surface sand layer. Below this sand layer there is assumed to be clay with increasing shear strength. The average q_t -profile includes sand pockets, but in the design profile it is aspired to omit the sands and rather to fit the design q_t -profile to CPT data in clay. The current design profile was compared to the design profile in [NGI \(2020b\)](#), which was obtained using statistical methods for filtering out sand pockets from the data, and they are in good agreement.

Note that all CPTs except the CPT from the centre of the jack-up only goes down to approximately 15 m, approximately corresponding to the depth of the spudcan tests. Therefore most emphasis was put on the first 15 m of measurements when the design q_t -profile was made. The design profile is more uncertain below 15 m, but is also less important as the spudcans only penetrated down to about 15 m. The reason that the soil profile is extending deeper than the spudcan penetration, is that in the FE-model, the soil continuum also needs to be defined

below the final spudcan penetration depth.

Undrained conditions are assumed for the clay. The undrained shear strength is obtained using the design q_t -profile and the common correlation

$$s_u = \frac{q_t - \sigma_{v0}}{N_{kt}^*} \quad (4.1)$$

where σ_{v0} is the overburden stress and N_{kt}^* is a cone factor where "*" indicates that it applies to the operational shear strength relevant for a given soil volume. In this case the volume involved in a spudcan failure. N_{kt}^* is discussed in section 2.2. For the elastic stiffness a constant rigidity index, E/s_u , is assumed. During the upcoming convergence study it is showed that the rigidity index is not important for spudcan load-penetration response, and therefore a rigidity index of 200 is used in the back-calculations. As an implication of the undrained condition Poisson's ratio ν is taken as 0,495, rendering the clay approximately incompressible.

As strain softening is considered in the back-calculation the sensitivity of the clay needs to be determined. [NGI \(2020a\)](#) has identified the larger part of the clay at DBB-JU1 to comprise of Upper Dogger Bank Clay (DBK_U_C) (from 3 m to 16,5 m below the seabed) which has an average sensitivity of 0,9 based on 101 unconsolidated undrained (UU) triaxial tests. This abnormal average S_t value of less than one indicates that the validity of S_t determined from the UU tests can be questioned. When determining S_t with a UU test, first a triaxial test is performed on an undisturbed sample with a cell pressure equal to the in-situ lateral stress and the intact strength is measured. Then, the sample is remoulded and reshaped to the desired dimensions before an additional triaxial test is carried out and the remoulded strength is determined. The sensitivity is then obtained as the ratio between the intact and remoulded strength. As the clay at Dogger Bank has distinct soil fabric with fissures, this introduces possible sources of error which can explain the abnormal S_t values from the UU tests. The reasons are, as presented in [NGI \(2020a\)](#):

1. Fissures and other weaknesses in the intact sample may cause too low measured intact s_u . When the sample is remoulded these weaknesses may be removed and will thus not affect the measurement of $s_{u,r}$.
2. When the sample is remoulded air can be trapped inside the sample. Then, during the triaxial tests this air may compress when subjected to the cell pressure and prevent the pore water from absorbing the cell pressure. This will result in a lower pore-pressure and therefore a higher effective stress in the sample, ultimately resulting in a higher measured $s_{u,r}$.

Both reasons will result in higher S_t values. Reason no. 2 was investigated by NGI by performing UU tests where the pore-pressure was measured, and concluded that increased effective stresses in the sample is a likely reason for the low sensitivity values. The sensitivity of several of the UU samples were also measured with fall cone and/or pocket penetrometer. For all cases this gave $S_t > 1$, and for the cases where UU tests gave $S_t < 1$, S_t from fall cone and pocket penetrometer gave S_t in the range from 1,2 to 2,3 (based on three cases) (NGI, 2016). It is important to bear in mind that falling cone tests involve a small area, and therefore such tests are less likely to be affected by fissures in the sample, thus falling cone tests may give too high intact strengths. Furthermore, sample disturbance may also have reduced the intact shear strength which would result in lower measured sensitivity. Thus, considering all this available information on the sensitivity of the Upper Dogger Bank clay, and accounting for the testing methods, sample disturbance, fissures and scale effects, it is difficult to conclude on a specific value for the sensitivity. As previously described in section 2.4 the sensitivity for marine clays typically range from 2 to 5, hence adopting a sensitivity larger than 1 seems reasonable. In the back-calculation several values for the sensitivity is tested to obtain a good match with the measured spudcan penetration resistance.

Another parameter important for describing the softening effect is ξ_{95} , the cumulative plastic shear strain required for 95% remoulding, which has been estimated to be around 10–25 in general. However, NGI has estimated that ξ_{95} equal to 1 is appropriate for Upper Dogger Bank Clay, based on the stress-strain curves from several triaxial tests (NGI, 2020b). Therefore ξ_{95} equal to 1 will be used in the current back-calculations. Note that NGI has considered ξ_{95} equal to 1,0 together with a sensitivity of 1,3, and it can be argued that ξ_{95} should be seen as depended on the chosen S_t . However a constant value of 1 for ξ_{95} is used during the back-calculation. Although the effect of using other ξ_{95} values are checked. Implications of this assumption are discussed in section 4.6.

The top sand layer with a thickness of 1 m can be considered thin compared to the size of the spudcan, and it is therefore assumed that the properties of this sand layer is of little importance for the spudcan load-penetration response. Therefore, little emphasis has been placed on determining exact sand parameters. The sand layer is classified as Surface deposits (SBF) and NGI (2020a) reports a best estimate for the constant volume friction angle of 33° for this unit. Since the sand will go through large deformations during the spudcan penetration, the constant volume friction angle is used as the friction angle, ϕ , in the back-analyses. For the sand elastic stiffness, E , a typical value for sand of 35 MPa is used with ν equal to 0,3. This may be a high

stiffness for a shallow sand layer, but as the sand layer is in general of less importance for the analyses considered herein, and furthermore, E is also of less importance in general for spudcan penetration, it is assumed that the elastic properties of the sand layer will have little influence on the spudcan response.

The total unit weight γ of the soil units are given in [NGI \(2020a\)](#). The sand (SBF) unit has an average γ of $19,3 \text{ kN/m}^3$ with a standard deviation of $0,9 \text{ kN/m}^3$. The clay (DBK_U_C) has an average γ of $20,1 \text{ kN/m}^3$ with a standard deviation of $1,0 \text{ kN/m}^3$. However, the initial stresses of the soil is assumed to have little influence on the load-penetration response of the spudcan, since the soil resistance is governed by the plastic failure mechanism evolving below the spudcan. As an implication of this the value of γ should not have a significant effect in the FEA. Furthermore, as spudcan penetration is a submerged process the effective unit weight γ' is used, and for the sake of simplicity γ' is taken as $9,0 \text{ kN/m}^3$ for all soil material, similar to [NGI \(2020b\)](#).

For determining the initial lateral stresses of the soil, a K'_0 of 1 is used. No direct measurements of K'_0 have been done for the Dogger Bank soil, but [NGI \(2020a\)](#) recommends low and high estimates for K'_0 based on correlations. For clay the high estimate is $K'_0 \leq 2,5$ and the low estimate is $K'_0 \leq 0,6$. However, since it is assumed that the initial stresses are of less importance for the spudcan response a constant K'_0 equal to 1 is used for all soil. In general the lateral stresses at Dogger Bank are uncertain because of the complex depositional history. Previous desiccation may have given large lateral stresses in the soil while the presence of fissures may reduce the lateral stress to zero ([NGI, 2020a](#)). Moreover, for spudcan penetration [DNV GL \(2020\)](#) investigated the effect of K'_0 and found that changing K'_0 had no effect on the spudcan penetration resistance.

Summary of geotechnical parameters for DBB-JU1

Soil layering and key geotechnical parameters are given in [Table 4.2](#). The undrained shear strength for the clay is obtained using the design q_t -profile in [Figure 4.1](#) ([Table B.1](#)) and [eq. \(4.1\)](#). The sensitivity of the clay is uncertain and S_t in the range from 1 to 6 is tested. ξ_{95} is taken as 1, and K'_0 is set equal to 1 for all back-calculations.

Table 4.2: Geotechnical parameters for location DBB-JU1 and soil layering. z_{top} and z_{bot} refer to depth to the top and bottom of the layers below the seabed.

z_{top} [m]	z_{bot} [m]	soil type	soil unit	γ' [kN/m^3]	E	ν	ϕ [°]
0,0	1,0	sand	SBF	9	35 Mpa	0,3	33
1,0	30,0	clay	DBK_U_C	9	$200 s_u$	0,495	

4.2.2 Location DBC-JU1

The back-calculations for location DBC-JU1 are less extensive and are done primarily to check that the FE-model can provide good predictions of spudcan penetration resistance at other locations than DBB-JU1. Therefore, a more simplified method for obtaining geotechnical parameters is used.

The used soil profile is taken from [NGI \(2020b\)](#). There is a top 1,2 m thick sand layer, interpreted as SBE, overlaying a 10,1 m thick clay layer belonging to the Botney Cut (BCT) clay unit. The soil below the clay comprises of sand. The bottom sand layer is interpreted to be of the Upper Dogger Bank Sand (DBK_U_S) unit. The surface sand layer is thin compared to the spudcan dimensions, and the spudcan penetrations at this location do not penetrate the bottom sand layer. Therefore it is assessed that the geotechnical sand parameters are of less importance for the spudcan back-analyses at DBC-JU1. For the undrained shear strength of the clay at DBC-JU1, the best estimate profile given in [NGI \(2020b\)](#) is used which is based on spudcan back-calculations using FE-analyses and bearing capacity formulations. This s_u -profile is tabulated in Table 4.3. Note that the soil profile presented in [NGI \(2020b\)](#) only extends down to 15 m depth, and presents CPT-data down to 20 m, whereas the soil continuum in the FE-models in this thesis extends down to 30 m depth. The CPT data presented by NGI indicated that there is sand below the BCT clay layer, i.e from 11,3 to 20 m depth. As the spudcans have a maximum penetration depth of 11,3 m the soil properties below 20 m depth should not have any significant influence on the spudcan load-penetration response, and it is assumed that the lower sand layer extends down to 30 m depth.

Table 4.3: Shear strength profile for location DBC-JU1

Depth below seabed [m]	s_u [kPa]
1.2	58.6
5.5	63.6
5.5	70.1
7.4	72.7
7.4	66.4
10.0	95.7
10.0	98.3
11.3	93.0

The sensitivity for (BCT) clay has an average value of 1,7 based on 21 UU triaxial tests. As discussed for the DBB-JU1 location the accuracy of S_t determined from UU tests may be questioned, and UU tests may in general give too low sensitives in the fissured clay present at DB. ξ_{95}

is set equal to 1 in the back-calculation, same as in [NGI \(2020b\)](#).

For the sand layer the same sand parameters are used as at DBB-JU1. I.e. ϕ is set equal to the constant volume friction angle of 33° , E is taken as 35 MPa and ν is taken as 0,3.

The average total unit weight for BCT clay is $19,6 \text{ kN/m}^3$ and for DBK_U_S $19,5 \text{ kN/m}^3$. As the initial stresses are assessed to be of less importance, as described for location DBB-JU1, an effective unit weight of 9 kN/m^3 is used in the back-calculations. Furthermore, K'_0 is taken as 1 like at DBB-JU1.

Soil layering and key geotechnical parameters for DBC-JU1 are given in [Table 4.4](#).

Table 4.4: Geotechnical parameters for location DBC-JU1 and soil layering. z_{top} and z_{bot} refer to depth to the top and bottom of the layers below the seabed.

z_{top} [m]	z_{bot} [m]	soil type	soil unit	γ' [kN/m^3]	E	ν	ϕ [$^\circ$]
0,0	1,2	sand	SBF	9	35 Mpa	0.3	33
1,2	11,3	clay	BCT	9	$200 s_u$	0.495	
11.3	30,0	sand	DBK_U_S	9	35 MPa	0.3	33

4.3 Finite Element Model

For the FE-analyses in this thesis the Coupled Eulerian-Lagrange method (CEL) is employed with Abaqus\Explicit version R2019x where the soil is modelled with Eulerian elements and the spudcan is modelled with Lagrangian elements. This allows the soil to undergo large deformations as it is pushed by the penetrating spudcan. Due to the symmetry of the spudcan a quarter of the physical problem is modelled.

The Eulerian soil is modelled as a quarter cylinder. A 5 m thick layer of void elements, i.e. elements without a material, is added on top of the soil to allow for free soil heave during the penetration. Symmetrical boundary conditions (BCs) is prescribed to the vertical planes of symmetry by prescribing zero velocity, i.e zero soil flow, perpendicular to the planes. For the outer circumferential border zero velocity was prescribed to both the horizontal directions being somewhat more strict than the more correct BC of zero radial flow. The imposition of this stricter BC is believed to have an insignificant effect on the analysis results, and is verified during the convergence study by considering the effect of soil radius. All vertical boundaries allow for free vertical soil movement. The bottom border is prescribed zero vertical velocity. An example of the soil model and mesh can be found in [Figure 4.3](#). The soil domain is meshed with 8-node linear Eulerian brick elements with reduced integration and hourglass control (EC3D8R), the only Eulerian

element type available in Abaqus R2019x.

A real spudcan is made up of plates and internal stiffeners with a complex geometry, but spudcans are designed to be used multiple times, thus a spudcan should only develop small elastic deformations during penetration. Furthermore, the stresses and strains in the spudcan is not of interest for the analyses herein. Therefore the spudcan is modelled as a solid weightless rigid body. The geometry is modelled after the geometry presented in Appendix A, and the model is displayed in Figure 4.2. The spudcan is meshed with 10-node quadratic tetrahedral elements named C3D10 in Abaqus. The element side-lengths were set to approximately 0,4 m giving a mesh density similar to the finest mesh density of the soil. This resulted in 28 732 elements for the spudcan. The mesh properties of the spudcan is believed to be of less importance as it is modelled as a rigid body, and therefore further verification of the spudcan mesh is not carried out. The spudcan is initially and during the application of the gravity load fixed inn all degrees of freedom. During penetration, only the prescribed vertical movement is allowed.

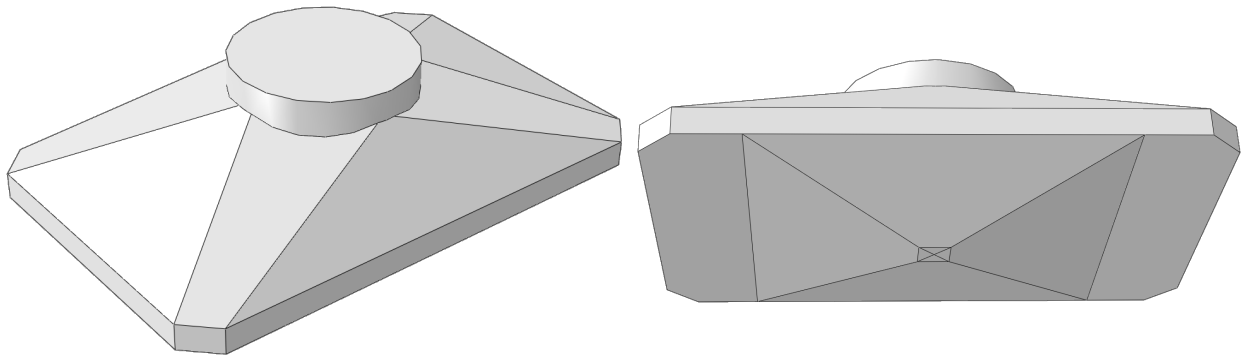


Figure 4.2: The Spudcan model used in the FE-analyses seen from top and bottom.

As the Lagrangian spudcan is penetrating into the Eulerian soil the volume of the spudcan displaces the soil-material in the Eulerian mesh, and the volume occupied by the spudcan in the Eulerian mesh is replaced by void. These contact constraints are enforced by the "general contact" algorithm available in Abaqus as described in section 2.6.1. This algorithm ensures that there is no soil flow into the volume occupied by the spudcan. For the tangential behaviour of the soil-spudcan interaction a friction formulation is used, where the tangential shear stress capacity is controlled by a friction coefficient μ and a shear stress limit τ_{\max} . When this shear stress limit is reached, the soil can slide along the spudcan. By modifying μ and τ_{\max} the soil-spudcan interaction can be modelled as smooth where the soil and spudcan are free to slide against each other, rough where the soil and spudcan are not allowed to slide against each other, or something in between by prescribing a shear stress limit. It is not possible to change interac-

tion properties with soil depth, therefore the interaction properties can not be made dependent on e.g. soil strength. Thus constant interaction properties must be defined for the analysis.

The FE-analysis consists of three steps. In the initial step the model is established with given materials and boundary conditions. In the next step a gravity load is introduced together with a geostatic stress field ensuring equilibrium with the gravity load. Furthermore, the geostatic field is prescribing initial vertical and horizontal stresses given by the user. In this case the at rest lateral earth pressure coefficient, K'_0 is set equal to 1 as discussed in section 4.2.1. The duration of this step is set to one second, and the gravitational acceleration is set to 10 m/s^2 . The last step is the penetration step where the spudcan is prescribed a constant vertical velocity. The duration of this step is modified to give the desired penetration depth dependent on the penetration velocity. During this step the penetration depth and resistance is measured to obtain the load-penetration response.

In the following presentation of load-penetration response curves the data has been filtered using the Butterworth filter to obtain smoother curves with less noise which are easier to interpret. The Butterworth filter is discussed in Section 2.6.4 and applied directly in Abaqus\CAE. The cut-off frequency is adjusted to minimise noise while still giving a good fit to the trend of the data. The default filter order in Abaqus of two is used. If not otherwise mentioned the cut-off frequency is set to 1 Hz in the following load-penetration curves. As noise is filtered out of the data, the level of noise in the different load-penetration curves should not be directly compared. A comparison of filtered and unfiltered data can be found in Appendix C Figure C.1.

4.4 Convergence Study

To find FE-model parameters that give reliable results a convergence study is carried out where the effect of the following parameters are investigated:

- Radius of soil domain
- Mesh density
- Soil-spudcan interaction
- Height of soil domain
- Penetration velocity
- Rigidity index

The goal of the study is to show that the model is converging to the correct solution and to establish the sensitivity to changes in the given parameters. During the study 16 analyses were carried out where one parameter was changed at the time, to verify if the model is converging. Note that in the following presentation of load-penetration response curves from the conver-

gence study the curves with an orange colour is corresponding to the same base-case analysis.

The soil profile used in the convergence study corresponds to location DBB-JU1, and geotechnical parameters for this location are described in section 4.2.1. The s_u -profile was obtained using a N_{kt}^* equal to 21 with the design q_t -profile (fig. 4.1) and eq. (4.1). However, note that due to minor adjustments in the design q_t -profile done after the convergence study, and because of a mistake done in the calculation of s_u from q_t , the shear strength used for the convergence study is up to 20 % larger than the correct value. The specific s_u profile used for the convergence study is given in Table B.2. The specific s_u -profile used in the convergence study is of less importance for results of the convergence study, thus the conclusions from this study are not affected by this discrepancy. In the convergence study the clay is modelled as elastic-perfectly plastic with the Tresca yield criterion. The constitutive behaviour of the sand is modelled as elastic with Mohr–Coulomb plasticity. Hence, no rate or softening effects are included in the convergence study.

First the **mesh density** was investigated by considering the four meshes given in Table 4.5. The meshes has the highest density in the centre of the soil domain and a linear increase in element side length in the radial direction. The vertical side length is kept constant and equal to the smallest horizontal side length except for the bottom 8,7 m. Here the vertical element side length is set equal to the largest element length in the horizontal direction. 8,7 m was chosen to ensure that the plastic deformation takes place in the more refined region. The purpose of this meshing strategy is to ensure adequate mesh refinement in the regions of large deformation while limiting the number of elements in the model to preserve computational time. The FE-model discretised with Mesh2 is shown in Figure 4.3. Note that the spudcan tip is located at the top of the soil surface, and that the Eulerian mesh around and above the spudcan consists of void elements.

Table 4.5: Meshes considered for the soil domain in the convergence study.

Name	No. of elements*	Approx. smallest side length [m]	Approx. largest side length [m]
Mesh1	51 204	0.6	1.2
Mesh2	124 108	0.4	1.0
Mesh3	271 920	0.3	0.8
Mesh4	728 679	0.2	0.6

* The no. of elements in this table applies to a mesh with radius and height of the soil domain equal to 30 m.

For the mesh density convergence study a soil radius, R , equal to 30 m, soil height, H , equal

to 30 m and a penetration velocity of 1 m/s is chosen. For the soil-spudcan interaction a shear stress limit of 50 kPa is used together with a very high friction coefficient giving a practically instantaneous shear stress capacity equal to shear stress limit on the soil-spudcan interface. These parameters are chosen based on preliminary FE-analyses, and is verified in the following parts of the convergence study.

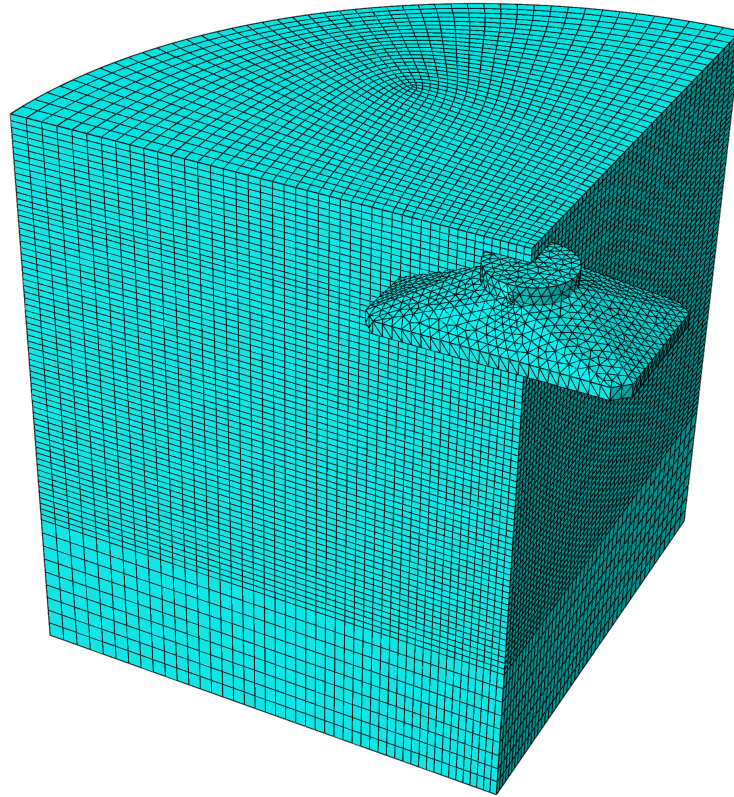


Figure 4.3: FE-model with spudcan and soil domain discretised with Mesh2.

The results of the mesh convergence study is presented in Figure 4.4(a). The calculation time was 19 minutes for the coarsest mesh and 20 hours for the finest mesh. From the figure it is seen that increased mesh density gives less resistance, and that the mesh refinement is not great enough for the solution to converge. At 15 m the relative difference between resistance from mesh 1 and 2 is 5,7 %, between mesh 2 and 3 is 5,8 % and between mesh 3 and 4 is 3,5 %. Thus the relative difference is decreasing and can indicate that the solution is approaching convergence. As a compromise between computational time and accuracy Mesh3 can be used in further back analyses, but the resistance will then be overestimated by 3,5 % or more. The response from Mesh 1 is more erratic than the response from the other meshes, and the response from the three finest meshes are parallel, thus increased mesh refinement gives a more stable and smooth solution. For the further convergence study Mesh2 is used.

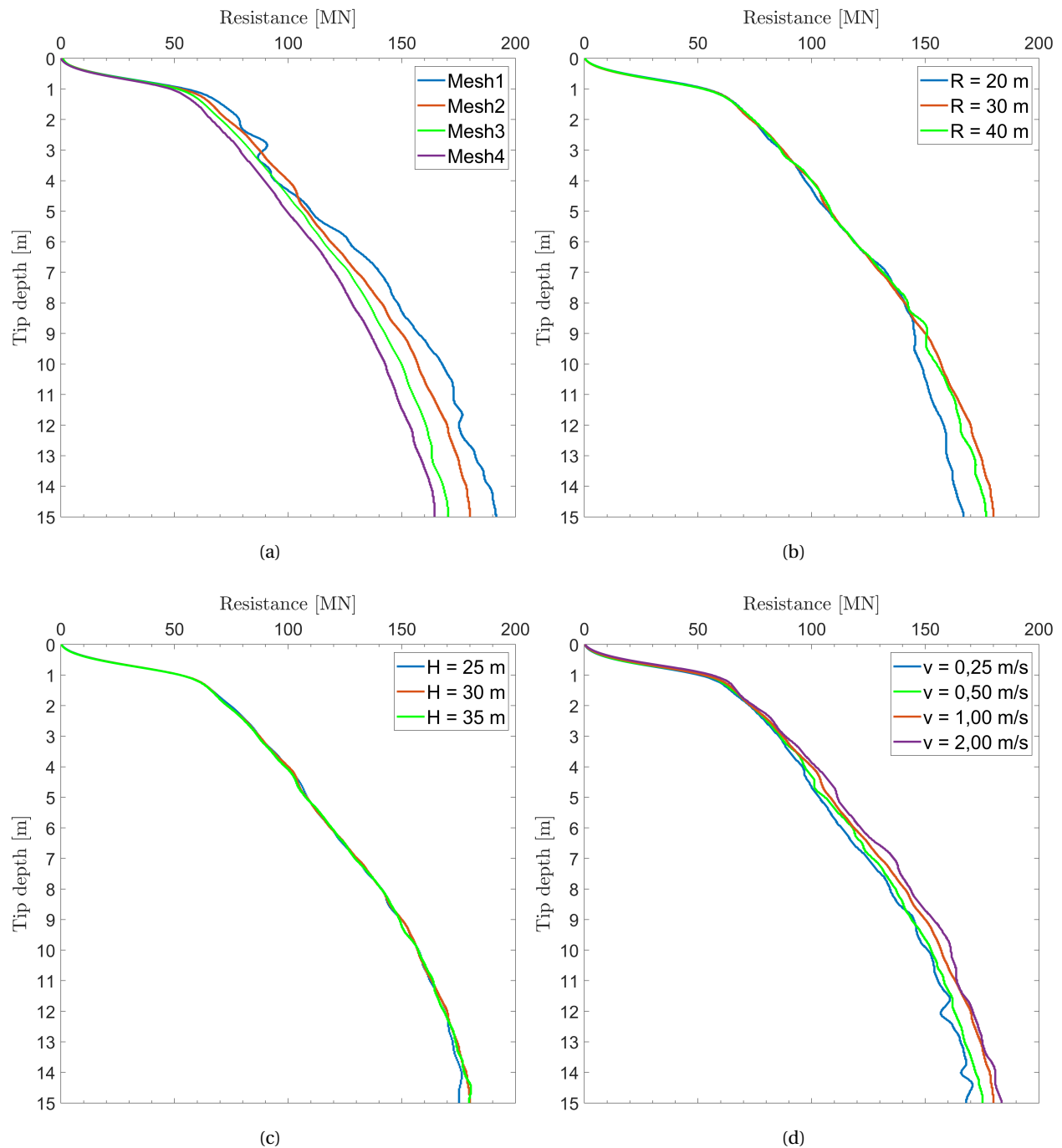


Figure 4.4: Load-penetration response from convergence study. (a)-(d) shows the effects of mesh density, radius of soil domain (R), height of soil domain (H) and penetration velocity (v), respectively. Tip depth is referring to the penetration depth of the spudcan tip.

For soil **radius** three different radii are considered, 20 m, 30 m and 40 m. The mesh density is kept similar to the mesh density of Mesh2, by shrinking or extending the mesh size while keeping the same gradual increase of element side length towards the circumferential border. The other FE-model parameters are identical to parameters used in the mesh density checks. The result

of the convergence study of soil radius are shown in Figure 4.4(b). In general the response from the models with a soil radius of 30 m and 40 m are very similar, indicating that the solution has converged for a radius of 30 m.

By introducing the circumferential BC two sources of error is introduced. The soil is free to move vertically, but restricted horizontally, whereas in reality the soil has some freedom to move horizontally and is not fully free to move vertically. The horizontal BC will therefore give a higher resistance while the vertical BC gives less resistance for the spudcan load-penetration response. It is not evident what is the dominating effect and the internal relationship between these effects may explain why a soil radius of 30 m gives a slightly higher resistance than a radius of 40 m. From 8,5 m of penetration and down the curve corresponding to a radius of 20 m diverge from the two other curves. This is due to a change in deformation mode in the model. The clay is modelled as incompressible, and thus the clay volume displaced by the spudcan must lead to an expansion of the soil volume somewhere else in the model. Initially this expansion takes the form of a ridge around the cavity, but at approximately 8,5 m of penetration the ridge height becomes constant for the model with a radius of 20 m, and the entire soil domain starts to heave. This behaviour is unrealistic and is demonstrating that the BC of free vertical movement at the circumferential border may give to low resistance. Furthermore, this unrealistic behaviour does not occur in the models with a radius of 30 or 40 meter. A radius of 30 m will be used for further back-calculations.

For the convergence study on the **height** of the soil domain three heights are considered, 25 m, 30 m and 35 m. For these analyses Mesh2 was used where the coarser bottom region was lengthened or shortened to obtain the desired height. Otherwise the same FE-model parameters were used as in the above analyses. Note that an additional 5 m thick layer of void elements above the soil is present in all analyses. The resulting load-penetration response is shown in Figure 4.4(c). The response from soil domains with heights of 30 m and 35 m are practically identical indicating that the solution has converged for H equal to 30 m. The resistance from the model with H equal to 25 m is slightly less at the deepest penetration than for H equal to 30 m and 35 m, thus H equal to 20 m is considered to be too low. Furthermore, an additional analysis was conducted where the bottom part of the mesh was refined, but this did not affect the load-penetration response. A soil domain height of 30 m will be used for further back-analyses.

The effect of spudcan **penetration velocity** was investigated by considering four different penetration velocities of 0,25 m/s, 0,50 m/s, 1,00 m/s and 2,00 m/s. Mesh2 was used with the same FE-model parameters as previously used in the convergence study. The resulting load-

penetration response is shown in Figure 4.4(d), and there is a clear trend of decreasing resistance with decreasing penetration velocity. The considered penetration velocities are much larger than in real spudcan penetration, but as the computational time is proportional with the inverse of penetration velocity, modelling the real penetration rate would require an impractical large computational time. However, real spudcan penetration is essentially quasi-static in nature, and when using a dynamic explicit solution, too large penetration rates may give rise to unrealistic dynamic effects, e.g. inertia forces. Therefore the modelled penetration rate must be sufficiently low to avoid such effects. For the convergence study on penetration velocity the cut-off frequency used for the Butterworth filter was modified in the post-processing of results since the penetration velocity indirectly influences the sampling frequency of the data, thus changing the appropriate cut-off frequency. Chosen cut-off frequencies were in the range from 0.3 Hz to 2 Hz and verified to match the unfiltered response.

Ideally the convergence study should show identical load-penetration response for the lowest penetration rates. However, this is not the case in Figure 4.4(d), and it is uncertain if the solution has converged. Although the curves corresponding to penetration velocities of 0,25 m/s and 0.5 m/s match quite well above 11,6 m depth they start to diverge below this depth. On the other hand it is not very clear how large the difference is since the curve corresponding to a velocity of 0,25 m/s is more erratic than the others. The relative difference for the deepest part is in the range of 1,0 to 4,5 % for penetration velocities of 0,25 m/s and 0,5 m/s. At 15 m depth the relative difference between the curves corresponding to velocities of 1 m/s and 0,5 m/s is 2,8 %. As a compromise between solution accuracy and computational time a penetration velocity of 1,0 m/s is used in the further spudcan back-analyses. Thus an overshoot in resistance of approximately 3 to 4,5 percent or more can be expected.

The effect of **soil-spudcan interaction** properties has been investigated by considering four different interaction properties by modifying the friction coefficient μ and the shear stress limit τ_{\max} :

1. Smooth: No friction between the soil and spudcan.
2. Shear stress limit: $\tau_{\max} = 50 \text{ kPa}$
3. Shear stress limit: $\tau_{\max} = 100 \text{ kPa}$
4. Rough: Full friction between spudcan and soil. τ_{\max} is set equal to $2s_u^{max}$ where s_u^{max} is the maximum undrained shear strength in the soil profile. Thus the soil will not slide along the

spudcan, but rather the soil will fail at a distance away from the spudcan.

The resulting load-penetration response from the convergence study of soil-spudcan interaction is shown in Figure 4.5(a). The curve corresponding to a smooth interaction gives the lowest resistance while the curve corresponding to a rough interaction gives the largest resistance. The relative difference at 15 m depth is 5.3 %, thus the difference between these two opposite interaction properties is not large. Furthermore, the two curves corresponding to τ_{\max} equal to 50 kPa and equal to 100 kPa are practically identical for most of the penetration. In reality the soil-spudcan interaction is neither fully smooth nor fully rough, but something in between with a gradually increasing shear stress limit with depth. However it is not possible to implement a gradually increasing shear stress limit with depth in Abaqus, so modelling the interaction with a constant τ_{\max} seems like the most correct approach. To give the most correct interaction between the soil and spudcan a τ_{\max} set to the average s_u from the top of the clay layer down to the maximum penetration depth can be used. Furthermore, since the model is not very sensitive to the value of τ_{\max} it seems reasonable to assume that this approach will not influence the load-penetration response to any large degree.

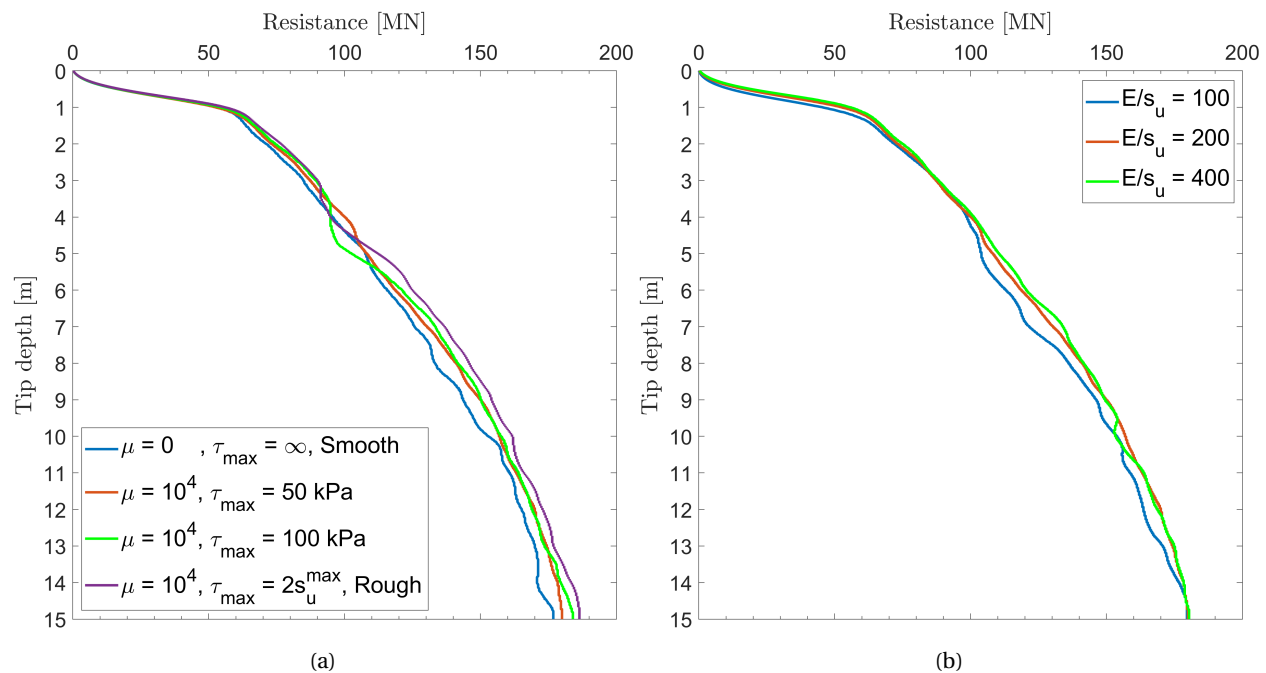


Figure 4.5: Load-penetration response from convergence study. (a) The effect of soil-spudcan interaction and (b) the effect of the rigidity index.

The effect of the **rigidity index** have been investigated by considering three different values of the rigidity index, 100, 200 and 400, and the resulting load-penetration response is shown in

Figure 4.5(b). The figure shows that the load-penetration responses are almost identical, but the curve corresponding to a rigidity index of 100 is showing slightly less resistance. The rigidity index is an inherent property of a clay and can vary between 100 and 1000 (Tho et al., 2012). Thus the rigidity index value of 100 can be considered as very low, and the corresponding low elastic stiffness may explain the reduced resistance. However increasing the rigidity index from 200 to 400 seems to have a very little to no effect on the load-penetration response. DNV GL (2020) and Tho et al. (2012) have also investigated the effect of the rigidity index on spudcan load-penetration response, and found that E/s_u has no significant effect on the load-penetration response. Based on the findings of these analyses it seems appropriate to set the rigidity index equal to 200 in the further spudcan-penetration analyses such that a good accuracy is obtained whilst keeping the computational time as low as possible. As previously described, increasing the rigidity index also increases the computational time.

Conclusion to the Convergence Study

The convergence study of mesh density was not able to show convergence of the solution for the finest meshes, but found that the relative difference was decreasing for increasing mesh density. It is concluded that Mesh3 can be used in further back-analyses but will probably then overestimate the resistance with 3,5 % or more. It is found that a radius of 30 m and height of 30 m for the soil domain is sufficiently large for the model to converge.

The effect of penetration velocity is less clear, but a trend of decreasing penetration resistance with decreasing penetration velocity is observed. Convergence for penetration velocity was not obtained, but as a compromise between solution accuracy and computational time it is concluded that a penetration velocity of 1 m/s can be used in further back-calculation. Then the soil resistance may be overestimated with 3 % or more.

By investigating the effect of spudcan-soil interaction it is found that the interaction properties do not have a large impact on the load-penetration response, and that the response is little influenced by the shear stress limit. The conclusion is that prescribing shear stress limit equal to the average undrained shear strength from the top of the clay layer down to the maximum penetration depth will yield the most correct response.

The convergence study of the rigidity index (E/s_u) showed that E/s_u does not have a significant effect on the load-penetration response. A rigidity index of 200 was found to be appropriate ensuring good solution accuracy whilst keeping the computational time low.

Adding together the overestimation of penetration resistance from the mesh density and penetration velocity, this FE-model with the recommended model parameters can be expected to give an overshoot in resistance in the order of 6-7 % or more.

4.5 Spudcan Back-Calculation

In the following back-calculations for spudcan penetration tests at DBB-JU1 is presented, and the effects of softening and penetration rate are investigated. Furthermore, a back-calculation of spudcan penetration at DBC-JU1 is undertaken to verify that the presented approach is valid for other locations. The main purpose of these back-calculations is to calibrate rate effect parameters after spudcan penetration tests such that these rate parameters can be used to study rate effects for the lateral capacity of monopiles.

To account for softening and rate effects, the UWA-soil model, as described in section 2.4.1, is used to model the clay constitutive behaviour and implemented with VUMAT in Abaqus\Explicit. As verified in Chapter 3, the implementation of the UWA-model together with the CEL approach in Abaqus is working well. The sand is modelled with the Mohr-Coulomb material model available in [Abaqus \(2019\)](#).

For the back-calculation, the FE-model developed during the convergence study is used. The resulting FE-model parameters are then a soil domain radius and height both equal to 30 m and a model penetration velocity of 1 m/s. For all back-calculations Mesh3 (table 4.5) is used, and for the spudcan-soil interaction the shear stress limit, τ_{\max} , is set equal to the average remoulded s_u from the top of the clay and down to 15 m, i.e. $\overline{s_u}/S_t$. τ_{\max} is set equal to the remoulded strength since the soil flowing around the spudcan will be close to fully remoulded. The friction coefficient, μ is set to 10^4 such that the interaction is controlled by τ_{\max} . Geotechnical input parameters are given in Table 4.2 and section 4.2.1.

To model different spudcan penetration velocities the approach described in section 2.4.2 is used. The normalised penetration velocity, v_n is calculated as

$$v_n = \frac{v}{\dot{\gamma}_{\text{ref}} D_{\text{eq}}}$$

Where v is the spudcan penetration rate, $\dot{\gamma}_{\text{ref}}$ is the reference shear strain rate, taken as 3 %/hr and D_{eq} is the equivalent diameter of the spudcan, in this case equal to 12,5 m. v_n is then calculated using the real penetration rate and real $\dot{\gamma}_{\text{ref}}$, and kept constant in the corresponding

FEA where the modelled penetration velocity is set to 1 m/s and $\dot{\gamma}_{\text{ref}}$ is modified to model the true penetration velocity.

4.5.1 Approach

Doing spudcan back-calculations which also accounts for strain softening introduces some challenges as the strength and softening properties for Dogger Bank clay are uncertain and can be considered as unknowns. Hence, in the back-calculations N_{kt}^* , S_t and ξ_{95} needs to be calibrated such that the load-penetration response in the FE-analysis matches the measured response. However, changing these parameters will have a similar effect on the penetration resistance, and the same response can be obtained for different combinations of N_{kt}^* , S_t and ξ_{95} . It is therefore difficult to assess what the correct value of each single parameter is. The following approach is used in the current back-calculations. To obtain a reference shear strength profile the best estimate N_{kt}^* equal to 23, which is based on FEA, reported in [NGI \(2020b\)](#) is used. Next, different values of S_t are tested to obtain a good match with the slow spudcan penetration tests. Thereafter different values for the rate effect parameters, i.e. η , β and $f_{\text{rate}}^{\text{max}}$, is tested to obtain a good match with the fast penetration test.

After this process best estimate parameters for soil strength, softening and rate effects giving good agreement between the FEA and measured response is obtained. In the last phase a sensitivity study is undertaken where these parameters are varied and the response is compared to the response using the best estimate parameters.

4.5.2 Results of Back-Calculations

In the following the results from the spudcan back-calculations at DBB-JU1 is presented. Figure 4.6(a) is showing measured spudcan load-penetration response from DBB-JU1 together with the results from FE-analyses. The measurements feature slow penetration tests, i.e SBF and PSA leg, and fast penetration tests, i.e. the PSF and SBA leg. All measurements show a maximum resistance of approximately 122,6 MN, corresponding to the maximum pre-load of the jack-up rig. A clear rate effect is observed with an increase in the order of 30-40 % in resistance from the slow to the fast penetration test. The FEA-curves show results for two different penetration rates, corresponding to the fast and slow tests. Figure 4.6(b) displays measured penetration rates from the spudcan tests, and the figure shows that the slow tests had penetration rates around 0,3 mm/s, while the penetration rate for the fast tests vary but have rates around 12 mm/s during

the fast loading steps. During the initial penetration down to 2-3 m, probably corresponding to the lifting of the jack-up out of the water, the penetration rate for all legs are higher.

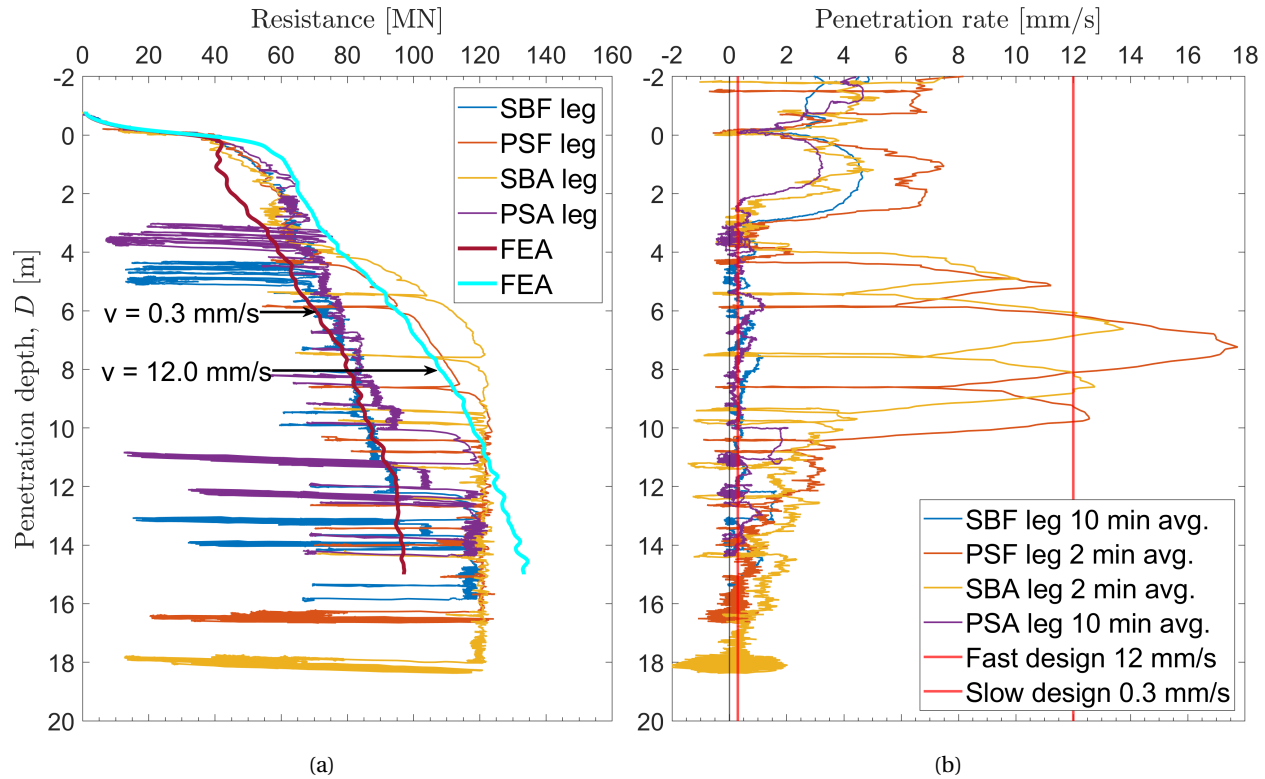


Figure 4.6: (a) is showing measured spudcan load-penetration response at DBB-JU1 together with load-penetration response from FE-analyses for two different penetration rates. (b) is showing the measured penetration rate during the spudcan tests. D is referring to the depth of maximum spudcan bearing area.

The penetration rate was calculated as $\Delta D/\Delta t$ for each data logging timepoint. To reduce noise in the data a moving average was used on the calculated rates. The moving average reduces the peak rates in the data, and it was therefore necessary to use different time spans for the moving average for the slow and fast tests to capture the peaks of the fast penetrations. Thus, an average over 10 minutes for the slow tests and an average over 2 minutes for the fast tests is used. From the plot of penetration rates it is evident that the adopted jacking procedure for the fast tests was not able to maintain a constant penetration rate, but fast penetration rates were obtained during selected loading steps. In the FEA it is not possible to model a changing penetration rate with the adopted approach for modelling of penetration rate. Inspection of the raw data showed that the PSA leg had an average penetration rate of 12 mm/s during the fast load steps, and the PSF leg had an average rate of 16 mm/s during the load step corresponding to the peak up to about 18 mm/s in Figure 4.6(b). Based on this a constant penetration rate of 12 mm/s was selected for the back calculation of the fast penetration tests. For FE-analyses of slow

penetration tests a rate of 0,3 mm/s is chosen as this rate gives a good fit to the measured rate in the slow tests.

For the FEA curves shown in Figure 4.6(a), an N_{kt}^* of 23 is used as previously described together with the design q_t -profile. For the softening a sensitivity of 4 and ξ_{95} of 1 is used. For the rate effect η equal to 0,5, β equal to 0,4, and f_{rate}^{max} equal to 6 is adopted. These parameters were found to give a reasonably good agreement with the measurements, as can be seen from the figure. The choice of parameters will be elaborated in the discussion to follow, and in the following these rate and softening parameters are denoted as the *base case parameters*. The FEA-curve with a penetration rate of 0,3 mm/s gives resistance similar to the slow penetration tests during the penetration depths with a comparable penetration rate, but the curve for the PSA leg shows slightly higher resistance. Considering the FEA-curve with a penetration rate of 12 mm/s and the fast penetration tests during the fast loading steps, they show similar resistance. The FEA-curve seems to match the PSF leg best, while the SBA leg shows a higher resistance. In general the chosen rate parameters seem to give a similar rate effect as measured in the field.

Sensitivity Study

A sensitivity study was carried out to see how rate and softening parameters and the N_{kt}^* factor influence the load-penetration response. For the rate effect two sets of rate parameters are considered together with an analysis with no rate effects, i.e. with η equal to zero. The corresponding load-penetration curves are shown in Figure 4.7(a). S_t and ξ_{95} are set equal to 4 and 1, respectively, which corresponds to the base case softening parameters, for all analyses presented in the figure. Figure 4.7(b) is showing plots of f_{rate} from the UWA-model for two different sets of rate parameters. The dotted curve with $f_{rate}^{max} = 1,45$, $\eta = 3,0$ and $\beta = 0,052$ is fitted to the NGI rate equation (eq. 2.3) for $f_{rate} \geq 1$ meaning that the part of the NGI rate equation for $f_{rate} < 1$ is not considered as $f_{rate} \geq 1$ in the UWA-model (eq. 2.4). Dotted load-penetration curves corresponding to the NGI-rate equation are shown in Figure 4.7(a) for penetration rates of 0,3 and 12 mm/s, and it is evident that the rate effect is small when using the rate parameters fitted to the NGI rate equation, although this equation is based on empirical measurements. Both the curves with a penetration rate of 0,3 and 12,0 mm/s using parameters fitted to the NGI rate equation have resistance similar to the curve without rate effects.

To obtain a rate effect matching the observed rate effect from the field a different set of parameters is proposed with $f_{rate}^{max} = 6,0$, $\eta = 0,5$ and $\beta = 0,4$ shown as the solid curve in Figure 4.7(b),

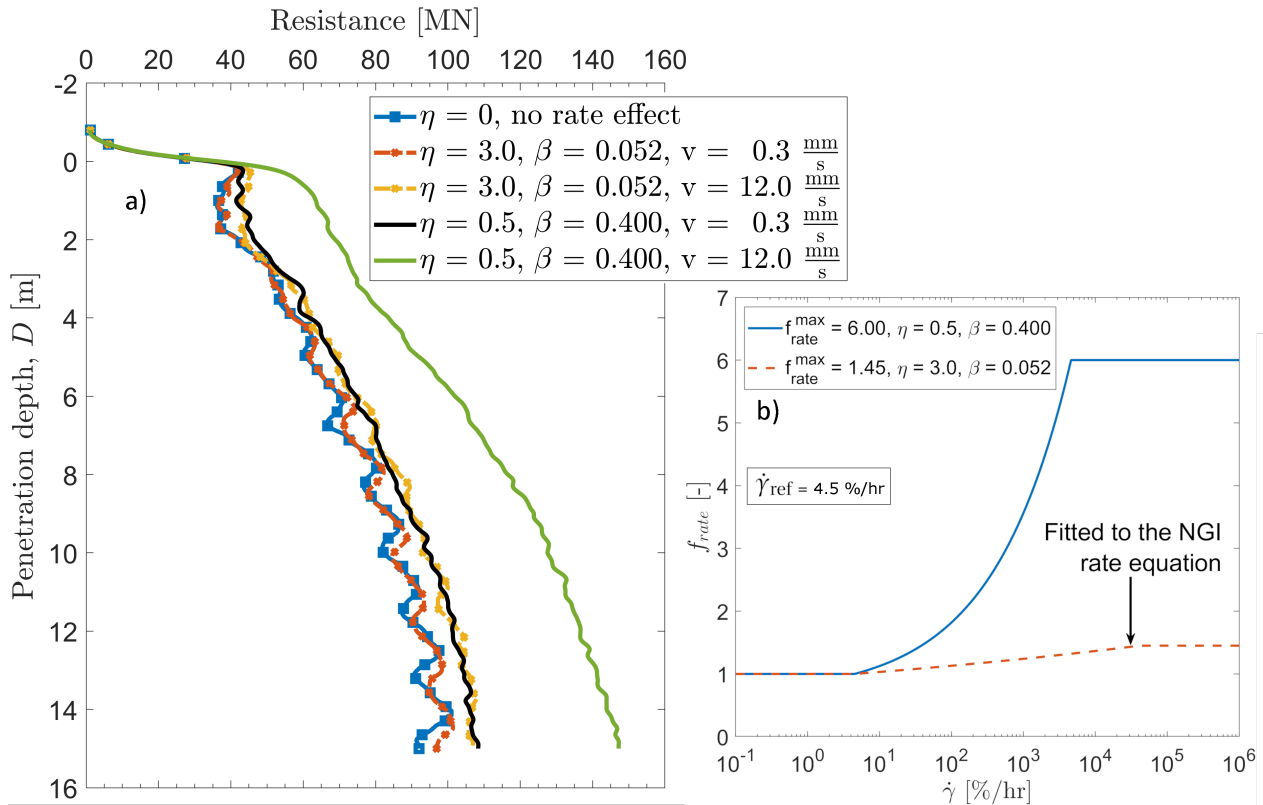


Figure 4.7: a) is showing load-penetration response from FEA using different rate effect parameters for two different penetration rates. b) is showing f_{rate} versus $\dot{\gamma}_{\text{ref}}$ for two sets of rate effect parameters.

and corresponding to the base case rate parameters. It is evident that these parameters give a much larger rate effect than the empirical based NGI rate equation. The corresponding load-penetration curves for rates of 0,3 and 12,0 mm/s are shown in Figure 4.7(a) and plotted as solid lines, and these curves show a rate effect similar to what is observed in the spudcan field tests. Note that the curves in Figure 4.7(b) are plotted for $\dot{\gamma}_{\text{ref}} = 4,5$ %/hr, while $\dot{\gamma}_{\text{ref}}$ is taken as 3 %/hr in all back-calculations.

Due to an error in the calculation of s_u from the design q_t -profile during the early stages of this study, the s_u -profile used for the analyses in Figure 4.7(a) is not consistent with an N_{kt}^* equal to 23 and the design q_t -profile. Although an incorrect s_u -profile is used in these analyses the comparison of rate effects in the figure is still valid. The adopted s_u profile is tabulated together with the correct profile in Table B.3. The same error applies to Figure 4.8(a), but the conclusions that can be drawn from the figure on the effect of S_t and ξ_{95} are not affected by this error.

To explore the effect of the softening parameters S_t and ξ_{95} , FE-analyses where these parameters are varied was undertaken, and the resulting load-penetration curves are shown in Figure 4.8(a). ξ_{95} is the cumulative plastic shear strain required for 95% remoulding. For these

analyses the base case rate parameters is used with a penetration rate of 0,3 mm/s. Note that the black curve in Figure 4.7(a) and Figure 4.8(a) corresponds to the same analysis using the base case parameters.

In general Figure 4.8(a) shows that the softening parameters have a significant effect on the resistance. Using a higher sensitivity of 6 or a lower ξ_{95} of 0,1 reduces the resistance compared to the base case parameters. Similarly, using a low S_t of 2,8 or a high ξ_{95} gives a higher resistance. Varying ξ_{95} has a significant effect on the resistance. Using ξ_{95} equal to 0,1, which means that the soil is fully remoulded after 10 % shear strain corresponding to a very brittle soil, yields a very low resistance compared to the base case parameters. On the opposite side, using ξ_{95} equal to 10, corresponding to a more ductile soil, gives much higher resistance as the soil will soften much less during the penetration.

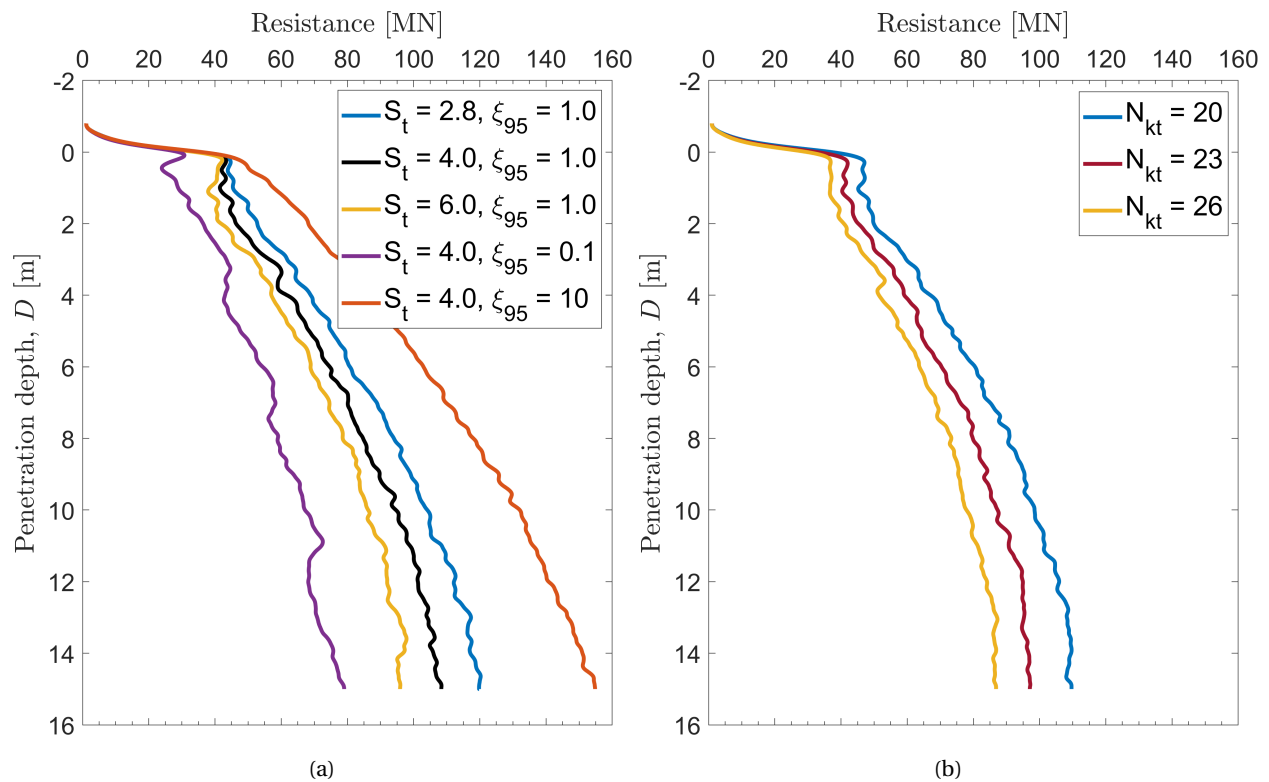


Figure 4.8: Load-penetration response from FEA showing the effect of (a) S_t and ξ_{95} and (b) the effect of N_{kt} .

The effect of changing the reference shear strength, s_u , is investigated by varying N_{kt} , and the resulting load-penetration response is shown in Figure 4.8(b). For the FEA corresponding to the plot, the base case softening and rate parameters are used with the design q_t -profile. Note that the red curve in this plot is the same as the red curve in Figure 4.6(a), and that the black and red curves are comparable as they are using the base case softening and rate effect parameters,

although they are based on slightly different s_u -profiles. As expected lowering the N_{kt} factor increases the resistance and vice versa. A key observation from Figure 4.8 is that changing one of the parameters, i.e S_t , ξ_{95} or N_{kt} , can have the same effect as changing another parameter. Therefore, the same response can be obtained for different combinations of the parameters. Hence, it is challenging to assess what the correct value of these parameters are if the correct value is not given by other information.

Failure Mechanism and Contour Plots

To gain more insight into the performance of the FE-model, contour plots displaying deformed shape, stresses, strains, velocity vectors and softening and rate effects in the soil are presented in the following. The displayed plots are from the two FE-analyses shown in Figure 4.6(a) using the base case softening and rate parameters, and the plots show the spudcan at 13 m tip penetration depth.

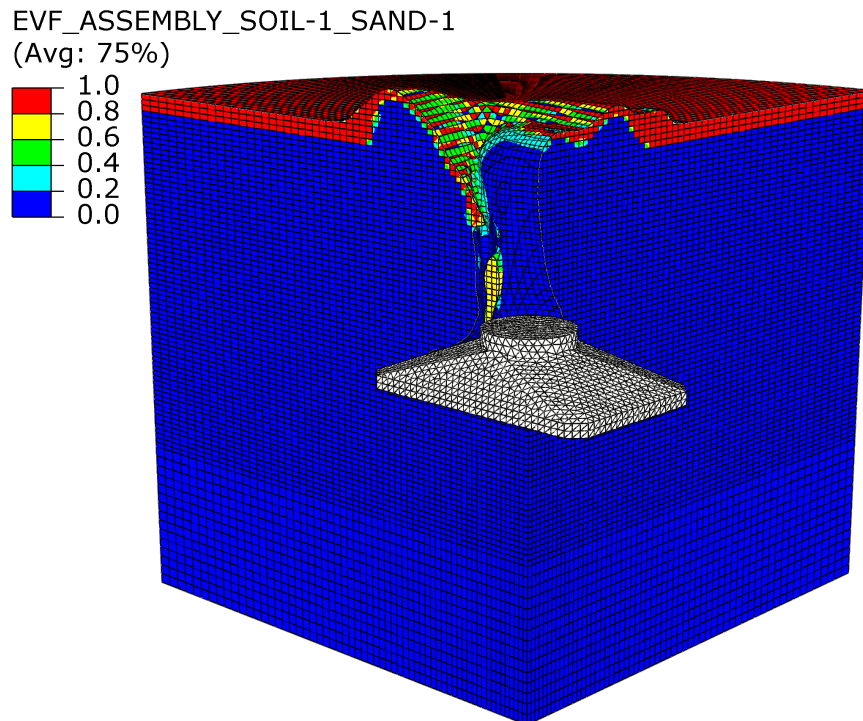


Figure 4.9: Deformed spudcan penetration FE-model at penetration depth D equal to 12,2 m for penetration rate of 0,3 mm/s. Contours of EVF sand.

Figure 4.9 is showing the deformed shape of the model with contours of Eulerian volume fraction (EVF) of sand. The penetration rate of the spudcan is here 0,3 mm/s. An EVF-sand value of 1 means that the respective element is 100% filled with sand and a value of e.g 0,5 means that it is 50% filled etc. EVF is described in section 2.6.1. The blue elements below the sand with EVF-sand of 0 are filled with clay. Thus, the figure shows that the sand remains at the surface with some sand falling into the cavity. During the penetration there is only a little sand below the spudcan which is quickly pushed out to the sides in the early stages of the penetration. This observation supports the assumption that the sand is of little importance for these analyses. The figure also shows that the Eulerian soil is flowing up into the initially void layer to form ridge around the cavity, confirming that the Coupled Eulerian-Lagrangian (CEL) formulation is

working as expected. It is also seen that there is backflow coming onto the top of the spudcan.

Figure 4.10 is showing contours of Tresca stresses and cumulative plastic shear strain, ξ . The plot of stresses shows that the soil strength is mobilised much deeper down than the penetration depth of the spudcan. Comparing with the plot of ξ , the plastic strains are, on the other hand, localised around the spudcan. From the stresses the formation of a slightly localised shear band with lower stresses can also be seen as the green band right below the spudcan.

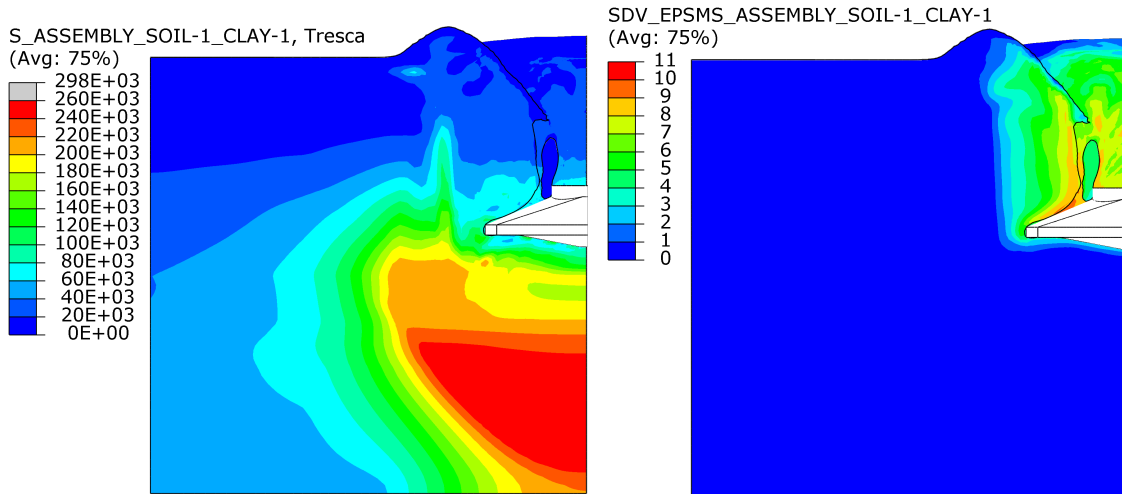


Figure 4.10: Deformed spudcan penetration FE-model at penetration depth D equal to 12,2 m for a penetration rate of 0,3 mm/s. Contours are showing Tresca stresses $[\sigma_1 - \sigma_3]$ in Pa (left) and cumulative plastic shear strain, ξ (right).

In Figure 4.11 contour plots of f_{soft} and f_{rate} are shown for a penetration rate of 0,3 mm/s and 12,0 mm/s. These parameters show how the softening and rate effect is distributed inside the soil and are described in section 2.4.1. The plots of f_{soft} show that the soil above and the soil which is flowing around the spudcan is fully remoulded with f_{soft} equal to $1/S_t$, which in this case is 0,25. The plots of f_{rate} show that there is significantly more rate effect in the analysis with a penetration rate of 12 mm/s compared to 0,3 mm/s. For a rate of 12 mm/s much of the soil flowing around the spudcan gains strength due to the rate effect, and much of the soil shows f_{rate} equal to $f_{\text{rate}}^{\text{max}}$ [= 6]. Whereas for a rate of 0,3 mm/s f_{rate} is around 3 in a smaller region. The distribution of the rate effect in the soil is erratic, similar to what was observed for the FE-modelling of a triaxial test (see Figure 3.6). The reason for this erratic rate effect distribution is discussed in section 3.2.

Comparing f_{soft} for the two penetration rates, it is evident that for a penetration rate of 12 mm/s, the softening zone is wider than for a penetration rate of 0,3 mm/s. The plots showing softening also show the formation of a shear band, where the softening is localising in a band

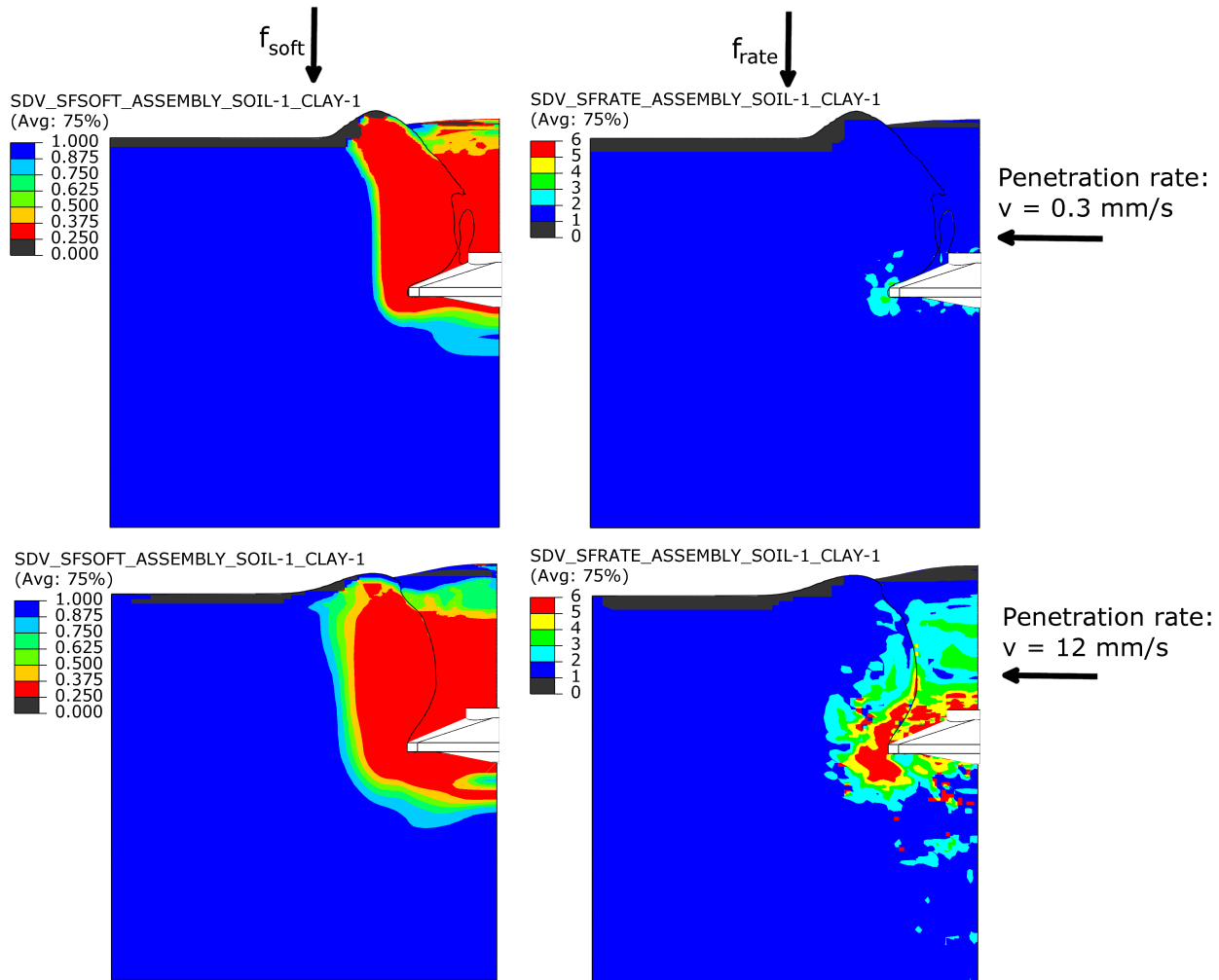


Figure 4.11: Deformed spudcan penetration FE-model at penetration depth D equal to 12,2 m. Contours are illustrating the softening and rate effect with f_{soft} and f_{rate} for penetration rates of 0,3 and 12,0 mm/s.

below the spudcan. By inspecting how the softening progresses in time during the penetration it is found that new shear bands are formed progressively with penetration. First a shear band is initiated and shear strain starts to localise in the mechanism as the spudcan is advancing downwards. When the spudcan advances even further a new shear band is initiated and develops, continuing this cycle.

Figure 4.12 is showing velocity vectors in the soil around the spudcan at a penetration depth D equal to 12,2 for penetration rates of 0,3 and 12,0 mm/s. The vectors indicate how the soil is flowing in the failure mechanism. It is seen that the soil failure resembles the deep type failure mechanism with local soil flow around the spudcan. It is also seen that the extent of the failure mechanism is different for the two penetration rates. For a rate of 0,3 mm/s the soil flow is concentrated in a smaller mechanism around the side of the spudcan, whereas for a rate of 12

mm/s the increased soil strength due to rate effects forces the mechanism to extend further out from the spudcan. From the deformed shape of the soil it is also evident that there is less backflow for a rate of 0,3 mm/s. For a penetration rate of 12 mm/s the cavity wall remains more intact, while for a rate of 0,3 mm/s the cavity wall is, to a greater degree, falling onto the spudcan.

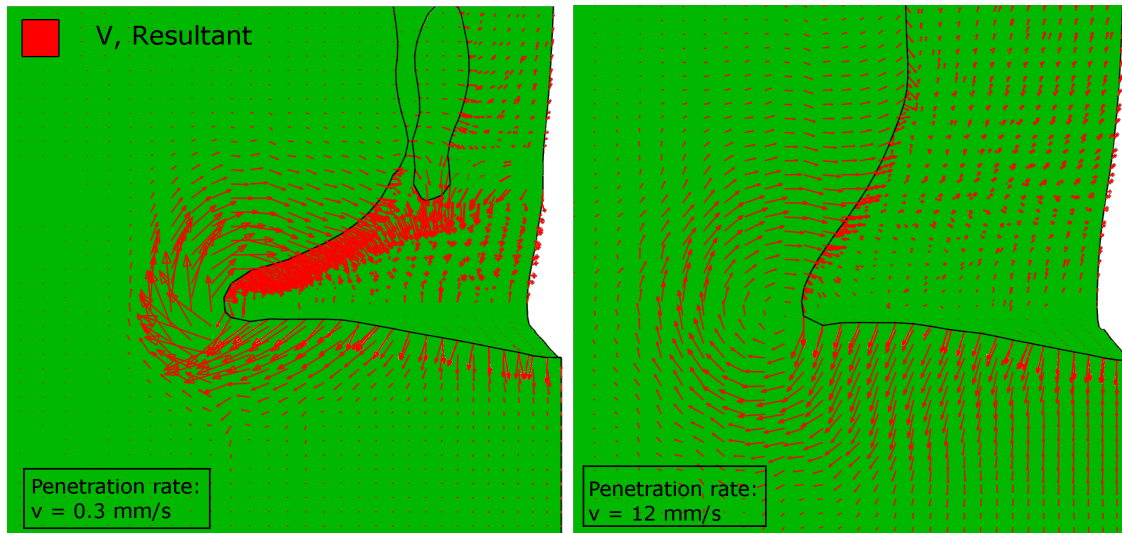


Figure 4.12: Velocity vectors in the soil during spudcan penetration at depth (D) equal to 12,2 m for two different penetration rates. The spudcan is not shown in the figure.

By inspecting how the velocity vector field, and with that the failure mechanism, in the soil changes during the penetration, information on when the failure mechanism is changing and when the onset of back flow starts can be obtained. In the first phase of the penetration the soil is pushed upwards by the spudcan forming a ridge around the cavity. In the next phase the ridge reaches its maximum height and the failure mechanism changes to a local flow around the spudcan. In the proceeding penetration the ridge may start to collapse into the cavity. For a penetration rate of 0,3 mm/s the transition between failure mechanisms happens at approximately D equal to 3,7 m, whereas for a rate of 12 mm/s this happens at approximately D equal to 7,7 m. Furthermore, the depth of transition from a shallow to deep failure mechanism is roughly the same at the ultimate cavity depth. Note that it is difficult to pinpoint for which exact depth the failure mechanism transitions from the FEA results as it is a gradual process.

The theoretical ultimate cavity depth, H_{cav} , can be calculated with eq. (2.10) which gives a theoretical cavity depth of 8,5 m. However, as noted in the literature review, H_{cav} may be reduced by 20-35% due to softening. Considering this the ultimate cavity depth will be 6,8 m to 5,5 m. Thus H_{cav} found from FEA is lower than the theoretical H_{cav} for a penetration rate of 0,3 mm/s, while for a penetration rate of 12 mm/s H_{cav} is larger than the theoretical prediction.

Although, the accurate theoretical cavity depth is uncertain when accounting for softening and rate effects.

4.5.3 Back-Analysis - Verification for DBC-JU1

To verify if the chosen back-calculation procedure and material parameters for softening and rate effects work for other locations, an additional back-calculation for location DBC-JU1 is undertaken. The analysis procedure and FE-model used is identical to that used for the back-calculation at DBB-JU1. Only soil layering and properties are changed. Geotechnical design parameters for DBC-JU1 are given in section 4.2.2 and in Table 4.4.

The measured spudcan load-penetration response at DBC-JU1 is presented in Figure 4.13(a) together with the results of the FE back-calculations. Figure 4.13(b) is showing the measured penetration rate for each of the legs. The PSF and SBA test where conducted as fast penetration tests, and the figure shows that these tests had a large penetration rate compared to the slow tests, i.e. the SBF and PSA tests. The slow tests have penetration rate around 0,35 mm/s after the

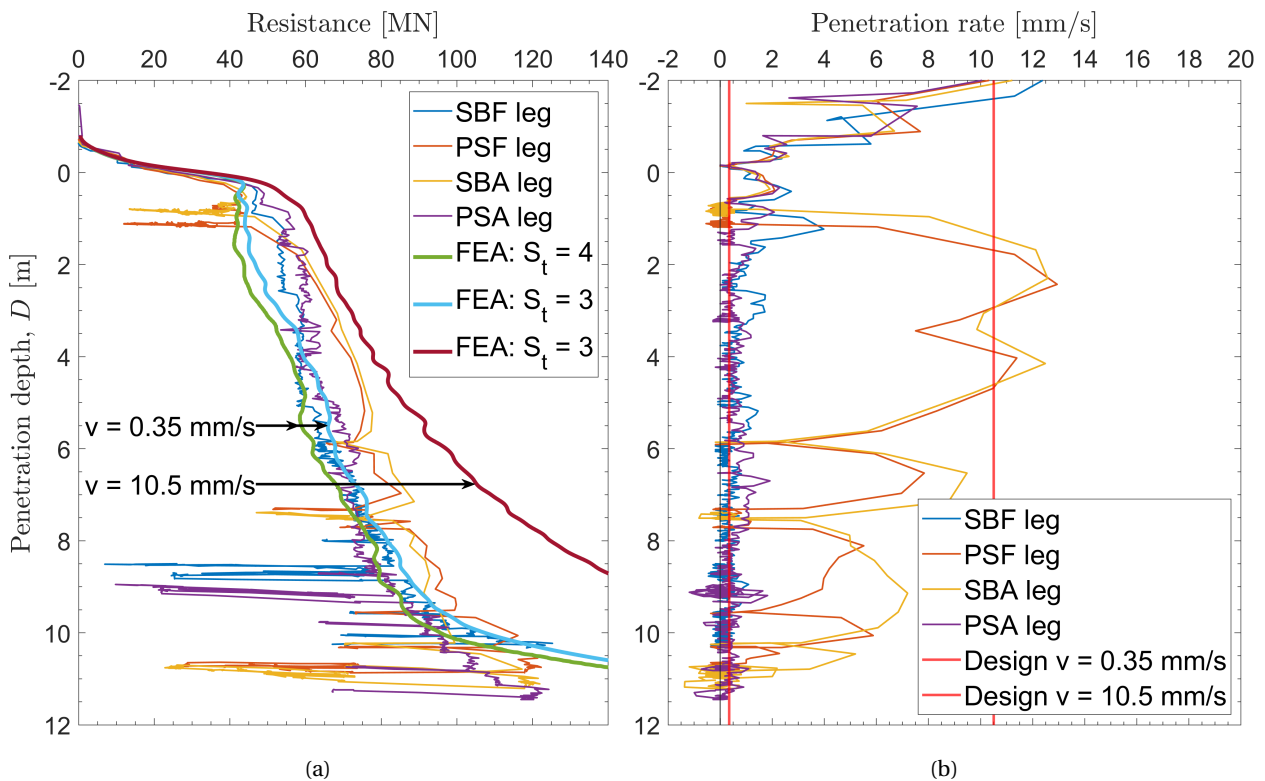


Figure 4.13: (a) is showing measured spudcan load-penetration response at DBC-JU1 together with load-penetration response from FE-analyses for two different penetration rates. (b) is showing the measured penetration rate during the spudcan tests. D is referring to the depth of maximum spudcan bearing area.

rates have stabilised, i.e. below 2 m depth. The fast penetration tests have varying penetration rate with rates around 10,5 mm/s during the fast loading steps. The fast penetration tests show a rate effect on the resistance, where the resistance in the fast tests are increased by about 15-25 % during the fast loading steps, compared to slow tests. All legs reach the maximum pre-load capacity of the jack-up of 122,6 MN below 10 m depth.

For the FE-analyses the base case softening and rate parameters are used ($S_t = 4$, $\xi_{95} = 1$, $\eta = 0,5$, $\beta = 0,4$ and $f_{rate}^{max} = 6$). However, using a sensitivity of 4 gave slightly lower resistance than the measured in the slow tests, therefore analyses with a sensitivity of 3 were done. Furthermore, the analyses was run with two different penetration rates. To match the slow penetration test a constant rate of 0,35 mm/s is used, and to match the fast loading steps of the fast tests a penetration rate of 10,5 mm/s is used. These rates are chosen based on the plotted rates in Figure 4.13(b).

The resulting load-penetration response from the FEA is shown in Figure 4.13(a). In general the FEA with a rate of 0,35 mm/s underpredicts the resistance in the top 4 m, but below 4 m the measured curves and curves from the FEA agree quite well. Sensitivities of 3 and 4 are giving resistance on the high and low side of the measurements, respectively. The curve corresponding to $S_t = 3$ gives best agreement above 7 m depth, while $S_t = 4$ gives better agreement below 7 m depth compared to the measurements from the slow tests. For the FEA with a penetration rate of 10,5 mm/s which is using S_t of 3, the resistance is higher than measured resistance for the fast tests. Thus, the rate effect may be slightly overestimated at DBC-JU1 when using the base case rate parameters. Though, it is expected that the base case rate parameters do not perfectly match because the clay at DBB-JU1 is different to DBC-JU1.

The stronger bottom sand layer begins at 11,3 m, which can be seen as an increasing rate of resistance with depth from around 9 m and below. This is most evident in the PSA and SBF curves. The presence of the bottom sand layer is also seen as an increased resistance in the FEA curves when the spudcan is approaching the sand layer. For the FEA with a penetration rate of 10,5 mm/s the increase in resistance due to the sand layer seems to happen at a shallower penetration depth, i.e. from 7-8 m. Whereas for the FEA with penetration rate of 0,35 mm/s this increase in resistance seems to happen from a round 9 m depth, similar to the measurements.

4.6 Discussion of Spudcan Back-calculations

In the following the results of the back-calculation for locations DBB-JU1 and DBC-JU1 are discussed. By using the same set of base case parameters for the softening and rate effects in FEA, a load-penetration response was obtained which is in reasonable good agreement with the measured response at both locations, for both slow and fast penetration tests. See Figure 4.6 and 4.13. The difference between FEA and measurements is varying with depth, and the measurements from different jack-up legs also vary. Moreover, the penetration rate in the spudcan tests are also varying. It is therefore less clear what a representable load-penetration response at the locations is for a given constant penetration rate. The variability in the measurements may be due to the generally large soil variability at Dogger Bank, differences in penetration rate and differences in the jacking procedure for each leg. For both locations the resistance from FEA is lower than the measured in the first 3-4 m of penetration. At DBB-JU1 the penetration rate was however larger in the first part of the test, and this may explain the larger resistance in the field measurements. At DBC-JU1 the reason for the higher resistance in the first part of the penetration is uncertain, as the initial penetration rate at this location is not much higher than for the deeper penetration. Possible reasons are the used jacking procedure, soil variability, and that the used soil parameters may work better for the deeper soil.

For DBB-JU1 the FEA with a penetration rate of 0,3 mm/s, in Figure 4.6, matches the SBF test best, and shows less resistance than the PSA test. The CPT-data in Figure 4.1 reveals that the CPT corresponding to the SBF test shows lower q_t values than the average for most depths. This spudcan test may therefore give lower resistance than what would be representable for the location as a whole. The q_t profile for the PSA leg is more in line with the design profile. Therefore, the FEA resistance is a bit lower than what the representative measurements would dictate. However, again, as the soil variability is large and the zone of influence is much larger for a spudcan than a CPT, it is not possible to draw assertive conclusions from the individual CPT-measurements regarding the load-penetration response.

It is important to keep in mind that the convergence study showed that the resistance is overestimated by approximately 7 % or more due to the used mesh density and penetration velocity which gives some dynamic inertia effects. Furthermore, the convergence study did not use a soil model which can describe strain softening or strain rate effects. Thus, it is possible that the current FE-model gives a solution that converges to a lesser degree than the convergence study indicates, when including strain softening and rate effects. Based on the known overestimation

and that the FEA provided a little low resistance, it can be concluded that the current FEA give too low resistance. Though, the variability in measurements is comparable to the deviation between the FEA and the measurements. Therefore, the discrepancy is not large compared to the general uncertainties in these back-calculations.

In the back-calculations N_{kt}^* was taken as 23, and other values were tested. The correct N_{kt}^* factor is uncertain due to the complex soil at Dogger Bank, but 23 was found to be the best estimate by NGI. In the current back-calculations it is difficult to assess the correct value since the resistance is also dependent on the uncertain softening properties of the soil. However, using N_{kt}^* equal to 23 gave reasonably good agreement with the measurements when applying the base case softening and rate effect parameters.

In the back-calculations, as a simplification, the effective unit weight of the soil, γ' , is taken as 9 kN/m^2 , although the average effective unit weight for the Upper Dogger Bank clay has an average γ' of $10,1 \text{ kN/m}^2$. This simplification is used since it is assumed that the initial stresses of the soil is of little importance for the spudcan resistance. However, eq. (2.8) [reading $Q_V = (s_u N_c s_c d_c + \sigma'_{v0}) A$] shows that the bearing capacity itself is dependent on the overburden stress and thereby γ' . Thus using a low γ' will give a lower resistance. However, hand calculations with eq. (2.8) using bearing capacity factors tabulated in [Hossain and Randolph \(2009b\)](#) shows that varying γ' from 9 to $10,1 \text{ kN/m}^2$ gave a difference in bearing capacity less than 1 %. Thus this simplification should not have any significant effect on the FE-analyses.

Strain Softening Effects

Strain softening effects are included in the back-calculations to account for the gradual remoulding of the soil flowing around the spudcan during the penetration. The effect of the softening parameters is shown in Figure 4.8(a), and it is evident that the softening can have a large impact on the soil resistance. For the back-calculations, base case softening parameters with S_t equal to 4 and ξ_{95} equal to 1 is used. The sensitivity of 4 is higher than the measured sensitivities for the clay, but as previously discussed in section 4.2.1 the measured sensitivity is uncertain. It is found that the resistance from FEA is a little low, and using a lower sensitivity would increase the resistance. Therefore using a sensitivity of for example 3 could yield better agreement with the measurements. For DBC-JU1 sensitivities of 3 and 4 gave similar agreement with the measurements.

In addition ξ_{95} also influences the penetration resistance. How quickly the soil is remoulded

is governed by ξ_{95} such that the relatively low used value of 1 is the reason why the soil flowing around the spudcan is fully remoulded, as seen in Figure 4.11. Others have estimated ξ_{95} to be around 10–25, but for Upper Dogger Bank Clay ξ_{95} is estimated by NGI to be around 1 based on triaxial tests. However this estimation also considered a sensitivity of 1,3. It is therefore uncertain if $\xi_{95} = 1$ is valid for the higher sensitivities used herein. Due to the lack of information for the true value of ξ_{95} from lab data this parameter may be the most uncertain in the back-calculations. Using other ξ_{95} -values could give good agreement with measurements with other combinations of softening and soil strength parameters.

The formation of shear bands is observed in the plots of stresses and of f_{soft} (fig. 4.10; fig. 4.11). Strain localisation and formation of shear bands or zones were also observed in the FE-simulation of a triaxial test. They form as a consequence of the softening incorporated in the analysis and a more complete discussion on the reason for the formation of such shear bands is given in section 3.2. Furthermore, in the triaxial simulations a counteracting effect where the rate effect counteract the strain localisation happening due to softening is observed. In the spudcan penetration analysis this counteracting effect seems to be smaller, since equally distinct shear bands are forming for both the slow and the fast spudcan penetration simulations. From the plots of f_{rate} , the rate effect seems to affect the areas of where the shear band is forming to a lesser degree, and this may be the reason for why this counteracting effect is not clearly observed for the spudcan tests.

Note that strain softening can give a spurious mesh dependency in FE-analyses where the shear band thickness and soil resistance become dependent on the used mesh refinement. Furthermore, when there is such a mesh dependency the FE-solution will not converge with respect to the mesh density. However for the triaxial FEA which included softening, the soil resistance did converge well for increasing mesh refinement. This could be due to the used CEL method where the material state parameters are not linked to an individual element since the material can move freely between elements. Moreover, including strain rate dependency with strain softening will counteract the mesh dependency (Zhou and Randolph, 2007). It is therefore assumed that spurious mesh dependency is not a problem for the current FEA, and this topic is not investigated further.

Although the correct value of the individual softening parameters which is used is uncertain, in combination they provide a load-penetration response which agree quite well with the measurements. The main objective of the spudcan back-calculations is to establish a description of the rate effect, and this objective can be met without finding precisely correct softening param-

eters.

Strain Rate Effects

To be able to back-calculate the rate effects observed in the spudcan penetration tests at Dogger Bank, strain rate effects are included in the FE-analyses. In the field measurements at DBB-JU1 increased loading rate gave an increase in resistance of 30-40 % which corresponds to approximately 22 % per log-cycle increase of loading rate. For DBC-JU1 the increase in resistance was 15-25 % corresponding to 14 % per log-cycle. Penetration velocities and relative increase in resistance were varying such that these percentages are approximate. Typically clays show an increase in strength of around 5-20 % per log-cycle increase in loading rate, thus the measured rate effect is close to typical values.

In the FE-analyses different rate effect parameters, i.e. η , β and $f_{\text{rate}}^{\text{max}}$, were tested to obtain a similar rate effect as observed in the field. This resulted in a set of base case rate parameters which gave a rate effect similar to the measurements. Initially rate parameters fitted to the empirical based NGI rate equation were tested. However, using these parameters gave far too low rate effects, and the base case rate parameters give a significantly larger f_{rate} -curve, as seen in Figure 4.7(b). However, the base case parameters, which were calibrated against the spudcan tests, were also used in the FE-analyses of triaxial compression tests, where the compression velocity and thus strain rate was varied. These FEA are similar to the real triaxial tests NGI have based their rate equation on. Interestingly, when using the base case parameters which give significantly more strain rate effects than the NGI equation, in triaxial tests the overall rate effect in the FEA is similar to the NGI equation, as shown in Figure 3.5. Therefore, using rate effect parameters which appear to be too high, and much higher than parameters estimated from laboratory tests, results in a rate effect which is very similar to empirical measurements when applied in a larger triaxial FE-model. Moreover, these base case rate parameters were solely calibrated against the spudcan tests, but are also agreeing well with physical triaxial measurements when applied to FE triaxial tests. This is a strong indication that the base case parameters give a rate effect which is realistic.

Why rate parameters which give a high f_{rate} -curve result in much lower and more realistic rate effects in total for a larger FE-model, such as models of spudcan penetration or triaxial tests, is difficult to pinpoint. One possibility is that there is something wrong in the implementation of the UWA-model in Abaqus\Explicit which gives a much lower rate effect than what would

be expected. Another reason could be due to some inherent difference between the triaxial tests where the rate effect is measured and how the rate effect behaves when those measurements are applied to constitutive models in FEA. Nevertheless, the current implementation of the UWA-model together with the base case rate parameters have been verified to work for both FE-analyses of triaxial tests and spudcan penetration.

To model different penetration rates in the FE-analyses the penetration rate in the FEA is not changed, but instead the reference shear strain rate, $\dot{\gamma}_{\text{ref}}$, is modified. This affects the computed strain rate effect applied to all soil movement in the model. Therefore, this has an unintended effect of giving rate effects and increased shear strength to soil movement other places in the model, such as to the cavity walls when they are collapsing during the penetration. This can be seen in Figure 4.11 where the cavity wall above the spudcan is also experiencing a rate effect. This will influence the deformation pattern and the ultimate cavity depth in the model. This effect is to some extent real as the soil being pushed by the spudcan is moving faster and therefore can be expected to experience a rate effect, but the parts of the soil which move due to gravity and is less effected by the spudcan penetration rate should not have such a rate effect.

In Figure 4.11 and 4.12 it is evident that the deformation pattern is different between the fast and the slow penetration. For a rate of 0,3 mm/s the spudcan is almost completely enveloped of soil, whereas for a rate of 12 mm/s the cavity wall is only bulging out and is much more intact. From the available information it is difficult to say if the large difference in deformed shape between the two penetration rates is realistic, but as the fast rate in the FEA is 40 times greater than the slow rate it is not unreasonable that the deformation pattern of the model changes due to the large difference in penetration rate.

Regarding the distribution of the rate effect in the soil, it is no surprise that the rate effect is greatest for the soil regions with the greatest soil rate or velocity, i.e close to the spudcan and inside the failure mechanism. For the fast test some rate effect is also seen in the deeper regions of the soil, indicating that the soil is developing plastic strains and failing. Thus the failure mechanism could be going deeper than what the plots of velocity vectors and f_{soft} would indicate. The contour plot of stresses also shows that the soil is mobilised deep below the spudcan.

When comparing the rate effect predicted by the FEA when using the base case rate parameters, the rate effect is underpredicted at DBB-JU1 and overpredicted at DBC-JU1. Thus the current base case rate parameters are a compromise and give fairly good agreement with measurements at both locations. The clay at DBB-JU1 is of the DBK_U_C unit while the clay at

DBC-JU1 is of the BCT unit, therefore, it is not unreasonable that the rate effect at the locations is different. When comparing the rate effect in the analysis with a slow penetration rate, to the analysis without rate effects, in Figure 4.7, it is seen that the slow test with a penetration rate of 0,3 mm/s has some strain rate effects which increases the resistance with approximately 10 %. It can be discussed if the rate effect is too large for the relatively slow penetration rate. It is therefore possible that the f_{rate} -curve corresponding to the base case rate parameters gives too much rate effect for the lower strain rates, and that these parameters could be optimised further such that there is less rate effect for lower strain rates.

Failure Mechanism and Backflow

The failure mechanism is seen in Figure 4.12 for a depth of 12,2 m, and appears to have localised to a soil flow around the spudcan. For the penetration rate of 12 mm/s the extent of the mechanism is larger than for a rate of 0,3 mm/s. This is because the rate effect gives larger resistance for higher soil velocities, therefore, the soil will develop a larger failure mechanism with lower soil velocities when the penetration rate increases. A larger mechanism will also generate more resistance such that a balance between failure mechanism size and soil velocity is automatically found in the solution process. The kinematic mechanism requiring the least energy will become governing.

As previously discussed the theoretically correct cavity depth is difficult to obtain when including strain rate and softening effects. Softening influences when the spudcan failure mechanism transitions from the shallow type to the deep local type. Also in general, softening will reduce the ultimate cavity depth, but this is partially counteracted by strain rate effects. This is observed in the current analyses as the fast penetration test gave a larger H_{cav} and less backflow. For the slow test H_{cav} is estimated to be 3,7 m, corresponding to the depth with onset of backflow, which is lower than the theoretical estimate. Thus, this can indicate that there is too much backflow in the current analysis due to a too high sensitivity. However, how the true spudcan failure mechanism in the fissured Dogger Bank clay is behaving is unknown, and even though the failure mechanism in the FEA may not be a complete description of reality, the load-penetration curve do agree with the measured response.

Looking at how the sand behaves, it is seen to fall into the cavity which seems realistic as the the top sand has little confining pressure. At DBC-JU1 there is also a deep sand layer which is evident in the load penetration response when the spudcan is approaching the bottom sand

layer, the resistance increases significantly. For the slow FE-penetration tests the sand layer is only felt by the spudcan when the spudcan is around 2 m or less above the sand layer. For the fast penetration FEA the bottom sand layer is felt much earlier, around 4-5 m before the sand layer. This is likely due to the large failure mechanism in the fast penetration analysis, which will then mobilise the sand strength in an earlier stage of the penetration. The effect of soil layering is not the primary interest in this thesis, and the subject is not further discussed.

4.7 Summary of Back-Calculation

Back-calculations of spudcan penetration tests from locations DBB-JU1 and DBC-JU1 were undertaken to establish strain softening and rate effect parameters. At both locations, the spudcan penetration tests included two slow tests and two fast tests with a penetration rate 30-40 times greater than the slow tests. The penetration rate was varying for the fast tests. The resistance was increased by approximately 22 % per log-cycle of increase in loading rate at DBB-JU1 and by approximately 14 % per log-cycle at DBC-JU1. This increase due to strain rate effects is close to typical values for clay. To account for the large deformations occurring during spudcan penetration and to incorporate strain softening and rate effects, the coupled Eulerian-Lagrange (CEL) approach was used with the UWA soil model in the finite element analyses.

To back-analyse the spudcan penetrations in FEA, strain softening and rate parameters were selected by trial and error guided by available data. Representative penetration rates were selected by engineering judgement and average values based on the varying penetration rates recorded from the jackup operations. The final base case parameters adopted ($S_t = 4$, $\xi_{95} = 1$, $\eta = 0,5$, $\beta = 0,4$ and $f_{rate}^{max} = 6$) did not provide an exact match to each of the penetration tests, though gave reasonably good agreement with the measurements when considering the variability in recorded resistance, soil properties and penetration rate.

The softening parameters were difficult to assess accurately, especially ξ_{95} . ξ_{95} is the cumulative plastic shear strain required for 95 % remoulding. It was found that the softening parameters had a great impact on the resistance. Since the resistance in the FE-analyses was a little low, the sensitivity of 4 might be too high. For DBC-JU1 S_t of 3 was tested and gave a similar agreement with measurements as S_t equal to 4. In conclusion, there is some uncertainty in the accuracy of the base case softening parameters, but they provide an acceptable result together with the other parameters.

The base case rate parameters give a rate effect on the resistance which is in reasonable

agreement with the measured spudcan penetration resistance. To obtain a large enough rate effect, the base case parameters had to be adjusted to higher values than the values based on physical triaxial tests. However, when the base case rate parameters are used in an FE-model of a triaxial test, the resulting overall rate effect is similar to measurements from real triaxial tests. Thus, the base case rate parameters which might appear to be too high, give good agreement with the rate effect measured in experiments when applied to larger FE-models.

In the back-calculations N_{kt}^* was taken as 23 based on other back-calculations carried out by NGI, and the base-case softening and rate parameters were calibrated to the measurements using this N_{kt}^* -value. It is uncertain if N_{kt}^* equal to 23 is correct, and therefore, other values were tested. As the effect of changing either N_{kt}^* , S_t or ξ_{95} is similar to changing one of the others, it is difficult to determine the correct value for the individual parameter. Though, a combination of parameters which gives a satisfactory result was found.

The failure mechanism in spudcan FEA was found to transition from shallow type to deep type, thus agreeing with the theory. The ultimate cavity depth observed in the analyses changed with penetration rate, and the ultimate cavity depth may have been too low due to too much softening. The ultimate cavity depth was challenging to accurately predict by analytical methods and to determine from FEA. Nevertheless, the obtained load-penetration response is in acceptable agreement with the measurements.

The main objective of the back-calculations was to calibrate rate effect parameters with spudcan penetration tests such that these rate parameters can be used to study rate effects for the lateral capacity of monopiles. It is concluded that this objective has been met and that the base case rate parameters, η equal to 0,5, β equal to 0,4 and $f_{\text{rate}}^{\text{max}}$ equal to 6, have been proven to give rate effects similar to observations from triaxial tests and spudcan penetration tests when used in the current finite elements models. The fact that these parameters work for both small triaxial tests and large spudcan tests indicate that they are also applicable to monopiles. The spudcan back-calculations were not able to provide accurate softening and strength parameters for the soil, but those parameters are of less importance in the forthcoming study of the relative rate effect on the lateral resistance of monopiles.

Chapter 5

Rate Effect on Lateral Capacity of Monopiles

As shown in the literature review, strain rate effects can increase the capacity of monopiles in clay for rapid loading. To investigate this subject, finite element analyses of a laterally loaded monopile in clay with varying loading rates are presented in this chapter. First laterally loaded monopile and spudcan penetration failure mechanisms are compared to verify that results from spudcan back-calculations can be used in analyses of monopiles. Next, an FE-model of an embedded monopile is established and the lateral capacity is found for different pushover rates. The objective of the analyses is to quantify rate effects on the lateral capacity of monopiles.

5.1 Problem Formulation

The aim of the FEA is to simulate the response of an offshore monopile subjected to lateral wave and wind loading. The considered design case is for a monopile situated at Dogger Bank (DB) in a design storm. Typical monopile dimensions for DB is used, with a realistic load case for DB. The analysis will consider the case where a single storm wave pushes over the monopile leading to large strain rates in the soil with accompanying strain rate effects. Furthermore, the analyses will investigate the effect of different pushover rates.

The specific design properties were obtained through communication with DNV. The monopile diameter, D_p , is set to 8,6 m which is a potential size considered for the Dogger Bank offshore wind project. The embedment depth, L , is set to 30,1 m corresponding to $3,5D_p$. Typically for DB and similar locations in the North Sea is L/D ratios around 3 to 4. The analyses will consider a lateral point load applied 55 m above the seabed from a storm wave with a time period T of 12 s, which is a typical storm load case in the ultimate limit state at the Dogger Bank area.

In the FE-analyses the results of the spudcan back-calculations are utilised, and therefore it is sought out to use an FE-model for the monopile analyses which is similar to the FE-model used in the spudcan analyses. Therefore, the CEL approach is used with Abaqus\Explicit in the monopile analyses, and the used soil layering and properties are similar to location DBB-JU1. Furthermore, the UWA-soil model is used to incorporate both strain rate and softening effects. The effect of cyclic degradation is not considered for this study. The main purpose of the FE-analyses is not to give accurate prediction of the lateral capacity for a certain monopile, but rather to quantify the relative rate effects. Hence, some simplifications are made to the model.

5.2 Comparison of Spudcan and Monopile Failure Mechanism

The monopile analyses utilise soil properties, i.e strength, softening and rate effect properties, obtained from spudcan penetration back-analyses. It is therefore investigated if the failure mechanism of a laterally loaded monopile is similar to the failure mechanism of a penetrating spudcan. This has previously been examined by [DNV GL \(2020\)](#). They compared modes of shearing and the size of the failure mechanism in FE-analyses of a laterally loaded monopile with an L/D_p ratio of 6 and a penetrating spudcan with a bearing area of 107 m².

Plots of displacement vectors and deviatoric strain from their analyses are shown in [Figure 5.1](#), and the modes of shearing is indicated in the figure. As concluded by [DNV GL \(2020\)](#) and seen from the figure, both failure types are dominated by shearing in extension (TXE) and direct simple shear (DSS). Moreover, the soil volume involved in the failure mechanisms are of similar size. This indicates both failure types may experience similar scale effects due to fissures and weaknesses in the soil, and that the operational shear strength determined for spudcans are applicable to monopiles. [NGI \(2020a\)](#) are in general agreement with these assessments. Furthermore, as the failure mechanisms and soil volumes are alike for both cases it is assumed that strain softening and rate effect parameters determined from spudcan analyses can be transferred to the monopile analyses.

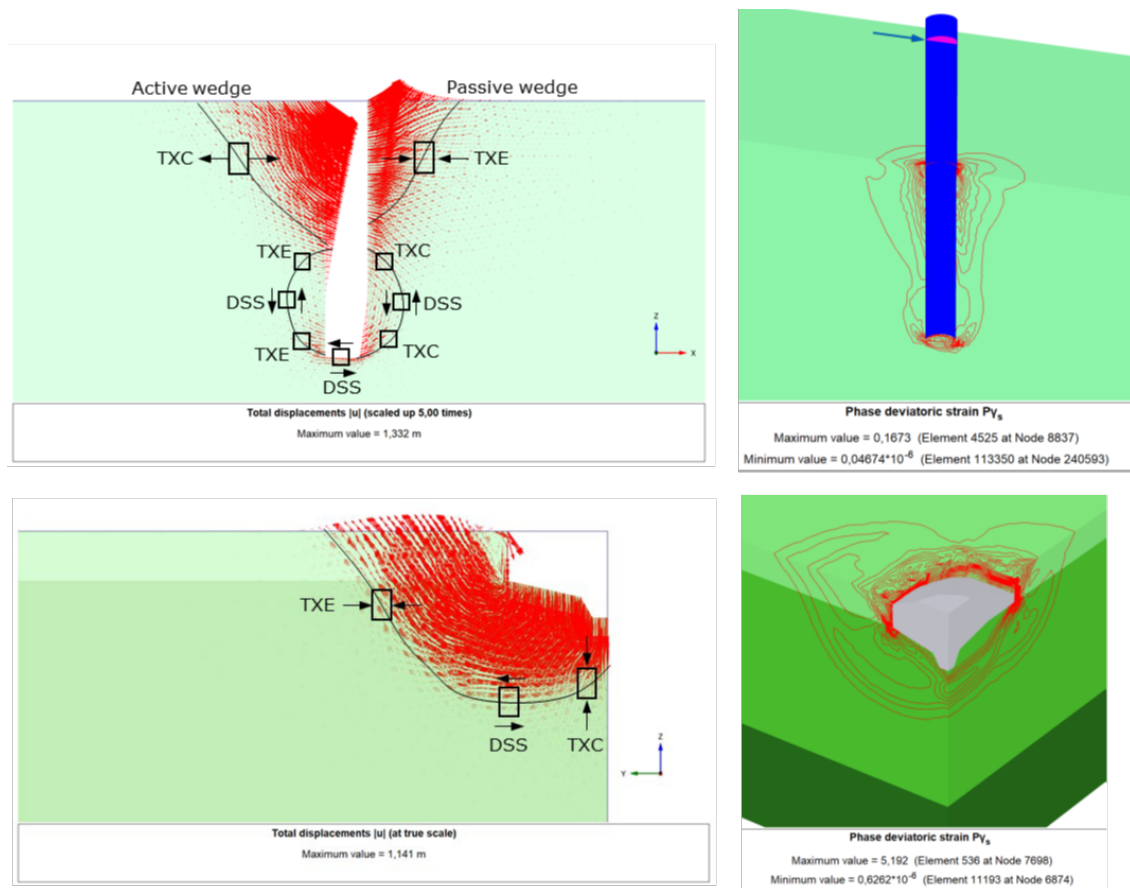


Figure 5.1: Comparison of failure mechanisms for spudcan penetration and laterally loaded monopiles, and mode of shearing. The figures are showing displacement vectors and deviatoric shear strain. Taken from [DNV GL \(2020\)](#).

5.3 Monopile Finite Element Model

The FE-model is created and analysed with Abaqus\Explicit using the CEL method ([Abaqus, 2019](#)), as described in section 2.6. To model the soil and to account for strain softening and rate effects the UWA model is used. Due to the symmetry in loading and geometry only half of the problem is modelled to limit the computational time.

The model consists of a cylindrical Eulerian soil domain with an embedded monopile modelled with Lagrangian elements. The radius of the soil domain is set equal to $4D_p$ in the analyses, after testing of various soil radii. The embedment depth of the monopile is set to $3,5D_p$, and the soil continuum extends $2D_p$ below the pile, giving a total height of the soil domain of $5,5D_p$. To allow for free soil heave during the analysis a 2 m thick void layer is added on top of the soil. The monopile has a diameter, D_p , equal to 8,6 m, and extends 55 m above the top of the soil to where the lateral load is measured. Thus, the monopile has a total length of 85,1 m. As a simplification,

the monopile is modelled as a rigid body and controlled by a reference point at the top of the pile. A rigid body is considered a reasonable simplification given the purpose of studying the relative effect of loading rates. The monopile is modelled as weightless in the soil by setting the pile weight equal to the weight of displaced soil. The model is shown in Figure 5.2.

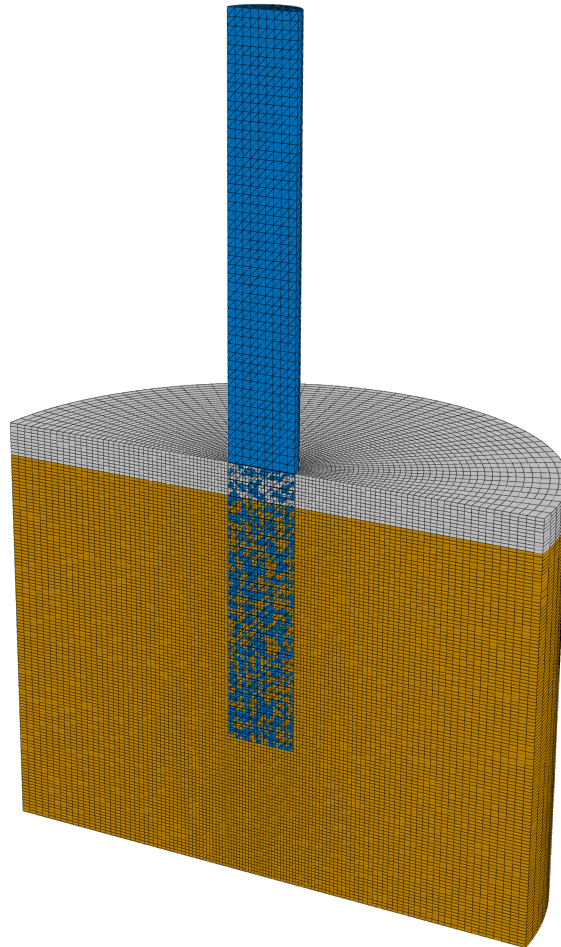


Figure 5.2: FE-model used for monopile pushover analysis and FE-mesh. The void and soil domain is indicated with different colours.

The soil domain is meshed with 8-node linear Eulerian brick elements with reduced integration and hourglass control, named EC3D8R in the Abaqus element library. The mesh density is similar to what was used in the spudcan back-analyses. It is assumed that the mesh density which was verified for the spudcan analyses also is sufficiently fine for the monopile FEA. No further verification of the FE-mesh is done for these analyses. Thus, a similar meshing strategy and mesh density as in the spudcan analyses is adopted for these analyses, with a finer refinement close to the monopile and a gradual increase in element size towards the circumferential border of the model. The smallest and largest element side length is approximately 0,4 m and

2,4 m, respectively. This resulted in a mesh with 368 768 elements for the Eulerian domain (soil and void domain). For the monopile 10-node quadratic tetrahedral elements, C3D10M, with approximate side lengths of 1 m are used. This gave 15 874 elements for the monopile. As the monopile is modelled as a rigid body, the pile mesh properties are of lesser importance and further verification of the pile mesh is not carried out.

For boundary conditions zero velocity in the vertical direction is prescribed on the bottom boundary. The circumferential boundary is prescribed zero velocity in both horizontal directions, and the plane of symmetry is prescribed zero velocity normal to the plane. The soil at all vertical borders are free to move vertically. As this is an explicit CEL analysis all boundary conditions have to be on velocities.

The FEA consist of three steps. In the initial step the model is established with boundary conditions and material definitions. Next a gravity step is introduced where gravity is defined and initial stresses are prescribed through a geostatic stress field. The duration of the gravity step is set to one second to allow the analysis to establish equilibrium between the gravity load and initial stresses. The gravitational acceleration is set to 10 m/s^2 , and the pile is completely fixed during this step, but the vertical DOF for the pile is free. In the final pushover step the top of the monopile is given a constant lateral velocity parallel to the plane of symmetry. During the pushover step the monopile is only allowed to move parallel to the plane of symmetry to maintain the symmetry of the model. Other movements and rotations are not allowed. Furthermore, the horizontal displacement at the top of the pile and at the seabed, and pile rotation is measured. The reaction force needed to displace the monopile at the pile top is also recorded. The duration of the pushover step is modified to give the desired monopile displacement.

In the initial stage of the analysis the Lagrangian monopile is wished in place in the Eulerian mesh, replacing the material in the area occupied by the monopile by void material. This is to avoid that a volume can be filled with both pile and soil. To define which volume is occupied by the pile in the Eulerian mesh, the volume fraction tool available in Abaqus is used. This tool calculates the Eulerian volume fraction (EVF) of soil for each element in the model. Giving EVF-soil of zero for the Eulerian elements filled with pile, and $\text{EVF-soil} < 1$ for elements that are partially filled with pile. With this method the Eulerian mesh do not have to conform to the monopile shape, and a regularised Eulerian mesh can be used in the area occupied by the pile. During the analysis the general contact algorithm, as described in section 2.6.1, is used to model the contact between the soil and monopile. This algorithm ensures that no soil will flow into the volume occupied by the monopile. The tangential behaviour is governed by a shear

stress limit, τ_{\max} , which is set equal to the average remoulded shear strength of the soil from the top of the soil layer down to the bottom of the monopile. The friction coefficient, μ , is set to a high value of 10^4 to allow τ_{\max} to govern the tangential interaction. This is equivalent to the tangential interaction properties used for the spudcan FEA. It is worth noting that this contact formulation as used here is not capable of transferring tensile stresses between the pile and the soil. Therefore, the soil will not stick to the pile when it moves away from the soil.

To ease the interpretation of the analysis output, the measured reaction force obtained for the analysis is filtered with the Butterworth filter to remove noise in the data. The filter is described in section 2.6.4, and a filter order of 2 is used with a cut-off frequency of 5 Hz. The filtered data was verified to match the unfiltered data.

To model different pushover rates the approach described in section 2.4.2 is used. The normalised loading rate, v_n , is calculated as

$$v_n = \frac{v}{\dot{\gamma}_{\text{ref}} D_p}$$

whew v is the lateral velocity of the pile top and $\dot{\gamma}_{\text{ref}}$ is taken as 3 %/hr. In the FEAs the prescribed velocity, v_A , is set to 2,0 m/s and $\dot{\gamma}_{\text{ref}}$ is changed to account for the real loading velocity or rate.

5.4 Geotechnical Parameters for Monopile Analysis

The simulated soil profile for these analyses is that of DBB-JU1, and the same design parameters as used in the spudcan analyses are adopted here. Geotechnical parameters for DBB-JU1 is discussed in section 4.2.1. The main objective is to study rate effects in clay, therefore, the relatively thin top sand layer of 1 m is not included in the monopile analyses. The sand layer from 0-1 m depth is replaced by a homogeneous clay layer with the same properties as the clay at 1 m depth. To obtain the s_u -profile the design- q_t determined for the spudcan analyses is used with N_{kt}^* of 23, similar to the spudcan back-analyses. However, the soil continuum extends deeper in the monopile model than in the spudcan penetration model. Hence, the q_t - and s_u -profile must be defined down to a deeper depth.

One CPT extends deeper than 15 m, and this CPT is used to extend the design profile. The q_t -profiles are shown in Figure 5.3, and show that there could be sand layers or pockets below 30 m. This sand is neglected in the monopile analyses and the soil is modelled as clay. The design q_t -profile is fitted to the measurements in clay as indicated in the figure, and the design profile

is tabulated in Table B.1.

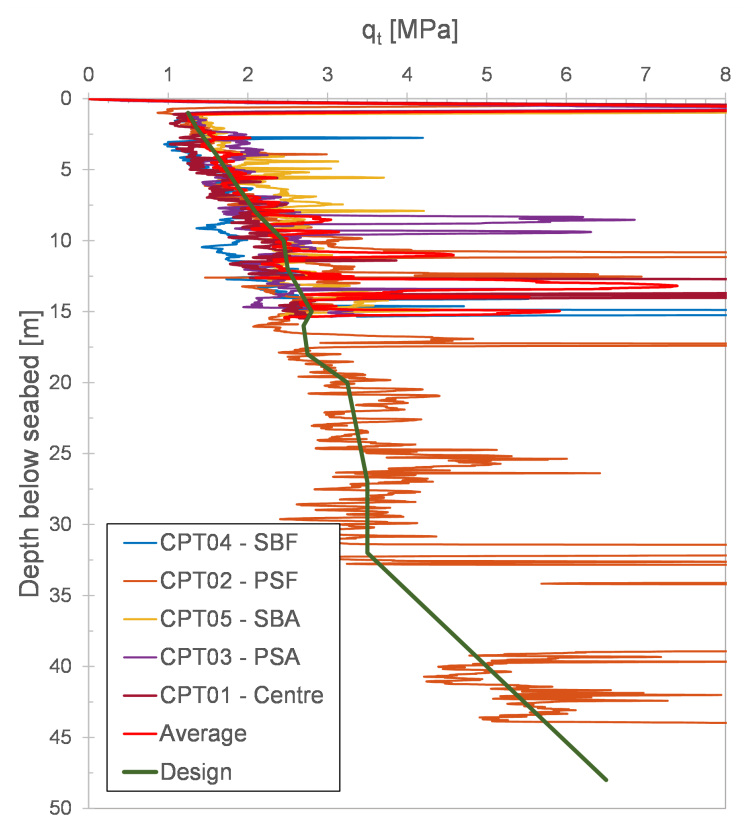


Figure 5.3: Measurements from CPTs, average q_t -profile and design q_t -profile.

For the spudcan analyses it was found that the elastic stiffness of the soil was of little importance, but the soil stiffness is probably more important for the response of a laterally loaded monopile. The soil stiffness will govern the initial response of the monopile before a plastic failure mechanism has developed. The strain rate effect in the UWA model is viscoplastic and is therefore governed by plastic strains after the soil has yielded. Since the main objective of this analysis is to quantify the rate effects, the initial response is of less interest. Therefore, an elastic stiffness of $200s_u$ is used, like in the spudcan back-calculations. As this may be a low stiffness the initial monopile resistance may also be low. For the spudcan analyses it was found that K'_0 had no impact on the spudcan response. For the monopile analyses it is assumed that K'_0 has little influence of the lateral resistance. Hence, K'_0 is taken as 1,0. Furthermore, the effective unit weight of the soil is used in the analyses and taken as 9 kN/m^3 , like in the spudcan analyses.

For the modelling of strain softening and rate effects the base case values for S_t , ξ_{95} , η , β and $f_{\text{rate}}^{\text{max}}$, are used since they gave reasonably good agreement with spudcan penetration tests. A summary of the geotechnical design parameters used for the monopile FEAs are given in Ta-

ble 5.1

Table 5.1: Geotechnical parameters and soil layering used for the monopile FEAs. z_{top} and z_{bot} refer to depth to the top and bottom of the layer below the seabed.

z_{top} [m]	z_{bot} [m]	soil type	soil unit	γ' [kN/m ³]	E	ν	K'_0	S_t	ξ_{95}	η	β	$f_{\text{rate}}^{\text{max}}$
0,0	48,0	clay	DBK_U_C	9	200 s_u	0,495	1	4	1	0,5	0,4	6

5.5 Monopile Analysis and Results

The monopile pushover FE-analyses are described in the following. To verify that the radius of the soil domain, R , of $4D_p$ is large enough to avoid boundary effects, analyses with radii of $3D_p$ and $5D_p$ is undertaken. In these analyses the pile head velocity is set to 2 m/s, and a Tresca soil model without softening or rate effects is used. For the radial boundary check, the mesh density was kept approximately constant with the same rate of increase in element size towards the boundary. However, the mesh was slightly less refined for the analysis with a radius of $3D_p$. The resulting monopile moment at seabed versus monopile rotation from the analyses with varying radius is presented in Figure 5.4. The moment was obtained as the measured force at the pile top times the pile height above the seabed. From the figure it is evident that R equal to $3D_p$ gives less resistance than the two larger radii. The analyses with R equal to $4D_p$ and $5D_p$ are practically identical, thus confirming that R equal to $4D_p$ is sufficiently large. The reason that a smaller radius gives less resistance is likely due to the boundary condition of free vertical soil movement at the circumferential boundaries, limiting the extent of the failure surface and hence resistance.

To assess the performance of the model the initial stresses after the gravity step is checked. A plot of the vertical initial stresses is shown in Appendix C, Figure C.2. The figure shows that the initial vertical stresses are comparable to the theoretical stress $\gamma'D$. There are however some deviations from this due to disturbances from the monopile. The vertical stress has minor lateral variations, and it is oscillating around the correct value during the gravity step. Below the pile there is a disturbance in the stress field with stress concentrations around the pile perimeter. This happens because the pile is modelled as infinitely stiff, in contrast to the soil. Therefore, the vertical stresses from the pile are mainly transferred to the soil along the pile perimeter. It is concluded that the initial stresses are sufficiently correct to give a reliable lateral resistance in the FE-analyses.

To study rate effects, monopile analyses with UWA soil model is carried out using the base

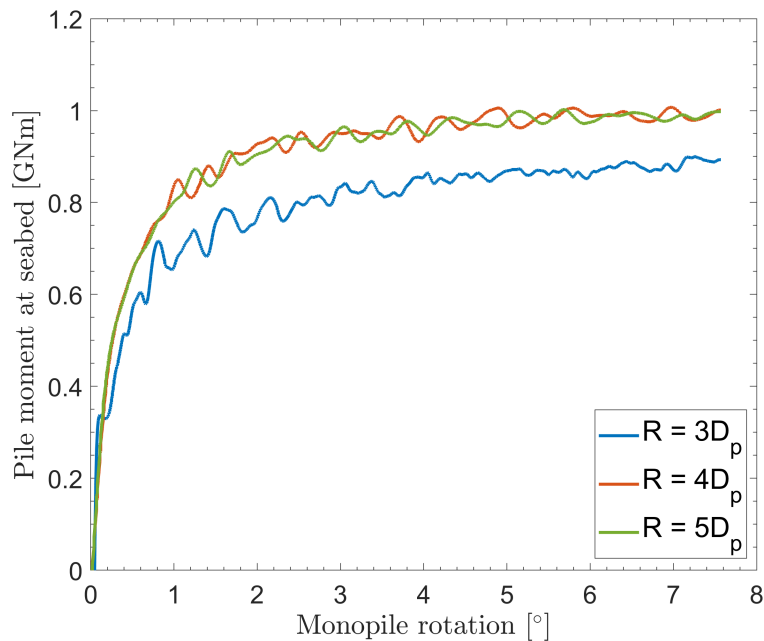


Figure 5.4: Moment versus rotation from monopile analyses with different soil domain radii.

case softening and rate parameters as given in Table 5.1. To model the ULS case consisting of a storm wave mobilising the full lateral resistance of the soil, and pushing over the monopile during one wave, an equivalent pile top velocity needs to be established. The lateral wave load is varying as a harmonic function with a time period, T , of 12 s, and the maximum load is therefore reached after $T/4$ or 3s. It is assumed, based on preliminary analyses, that the maximum resistance is mobilised after the monopile has rotated 5° . This results in an equivalent pile top velocity of 2,2 m/s. A reference a velocity corresponding to a slow load case is also established. For this the loading rate used in the PISA monotonic load tests is used. The PISA load tests had a lateral ground velocity of $D_p/300$ / min for most loading steps, equivalent to a pile top velocity of 0,0017 m/s in this case (Byrne et al., 2020). Additionally, pile top velocities of 0 (no rate effect), 0,1 and 1,0 m/s is analysed.

As previously discussed, in the FE-model the prescribed pile top velocity is constant in all analyses. This velocity has to be sufficiently low to avoid inertia effects and high enough to give an acceptable computational time. For these analyses the pile top velocity is set to 2,0 m/s. This gives velocities in the soil of less than 1 m/s which are lower than the soil velocities in the spudcan FEAs, which were verified through a convergence study. Thus, it is assumed that a pile top velocity of 2 m/s is sufficiently low to avoid inertia effects. The real monopile pushover rate is modelled by changing $\dot{\gamma}_{\text{ref}}$. To verify that the adopted pile top velocity is sufficiently low, the kinetic energy in the analyses was checked and it is found that the kinetic energy in the soil

is less than 5 % of the internal energy (strain energy, plastic dissipation etc.) for most of the analysis time. Only in the early stages of the analysis is the ratio of kinetic energy to internal energy larger, going up to 10 %. As the kinetic energy is low, it is concluded that using a pile top velocity of 2 m/s is acceptable.

Displacement versus lateral resistance force and rotation versus moment curves from the monopile pushover analyses are shown in Figure 5.5. From the figure it is evident that larger loading rates give larger resistance. In the initial phase of the analysis before a failure mechanism has evolved, the rate of increase in resistance with displacement is steep. When a failure mechanism has been established the curves flatten out and eventually reach a plateau corresponding to the ultimate capacity. The ultimate capacity is reached at around 5-6° pile rotation or around 2 m ground displacement for the three largest loading rates. For the two lowest loading rates, i.e. 0 and 0,0017 m/s, the peak resistance is reached after approximately 2° rotation or 1,0 m of ground displacement, and after this the resistance slightly decreases due to softening. This post peak reduction in resistance is not observed for the faster loading rates since these analyses have more rate effects which counteracts the softening. When increasing the pile top velocity from 0,0017 m/s to 2,2 m/s the resistance is increased by 35 % for 3° rotation. This corresponds to 11 % increase in resistance per \log_{10} -cycle increase in loading rate. Comparing the resistance for loading rates of 0,1 and 2,2 m/s at 3° rotation shows an increase in resistance of 16 % per log cycle increase in loading rate. Thus, the increase in resistance is not directly proportional to the logarithm of loading rate increase.

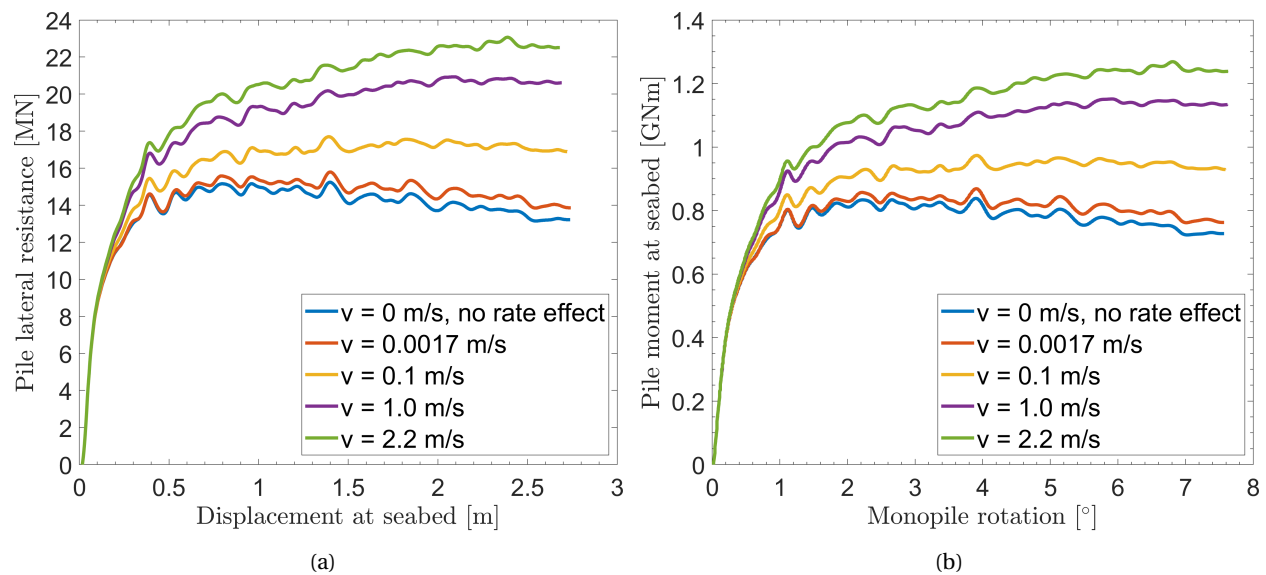


Figure 5.5: Monopile response to lateral loading for different pile top lateral velocities, v , in FE-analyses. (a) displacement versus resistance force and (b) moment versus rotation.

To better understand the performance of the FE-model, contour plots of stress, strain, f_{soft} , f_{rate} and a plot of velocity vectors are presented in the following. The figures are showing plots from the monopile analysis with the largest pile top velocity, equal to 2,2 m/s, for a monopile rotation of 5,3°. Figure 5.6 is showing contour plots of Tresca stresses, and it is seen that the soil strength is mobilised on the back and front side of the monopile. Due to high strain rates in some regions close to the pile these regions experience large rate effects and therefore have large stresses. Tresca stresses close to the border are relatively low, which indicates that there is little boundary effects. Thus, confirming that the soil radius is large enough. Stresses at the bottom boundary are also low, indicating that the height of the soil domain is sufficient.

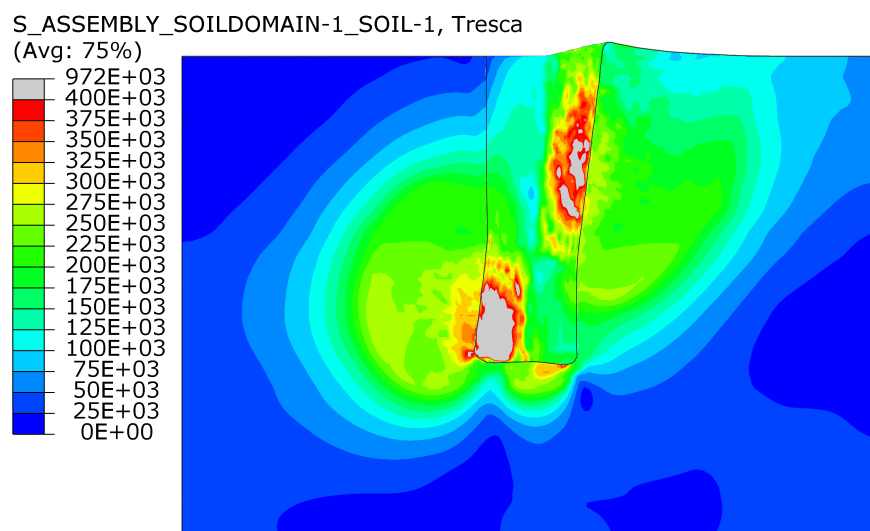


Figure 5.6: Contour plot of Tresca stress $[= \sigma_1 - \sigma_3]$ for the monopile FE-analysis with $v = 2,2$ m/s at $5,3^\circ$ rotation. Stress in Pa.

Figure 5.7 is showing contours of cumulative plastic shear strain, ξ , and it is seen that only smaller regions have developed significant plastic strains. The monopile is also included in this figure, and shows gaps forming in the regions where the pile moves away from the soil. The gaps are forming as a consequence of the contact formulation which is not able to transfer tensile stresses.

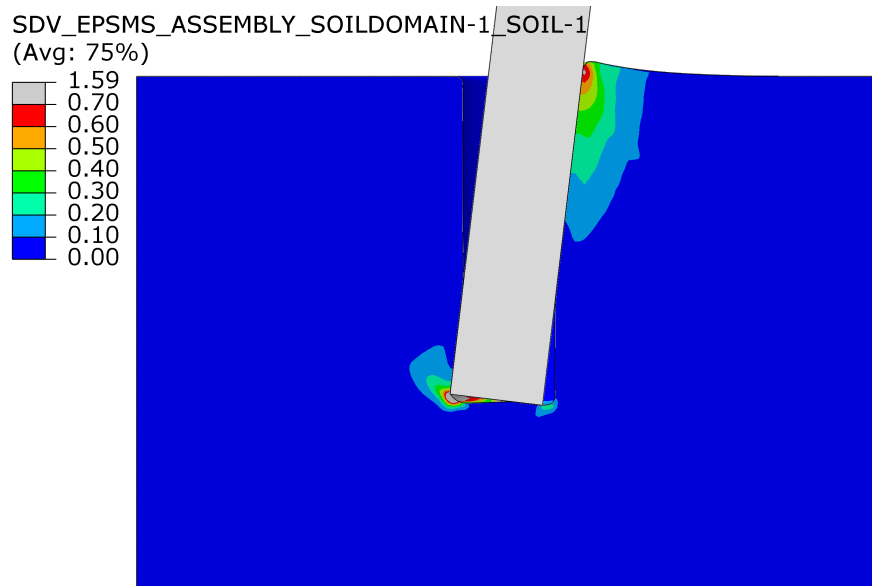


Figure 5.7: Contour plot of cumulative plastic shear strain, ξ , for the monopile FE-analysis with $v = 2,2$ m/s at $5,3^\circ$ rotation.

Figure 5.8 and 5.9 are showing contours of f_{soft} and f_{rate} , respectively, for the monopile analysis. These factors show how the shear strength is scaled due to strain softening and rate effects, as described in section 2.4.1. Since the softening effect is a function of ξ it is seen that the areas which has developed most plastic strain also have softened the most. Here, S_t is equal to 4 such that the minimum value of f_{soft} is 0,25. However, most of the soil which has softened has $f_{\text{soft}} > 0,5$. The contours of f_{rate} in Figure 5.9 show that significant areas of the soil experience a rate effect, with high values of f_{rate} going up to $f_{\text{rate}}^{\text{max}} [= 6]$. Most of the rate effect is located close to the pile, but there is also high f_{rate} -values in some elements at a distance away from the pile. Possibly corresponding to where the soil is failing. The high f_{rate} -values are the reason for the increased lateral resistance for the analysis with a pile top velocity of 2,2 m/s in Figure 5.5.

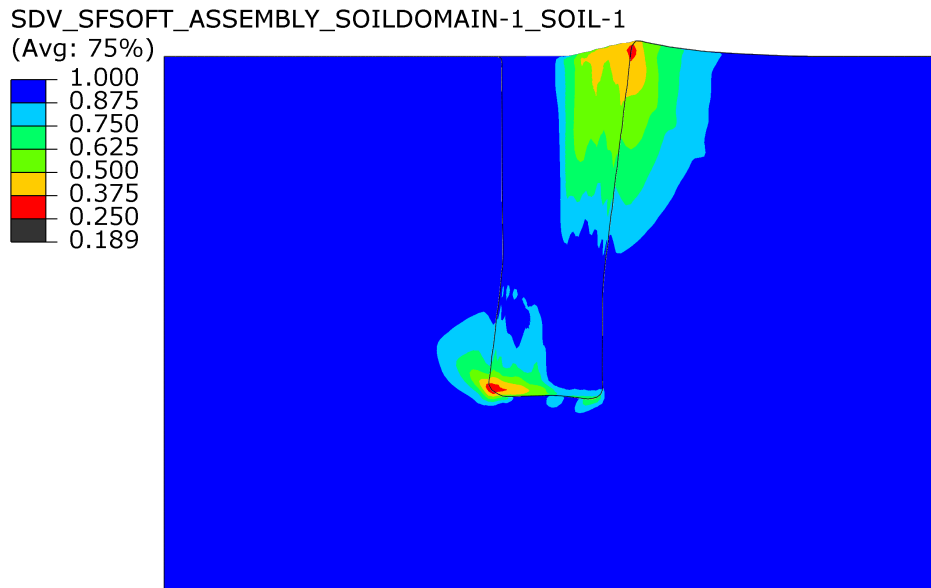


Figure 5.8: Contour plot of f_{soft} for the monopile FE-analysis with $v = 2,2$ m/s at $5, 3^\circ$ rotation.

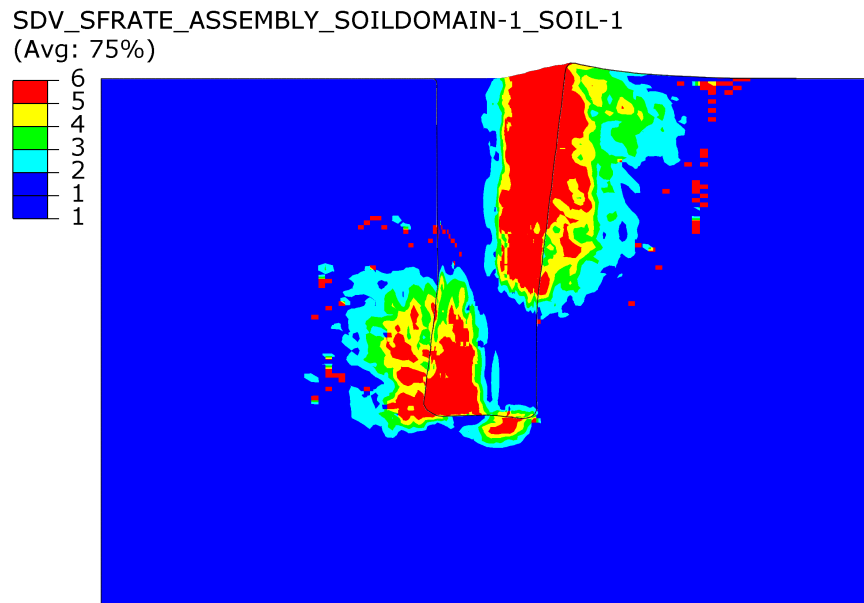


Figure 5.9: Contour plot of f_{rate} for the monopile FE-analysis with $v = 2,2$ m/s at $5, 3^\circ$ rotation.

Velocity vectors in the soil at $5,3^\circ$ pile rotation are shown in Figure 5.10. The figure shows how the soil moves within the failure mechanisms. On the front side of the pile the soil seems to move as passive failure wedge, and a fairly abrupt transition in velocity magnitude can be seen between the soil inside and outside of the failure mechanism. Behind the pile a circular shaped failure mechanism can be seen in the area where the toe of the pile is kicking back into the soil. The soil is moving out from the pile and moving back in further up. A rough indication of these failure mechanisms is shown in the figure. It is also seen that soil is pushed up in front of the pile to form a smaller ridge.

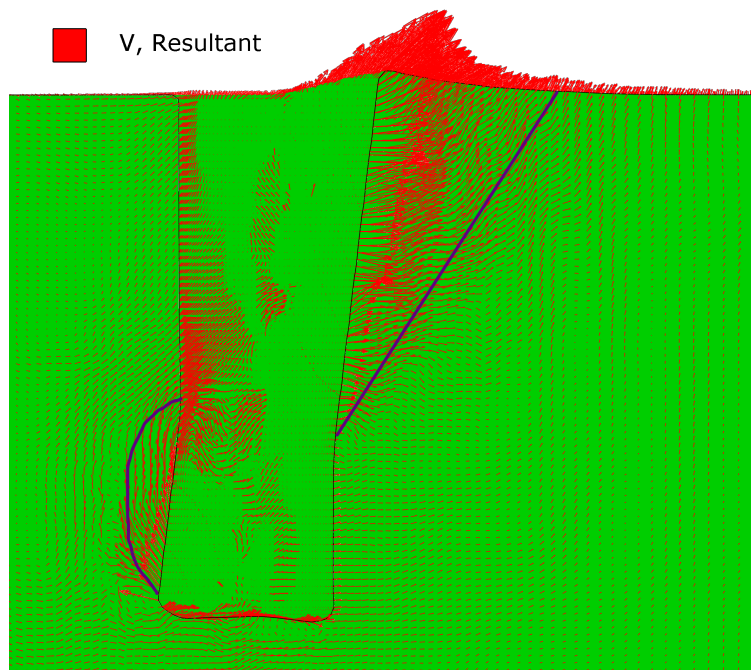


Figure 5.10: Soil velocity vectors from FE-analysis of a laterally loaded monopile at $5,3^\circ$ rotation with a pile top velocity, v , of 2,2 m/s. The failure mechanism geometry is indicated in the figure.

5.6 Discussion of Monopile Analyses

For the monopile pushover analyses some assumptions were made regarding the FE-model, and the model was not verified through a convergence study. However, results from the convergence study of the spudcan penetration FE-model was utilised when establishing the monopile model. The mesh density used in the monopile analyses is similar to the mesh density used in the spudcan analyses, and both analyses had similar dimensions. It is still possible that the FE-mesh is not sufficiently fine to give a convergent solution, but the main objective of the monopile pushover analyses is to study the effect of loading rate, not to accurately predict the lateral resis-

tance. Hence, it is not essential to have a mesh which can give a convergent solution. The radius of the soil domain was verified to be sufficiently large, but the height of the soil domain was not checked through a convergence study. However, as only lateral loading is considered and the soil domain extends $2D_p$ below the monopile toe, it is assumed that the soil domain height is sufficiently large to avoid boundary effects from the bottom boundary. This assumption is supported by the contour plot of stresses in Figure 5.6 which shows that the soil strength closer to the bottom boundary is mobilised in a small degree. The contours of ξ in Figure 5.7 also show that the plastic strains in the model is located far from the bottom boundary.

For the monopile analyses the coupled Eulerian-Lagrange (CEL) approach was used, which is capable of describing large deformations. Although, the soil deformations are not extensive in a monopile pushover analysis compared to e.g. soil deformations in spudcan penetration, and convectional Lagrangian FEA can be used to analyse lateral loading of monopiles. The reason that CEL was used in this case is to keep the monopile analyses similar to the spudcan analyses, such that the experience and the results from the spudcan modelling could be used in the monopile modelling. It is possible that more accurate results could be obtained with a Lagrangian analysis, since the tracking of state parameters when the material moves in the Eulerian mesh can introduce some inaccuracies.

In the FEAs, the soil stiffness was set to $200s_{ll}$, which can be considered to be a low stiffness. The soil stiffness should not have any significant influence on the rate effect in the analyses, as previously discussed. However, the soil stiffness governs the initial response of the monopile before a plastic failure mechanism has been established. Since a relatively low stiffness is used, the resistance in the initial elastic part on the monopile load-displacement curves, in Figure 5.5, is probably underestimated.

The plot of velocity vectors shows a failure mechanism where the pile rotates as a rigid body around a rotation centre above the toe. This monopile response to lateral loading is typical, as discussed in section 2.7, and is as expected since the pile was modelled as a rigid body. A passive earth pressure is mobilised in front of the pile and behind the monopile toe. This is similar to the failure mechanism obtained from small strain FE-analyses done by DNV, as shown in Figure 5.1. However, the analyses by DNV also show an active wedge falling onto the pile. This differs from the current analysis which has a pile-soil contact formulation which cannot transfer tensile stresses, and a high shear strength to withstand active wedge failure. Therefore, there is no active wedge falling onto the monopile. Thus, the analyses herein are for the case where a gap has formed behind the pile prior to the application of the lateral load, which prevents

suction forces to mobilise an active wedge behind the pile. This gap will then reduce the lateral resistance mobilised by the monopile as it cannot benefit from the tensile strength on the active side.

In the analyses, submerged weights are considered, and it is therefore assumed that the gap behind the pile is filled with water at all times during the analysis. This assumption seems valid for low loading rates. For larger loading rates the gap, which extends down to approximately 19 m below the seabed, will open in the matter of seconds. Then it is not certain there is enough time for water to flow into the gap, and it is possible that suction forces will develop. Such suction forces could contribute to increase the lateral resistance of monopiles for rapid loading. However, such suction forces and the influence of water flow is not investigated in this study.

The monopile is modelled as a solid rigid body to simplify the analysis. In reality the monopile has some flexibility, but for monopiles with a low L/D_p ratio they behave more or less like rigid. It is therefore assumed that this simplification will have little influence on the monopile response. Furthermore, in reality monopiles are often open ended hollow steel tubes, not solid. This can influence the failure mechanism around the pile toe, and the soil failure may go inside the monopile instead of around it. It is assumed that this simplification do not influence the conclusions that can be drawn on rate effects for monopiles to any significant degree. Furthermore, no dynamic inertia effects are included in the analyses. For low pile lateral velocities this may be a valid approach, but for larger velocities dynamic effects can be expected to influence the response. Especially, for the highest monopile top velocity considered herein of 2,2 m/s dynamic effects can be significant. In reality, there is also a more complicated system with a monopile and wind turbine with blades in contrast to the single pile system considered in the current analyses. However, the study of dynamic effects on a monopile-wind turbine system is beyond the scope of this thesis.

By considering different monopile pushover rates it was shown that strain rate effects give increased lateral resistance for increasing pushover rates. The increase in resistance was found to be between 11 and 16 % per log-cycle increase in loading rate. This agrees well with the typical 5-20 % strength increase per log-cycle increase in loading rate for clays. In the PISA pile load tests they observed rate effects with 8 and 33 % increase in resistance per log-cycle, a rather large span. However, 33 % came from an unintended less controlled test, and may therefore be less accurate. The rate effects herein are close to the lower 8 % increase found in the PISA project. Based on these comparisons, the observed rate effect in the current analyses seems reasonable.

In the FEAs, rate effect parameters for the UWA-model calibrated against spudcan penetration tests were used. In addition these rate effect parameters, when applied in an FE-model of a triaxial test, gave a similar rate effect as observed in physical triaxial tests, see Figure 2.4 and 3.5. As these UWA-rate effect parameters give a reliable rate effect for two different analysis types, it seems probable that they will give reliable rate effects for analyses of monopile lateral resistance. Since these parameters gave reasonable rate effects in the monopile analyses, this assumption is strengthened. The rate effect parameters were calibrated against spudcan tests done in the complex Dogger Bank clay, but also gave good agreement with empirical formulas based on triaxial tests done on Norwegian onshore clays. This may indicate that the used rate effect parameters are valid for other types of clay and not only for Dogger Bank clay, since the parameters give a rate effect similar to what is observed for other clays.

The analysis with a pile top velocity of 2,2 m/s was designed to replicate a ULS storm load case, where the pile is pushed to 5° rotation by a wave in 3 seconds, corresponding to a wave with a time period of 12 s. It was assumed that 5° rotation would mobilise the ultimate resistance of the soil. These assumptions were used to calculate the equivalent lateral pile top velocity of 2,2 m/s. This increased lateral velocity gave an increase in resistance of 35 % compared to the analysis with a slow velocity of 0,0017 m/s at 3° monopile rotation. Thus, rate effects may give significant increase in the ultimate lateral capacity of monopiles in clay. The resistances are compared at 3° rotation because for larger displacements the resistance in the analyses with lower velocities starts to reduce due to softening. If the rate effect is measured at larger displacements, the rate effect would be higher.

As a low soil stiffness is used, larger displacements are required to bring the soil to failure and to reach the ultimate capacity, and if a higher soil stiffness had been used, less displacement would be necessary to mobilise the ultimate resistance. Therefore, for a higher stiffness a lower lateral pile velocity would be required to reach the ultimate pile resistance during a storm wave. A lower velocity would result in less rate effects. Thus, the assumed low soil stiffness in the current analyses may have resulted in an overprediction of the rate effect for the considered ULS load case. On the other hand, cyclic degradation effects from previous wind and wave loading have not been accounted for in the current analyses. Cyclic degradation effects may reduce the soil stiffness to a lower value. Moreover, if the pushover rate is approximately halved there is still a significant increase in resistance of about 26 %. Furthermore, cyclic degradation effects on the soil strength has not been accounted for either. In general, cyclic effects can be expected to lower the overall capacity of a monopile, but rate effects are still likely to increase the capacity.

The monopile pushover analyses included strain softening effects. The strain softening in the soil was modest compared to the softening in the spudcan analyses. For the monopile analysis the soil deforms to a lesser degree and a smaller area close to the monopile softens, whereas for the spudcan analyses much of the soil around the spudcan experiences large deformations and becomes fully softened. Hence, softening is less important for the monopile response to lateral loading, and the known uncertainty in the used softening parameters is assumed to be of little importance for the results.

As shown above strain rate effects may increase the ultimate lateral capacity of monopiles, and this is demonstrated for a realistic load case for the North Sea using monopile dimensions considered for the Dogger Bank wind farm. Although there are uncertainties associated to the applied load case, lower loading rates have shown a significant rate effect. Thus, rate effects can be expected to give a significant increase in capacity in the ULS. Further research is needed to accurately quantify the rate effect for laterally loaded monopiles. This increased resistance can be utilised in monopile design when dimensioning in the ultimate limit state for loading types with a short duration, for example wave loads. This may result in a shorter embedment depth of the monopile with less steel usage. A relatively low reduction in necessary embedment depth for a single pile can give considerable financial savings when considering a larger offshore wind park with for example 100 wind turbines.

5.7 Summary of Monopile Analyses

In the monopile pushover analyses, Abaqus\Explicit was used with the coupled Eulerian-Lagrange approach and the UWA soil model to account for strain softening and rate effects. The objective of the analyses was to quantify strain rate effects for laterally loaded monopiles. The strain softening and rate parameters were calibrated against spudcan penetration tests, and the rate parameters were also verified against an empirical rate effect formulation. The monopile FE-model was investigated and it is concluded that the FE-model can give sufficiently accurate results when considering the objective of the model.

The finite element analyses set out to simulate a load case where a storm wave pushes over the monopile, mobilising the ultimate lateral capacity of the soil, during one wave. The specific load case and monopile parameters were chosen based on realistic data from the Dogger Bank Offshore Wind Farm gained from communication with DNV. The geotechnical parameters were taken from location DBB-JU1 at Dogger Bank, one of the locations used for spudcan penetration

tests and back-calculations.

Some simplifications were made during the modelling. The monopile was modelled as a rigid body and cyclic degradation effects and dynamic inertia effects were not included in the analyses. The stiffness of the soil was set to a relatively low value which may have given an inaccurate initial response for the monopile before a failure mechanism has developed. Furthermore, it is assumed that a water filled gap has already formed behind the pile prior to the load application, and no effects of water flow around the pile are included. However, it is assessed that these simplifications do not have a significant effect on the relative loading rate effect in the analyses.

The monopile pushover analyses succeed in modelling strain rate effects, and they showed that strain rate effects gave between 11 and 16 % increase in resistance per \log_{10} -cycle increase in loading rate. This rate effect is in agreement with typical rate effects for clays, and in agreement with observed rate effects for laterally loaded piles in the PISA project. For the considered ultimate limit state load case, rate effects gave an increase of approximately 35 % in lateral resistance for the monopile, whereas halving the loading rate results in an increase of approximately 26 %. Thus, loading rates in a ULS case can give a significant increase in capacity. Further research with other monopile designs and load cases are needed for accurate predictions of the rate effect on lateral capacity of monopiles for practical applications. Incorporating rate effects in monopile design can give significant cost savings for a wind farm project.

Chapter 6

Summary and Recommendations for Further Work

6.1 Thesis Summary

This thesis has investigated the effect of loading rate on the lateral capacity of monopiles by using finite element analyses (FEAs) with a soil model capable of describing strain rate and softening effects. This study has evolved around the Dogger Bank Offshore Wind Park, and to study rate effects for monopiles, measurements from penetration tests with large spudcan foundations have been utilised. Back calculations of spudcan penetration tests were carried out using Abaqus\Explicit with the coupled Eulerian-Lagrange (CEL) approach which can describe large deformations without suffering large mesh distortions with accompanying problems. Hence, the complete penetration process could be modelled in one analysis.

To account for strain softening and rate effects, the so-called UWA soil model is used in the FEAs. The implementation of the UWA-model together with the CEL approach was verified by simulating a triaxial compression test, and it was concluded that strain softening and rate effects worked as expected. Furthermore, the use of a normalised loading rate to account for the real loading rate was verified. In addition, rate effect parameters calibrated against spudcan penetration tests were found to give a rate effect similar to rate effects observed in physical triaxial tests when applied to a finite element (FE) model of a triaxial test.

Spudcan penetration tests from location DBB-JU1 and DBC-JU1, both located in the Dogger Bank wind farm, was analysed. The penetration tests included tests with normal and faster pen-

etration rates, and the observed increase in resistance due to loading rate was close to typical rate effects for clays found in literature. To establish geotechnical parameters, CPT and laboratory data was used. There were some variability in resistance and penetration rate between individual tests at each location. This made interpretation of results more challenging.

The spudcan tests were used to calibrate strain softening and rate effect parameters for the UWA-model, and to determine the shear strength of the soil through back-calculation of the measured penetration resistance. The calibration was done against measurements from location DBB-JU1 and verified to give a satisfactory prediction of penetration resistance at location DBC-JU1. The back-calculations were able to give penetration resistance in reasonable agreement with measured resistance for both slower and faster penetration rates. The softening and strength parameters were difficult to calibrate from the available data, but a combination of parameters which gave satisfactory results was established. Furthermore, the strength and softening parameters were found to be less important for the monopile pushover analyses.

The back calculated rate effect parameters resulted in parameters which are considerably higher than parameters calibrated against an empirical based rate effect formula. However, the high rate effect parameters performed well for spudcan penetration and triaxial tests in FE-analyses. The reason that seemingly high rate effect parameters were needed to model a reliable rate effect is uncertain. The evolution of the spudcan failure mechanism during the penetration was investigated and generally behaved as predicted in the literature.

An FE-model for monopile pushover analyses was established using a similar methodology as for the spudcan analyses to investigate rate effects on monopile lateral capacity. The considered soil profile is similar to that of DBB-JU1, and the monopile dimensions were chosen to resemble a monopile at the Dogger Bank wind farm. Some simplifications were made in the modelling, but these simplifications should not have a significant effect on the rate effects in the analyses. However, a low soil stiffness was used which made the initial response less correct, and may have led to an overprediction of the rate effect in the considered ultimate limit state (ULS) load case. Reduction of soil strength and stiffness due to cyclic degradation effects was not considered in this study, but such effects should be considered if the current results are to be used in the industry.

The monopile pushover analyses consist of an embedded monopile which is pushed over at different rates. The fastest pushover rate was chosen to resemble the ULS load case where one single storm wave pushes over the monopile and mobilises the ultimate lateral resistance.

In addition slow and intermediate loading rates were analysed to quantify the relative rate effect. The ULS load case gave an increase in resistance of approximately 35 % when compared to the slowest loading rate, corresponding to an almost static load. In general an increase in resistance of between 11 and 16 % per \log_{10} -cycle of increase in loading rate was observed in the FE-analyses. This is within the range of the rate effect observed in the PISA lateral load tests performed in clay similar to Dogger Bank. It is worth noting that the magnitude of the rate effect observed in the current study for the ULS case is associated with some uncertainty, due to the low stiffness used and assumptions made in the implementation of the ULS case. However, if the loading rate in the ULS case was approximately halved the resistance would still increase with 26 %. Thus, the results indicates that there is significant rate effects which can be utilised in design in the ultimate limit state, despite the uncertainties in the analyses.

The main objective for this thesis was to quantify loading rate effects on the lateral capacity of wind turbine supporting monopiles, and investigate if rate effects can increase the lateral capacity in the ultimate limit state. The thesis has been able to analyse rate effects for monopiles, and found a rate effect within the range from previous research. Furthermore, the relative rate effect presented in the current results has less variability than results found in the literature. The current results indicate that monopile lateral capacity in the ULS can be significantly increased when accounting for loading rate effects. This may lead to shorter monopile design and significant financial savings for an offshore wind project.

6.2 Recommendations for Further Work

There are several topics that have not been included in this thesis and which require further research. This study has investigated strain rate effects for Dogger Bank clay, and further investigation is needed to verify if the current results are applicable to monopiles in other clays. Furthermore, rate effects for other soil materials like sand and the effect of soil layering need to be studied. As the mobilisation of the soil strength varies with depth for a laterally loaded pile, different layering configurations may affect the loading rate effect in different ways.

More knowledge about rate effects on monopile capacity can be obtained from field tests where monopiles are loaded with different rates, like in the PISA tests. This would give more confident results than FEA, and could be used to corroborate FEA. More spudcan tests or other loading tests with varying loading rate could also be used to gain more knowledge about rate effects for large foundations.

The current analysis methodology and rate effect parameters can be used to study other geotechnical problems involving high loading rates. For example installation of torpedo anchors. The current results could also be compared to existing studies on the effect of loading rate in geotechnical problems, which might give more general information on rate effects.

This study has not used rate effects measured in laboratory testing since laboratory strength determination has proven difficult for Dogger Bank clay. But rate effect measurements from lab could be used to study rate effects for monopiles at other locations. How the effect of cyclic degradation on the soil may influence loading rate effects should be studied to check if the relative rate effect found in the current study is valid when accounting for cyclic degradation.

The current FE-analyses employed the coupled Eulerian-Lagrange (CEL) method which can describe large deformations. CEL is not necessarily needed for monopile pushover analyses, and more common Lagrangian finite element methods can possibly provide better accuracy. Moreover, the current monopile FE-model was not verified with a convergence study. Therefore, the monopile analyses should be checked with a verified Lagrangian FE-model. Furthermore, spurious mesh dependency can be a problem for FEA including strain softening effects. More thorough assessments of whether this effect may have affected current results would be beneficial.

The convergence study showed that the current spudcan penetration FE-model could be further optimised, and the convergence study did not include softening and rate effects. The results of the current spudcan back-analyses should be checked with an optimised FE-model to verify the material parameter calibration. Future spudcan analyses could use a more refined mesh, and include softening and rate effects in the convergence study.

Dynamic effects have not been considered in the current study, and a rigid body simplification was used for the monopile. Further research should investigate if the dynamic effects of a monopile - wind turbine system can influence loading rate effects. Furthermore, it should be verified if a correct structural model of the monopile will give the same rate effects as currently obtained for a rigid body monopile. The current analyses have assumed that a gap has formed on the active side of the monopile prior to the load application. The effect of a gap opening behind the pile with possible water flow into the gap and the development of suction forces should be checked. Soil tensile strength may further increase the resistance for rapid loading. This study has only considered rate effects for the plastic soil response, and further research can investigate if strain rate effects can give higher strength and stiffness to the elastic soil response.

To give more accurate predictions of rate effects for laterally loaded monopiles, other analyses with different monopile designs and loading conditions need to be evaluated. Then, with further research into this topic, rate effects can be incorporated into industry practises, e.g into p - y curves for monopiles, and be used to optimise monopile design in future offshore wind projects.

Bibliography

Abaqus (2019). Abaqus version R2019x User's Manuals. Dassault Systèmes.

Belytschko, T., W. K. Liu, B. Moran, and K. I. Elkhodary (2014). *Nonlinear Finite Elements for Continua and Structures*, 2nd Edition. USA, Beaverton: John Wiley & Sons, Ltd. ISBN: 978-1-118-63270-3.

Byrne, B. W., R. A. McAdam, H. J. Burd, W. J. A. P. Beuckelaers, K. G. Gavin, G. T. Houlsby, et al. (2020). Monotonic laterally loaded pile testing in a stiff glacial clay till at Cowden. *Géotechnique*, 70(11), 970–985. DOI: [10.1680/jgeot.18.pisa.003](https://doi.org/10.1680/jgeot.18.pisa.003).

Casacrande, A. and S. D. Wilson (1951). Effect of Rate of Loading on the Strength of Clays and Shales at Constant Water Content. *Géotechnique*, 2(3), 251–263. DOI: [10.1680/geot.1951.2.3.251](https://doi.org/10.1680/geot.1951.2.3.251).

Chatterjee, S., M. Randolph, and D. White (2012). The effects of penetration rate and strain softening on the vertical penetration resistance of seabed pipelines. *Géotechnique*, 62(7), 573–582. DOI: [10.1680/geot.10.p.075](https://doi.org/10.1680/geot.10.p.075).

Chopra, A. K. (2012). *Dynamics of structures : theory and applications to earthquake engineering*. 4th ed. Boston, Massachusetts: Prentice Hall. ISBN: 0132858037.

Cotterill, C., E. Phillips, L. James, C.-F. Forsberg, and T. I. Tjelta (2017a). How understanding past landscapes might inform present-day site investigations: a case study from Dogger Bank, southern central North Sea. *Near Surface Geophysics*, 15(4), 403–414. DOI: [10.3997/1873-0604.2017032](https://doi.org/10.3997/1873-0604.2017032).

Cotterill, C. J., E. Phillips, L. James, C. F. Forsberg, T. I. Tjelta, G. Carter, et al. (2017b). The evolution of the Dogger Bank, North Sea: A complex history of terrestrial, glacial and marine environmental change. *Quaternary Science Reviews*, 171, 136–153. DOI: [10.1016/j.quascirev.2017.07.006](https://doi.org/10.1016/j.quascirev.2017.07.006).

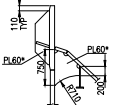
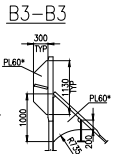
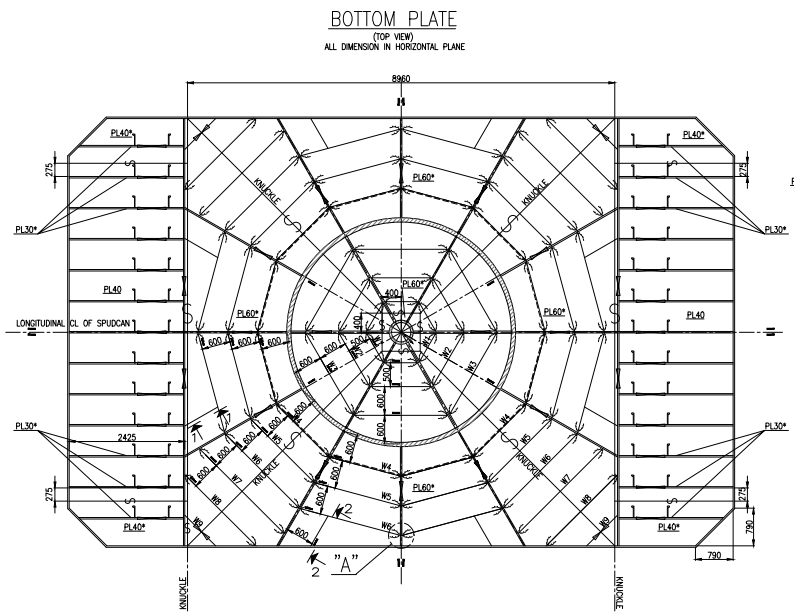
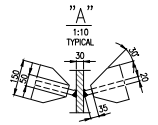
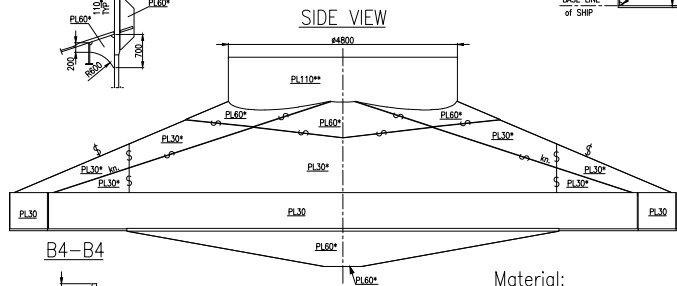
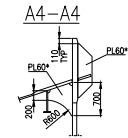
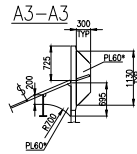
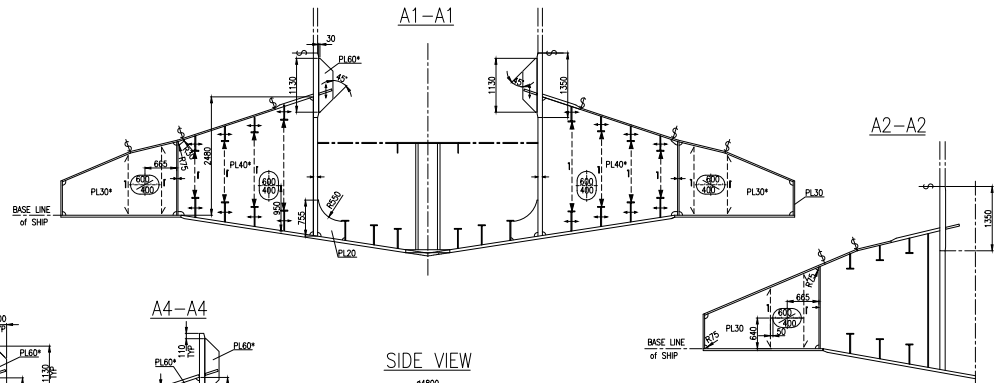
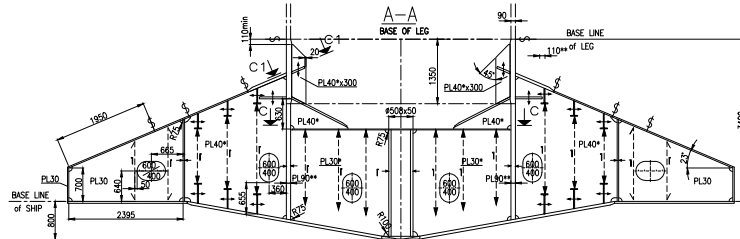
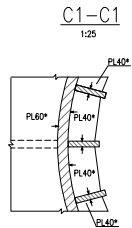
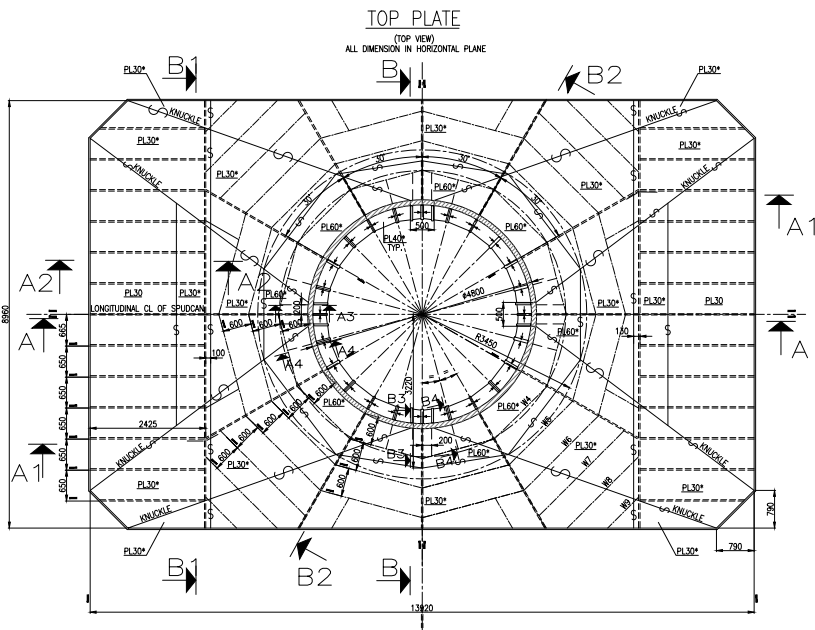
- Dayal, U. and J. H. Allen (1975). The Effect of Penetration Rate on the Strength of Remolded Clay and Sand Samples. *Canadian Geotechnical Journal*, 12(3), 336–348. DOI: [10.1139/t75-038](https://doi.org/10.1139/t75-038).
- Dean, E. T. (2008). Consistent preload calculations for jackup spudcan penetration in clays. *Canadian Geotechnical Journal*, 45(5), 705–714. DOI: [10.1139/t07-108](https://doi.org/10.1139/t07-108).
- DNV GL (2018). DNVGL-ST-0126: Support structures for wind turbines. Standard.
- DNV GL (2019). DNVGL-RP-C212: Offshore soil mechanics and geotechnical engineering. Recommended practice.
- DNV GL (2020). Back-analysis of Jacking Trials. Report No.: 2019-1293, Rev. 1.
- Dogger Bank Wind Farm (2021). *SSE Renewables, Equinor and Eni*. URL: <https://doggerbank.com>.
- Dutta, S., B. Hawlader, and R. Phillips (2015). Finite element modeling of partially embedded pipelines in clay seabed using Coupled Eulerian–Lagrangian method. *Canadian Geotechnical Journal*, 52(1), 58–72. DOI: [10.1139/cgj-2014-0045](https://doi.org/10.1139/cgj-2014-0045).
- Equinor (2020). Dogger Bank Jacking Trials 2020. Experience Report. Dated 2020-08-10, Rev. 1 / Draft.
- Herschel, W. and R. Bulkley (1926). Measurement of consistency as applied to rubber-benzene solutions. *Am. Soc. Test Proc.* Vol. 26. 2, 621–633.
- Hossain, M. S. and M. F. Randolph (2009a). Effect of Strain Rate and Strain Softening on the Penetration Resistance of Spudcan Foundations on Clay. *International Journal of Geomechanics*, 9(3), 122–132. DOI: [10.1061/\(asce\)1532-3641\(2009\)9:3\(122\)](https://doi.org/10.1061/(asce)1532-3641(2009)9:3(122)).
- Hossain, M. S. and M. F. Randolph (2009b). New Mechanism-Based Design Approach for Spudcan Foundations on Single Layer Clay. *Journal of Geotechnical and Geoenvironmental Engineering*, 135(9), 1264–1274. DOI: [10.1061/\(asce\)gt.1943-5606.0000054](https://doi.org/10.1061/(asce)gt.1943-5606.0000054).
- Huynh, D. V. K., H. P. Jostad, and H. K. Engin (2019). Improvement of NT-bar Evaluation in Clays Using Large Deformation FE Method. *Proceedings of the 1st Vietnam Symposium on Advances in Offshore Engineering*. Springer Singapore, 137–143. DOI: [10.1007/978-981-13-2306-5_17](https://doi.org/10.1007/978-981-13-2306-5_17).
- ISO (2016). Petroleum and natural gas industries — Site-specific assessment of mobile offshore units — Part 1: Jack-ups. Standard ISO 19905-1:2016. Geneva, Switzerland: International Organization for Standardization. URL: <https://www.iso.org/standard/68135.html>.

- Jan De Nul (2020). Jacking Report. Dogger Bank Offshore Windfarms. JdN document No.: JDN-6723-JRE-JT-001, Rev 2.
- Kim, Y., M. Hossain, D. Wang, and M. Randolph (2015). Numerical investigation of dynamic installation of torpedo anchors in clay. *Ocean Engineering*, 108, 820–832. DOI: [10.1016/j.oceaneng.2015.08.033](https://doi.org/10.1016/j.oceaneng.2015.08.033).
- Kvalstad, T., F. Nadim, and C. Arbitz (2001). Deepwater Geohazards: Geotechnical Concerns and Solutions. Houston: Proc., Offshore Technology Conf. DOI: [10.4043/12958-ms](https://doi.org/10.4043/12958-ms).
- Lunne, T. and K. Andersen (2007). Soft Clay Shear Strength Parameters For Deepwater Geotechnical Design. *Proc., 6th Int. Offshore Site Investigation and Geotechnics Conf.: Confronting New Challenges and Sharing Knowledge*, 151–176.
- Lunne, T., P. Robertson, and J. Powell (1997). Cone penetration testing in geotechnical practice. London: Blackie. Chap. 5.4.2, p. 66. ISBN: 0751403938.
- Marsland, A. (1972). Clays subjected to in situ plate tests. *Ground Engineering*, 5(6), 24–31.
- Meyerhof, G. G. (1983). Scale Effects of Ultimate Pile Capacity. *Journal of Geotechnical Engineering*, 109(6), 797–806. DOI: [10.1061/\(asce\)0733-9410\(1983\)109:6\(797\)](https://doi.org/10.1061/(asce)0733-9410(1983)109:6(797)).
- NGI (2016). Dogger Bank Creyke Beck B – Geotechnical Design Basis. Geotechnical Parameters Report. Document No.: 20150552-01-R, Rev 0.
- NGI (2020a). Dogger Bank B Offshore Wind Farm. Geotechnical Interpretation Report. Document No.: 20200151-03-R, Rev 0.
- NGI (2020b). Dogger Bank B Offshore Wind Farm. Spudcan Penetration Back-Analyses. Document No.: 20200151-04-R, Rev 0.
- Qiu, G., S. Henke, and J. Grabe (2011). Application of a Coupled Eulerian–Lagrangian approach on geomechanical problems involving large deformations. *Computers and Geotechnics*, 38(1), 30–39. DOI: [10.1016/j.compgeo.2010.09.002](https://doi.org/10.1016/j.compgeo.2010.09.002).
- Randolph, M. and S. Gourvenec (2011). *Offshore Geotechnical Engineering*. Taylor & Francis Group. ISBN: 9780415477444.
- Sandven, R., K. Senneset, A. Emdal, S. Nordal, N. Janbu, L. Grande, et al. (2017). *Geotechnics. Field and Laboratory Investigations. Compendium*. NTNU Geotechnical division.
- Stylegar, F. A. and S. Askheim (2018). Nordsjøfastlandet. *Store norske leksikon*. URL: <https://snl.no/Nordsj%C3%B8fastlandet>.

- Tho, K. K., C. F. Leung, Y. K. Chow, and S. Swaddiwudhipong (2012). Eulerian Finite-Element Technique for Analysis of Jack-Up Spudcan Penetration. *International Journal of Geomechanics*, 12(1), 64–73. DOI: [10.1061/\(ASCE\)GM.1943-5622.0000111](https://doi.org/10.1061/(ASCE)GM.1943-5622.0000111).
- Tseng, C.-C. and S.-L. Lee (2017). Closed-form designs of digital fractional order Butterworth filters using discrete transforms. *Signal Processing*, 137, 80–97. DOI: [10.1016/j.sigpro.2017.01.015](https://doi.org/10.1016/j.sigpro.2017.01.015).
- Wahl, M. M. (2020). Spudcan Penetration at Dogger Bank. Comparing Jacking Trials with Calculations. Project thesis. The Norwegian University of Science and Technology.
- WindEurope (2021). Offshore Wind in Europe - Key trends and statistics 2020. WindEurope asbl/vzw.
- Worren, A. (2013). Finite Element Analyses of Spudcan Penetration Using CEL Method. Master's thesis. The Norwegian University of Science and Technology. URL: <http://hdl.handle.net/11250/237392>.
- Zdravković, L., R. J. Jardine, D. M. G. Taborda, D. Abadias, H. J. Burd, B. W. Byrne, et al. (2020a). Ground characterisation for PISA pile testing and analysis. *Géotechnique*, 70(11), 945–960. DOI: [10.1680/jgeot.18.pisa.001](https://doi.org/10.1680/jgeot.18.pisa.001).
- Zdravković, L., D. M. G. Taborda, D. M. Potts, D. Abadias, H. J. Burd, B. W. Byrne, et al. (2020b). Finite-element modelling of laterally loaded piles in a stiff glacial clay till at Cowden. *Géotechnique*, 70(11), 999–1013. DOI: [10.1680/jgeot.18.pisa.005](https://doi.org/10.1680/jgeot.18.pisa.005).
- Zhou, H. and M. F. Randolph (2007). Computational Techniques and Shear Band Development for Cylindrical and Spherical Penetrometers in Strain-Softening Clay. *International Journal of Geomechanics*, 7(4), 287–295. DOI: [10.1061/\(ASCE\)1532-3641\(2007\)7:4\(287\)](https://doi.org/10.1061/(ASCE)1532-3641(2007)7:4(287)).
- Zhu, H. and M. F. Randolph (2011). Numerical analysis of a cylinder moving through rate-dependent undrained soil. *Ocean Engineering*, 38(7), 943–953. DOI: [10.1016/j.oceaneng.2010.08.005](https://doi.org/10.1016/j.oceaneng.2010.08.005).

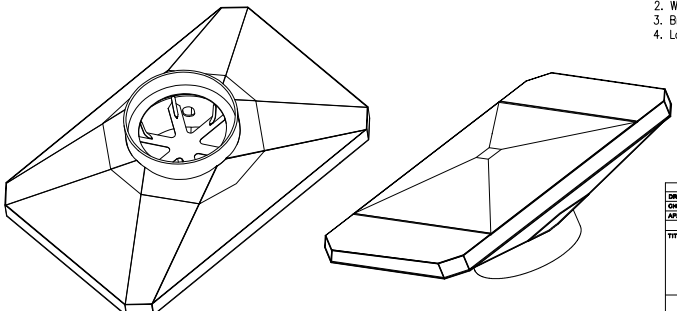
Appendix A

Spudcan Drawing



TOP 3D VIEW

BOTTOM 3D VIEW



Material:
Material to be H36 steel certified by DNV U.N.O.
* - Means extra strength steel 550
** - Means extra strength steel 690
Grade of steel acc. NB130/203-002

- Notes:**
1. Structural details acc. "Catalogue of typical hull structural elements K-100"
 2. Welds acc. NB130/203-042-1 "WELDING TABLE-OFFSHORE STRUCTURE", U.N.O.
 3. Brackets acc. Brackets Table NB130/235-002
 4. Lamination testing region indicated as

DATE	NAME
2013.06.14	R.S.
2013.06.20	M.L.
2013.06.20	T.P.

StoGda
SHIP DESIGN & ENGINEERING

CRIST
PROJECT #17403-00

NB130

TITLE
SELF-ELEVATING WIND TURBINE INSTALLATION UNIT
SPUD CAN STRUCTURE

DATE	SCALE	SIZ	AREA	ARCHIVE	DRAWING NO.	SHEET	TOTAL SHEETS
2013.06.20	1:50	A1			NB130/323-001-1-ACO	1	2

This document must not be reproduced and published without the StoGda's permission

Appendix B

Soil Data

s_u- and *q_t*-profiles

Table B.1: Design q_t -profile for location DBB-JU1

Depth below seabed [m]	q_t -design [kPa]
1	1250
2	1350
4	1610
6	1850
8	2100
10	2450
12	2500
14	2700
15	2800
16	2700
18	2750
20	3250
27	3500
32	3500
48	6500

Table B.2: Shear strength profile used in the convergence study

Depth below seabed [m]	s_u [kPa]
1	59.5
2	64.3
4	76.7
6	88.1
8	100.0
10	116.7
12	119.0
14	128.6
15	133.3
16	107.1
18	131.0
20	154.8
27	166.7
30	166.7

Table B.3: The s_u -profile adopted for some FE-analyses and the correct s_u -profile at DBB-JU1.

Adopted in fig. 4.7(a) and fig. 4.8(a)		Design qt-profile, $N_{kt}^* = 23$	
Depth below seabed [m]	s_u [kPa]	Depth below seabed [m]	s_u [kPa]
1	54.3	1	53.5
2	58.7	2	57.0
4	70.0	4	66.7
6	80.4	6	75.5
8	91.3	8	84.7
10	106.5	10	98.3
12	108.7	12	98.8
14	117.4	14	105.8
15	121.7	15	109.3
16	117.4	16	104.2
18	119.6	18	104.7
20	141.3	20	124.8
27	152.2	27	129.9
32	152.2	32	125.7

Appendix C

Miscellaneous Plots

Comparing filtered and unfiltered load-penetration response

Initial stresses in monopile analysis

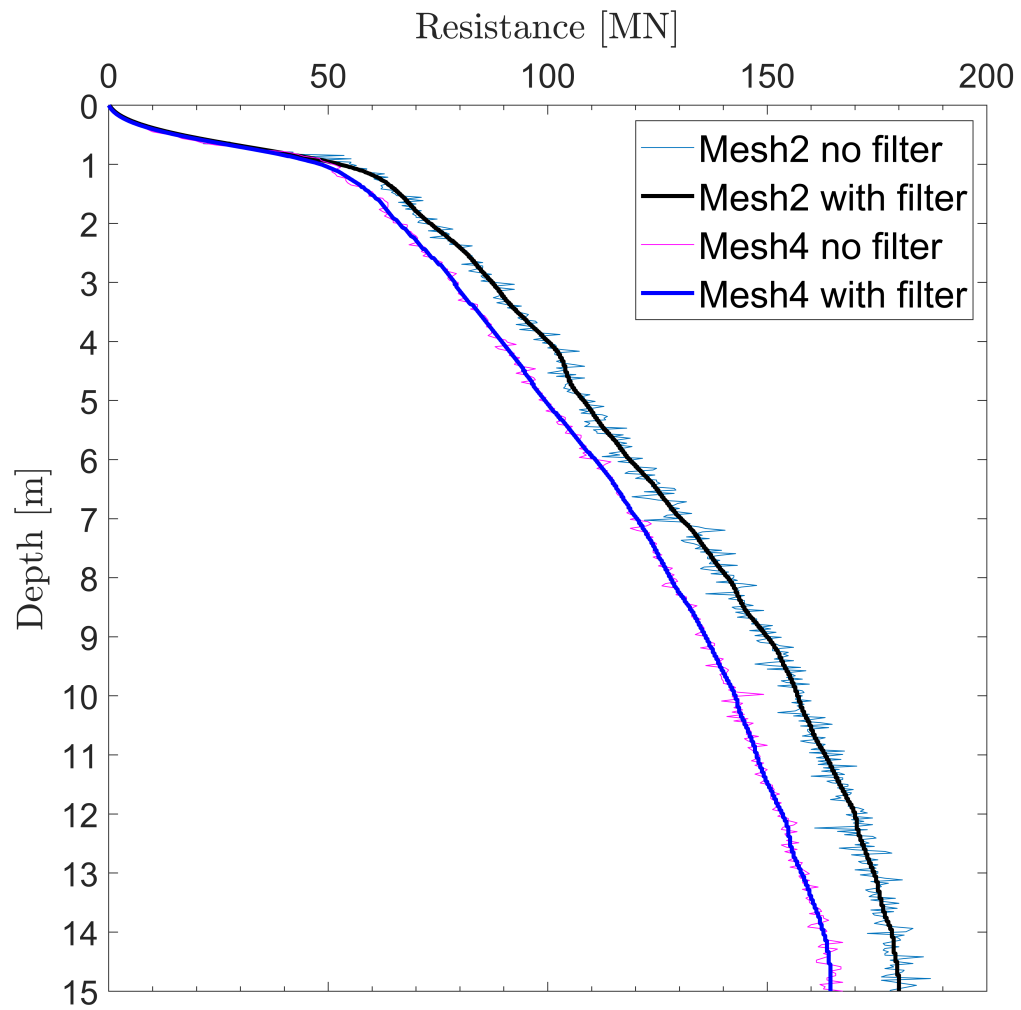


Figure C.1: Comparison of filtered and unfiltered load-penetration response for analysis Mesh1 and Mesh4 conducted in the convergence study. The Butterworth filter is used.

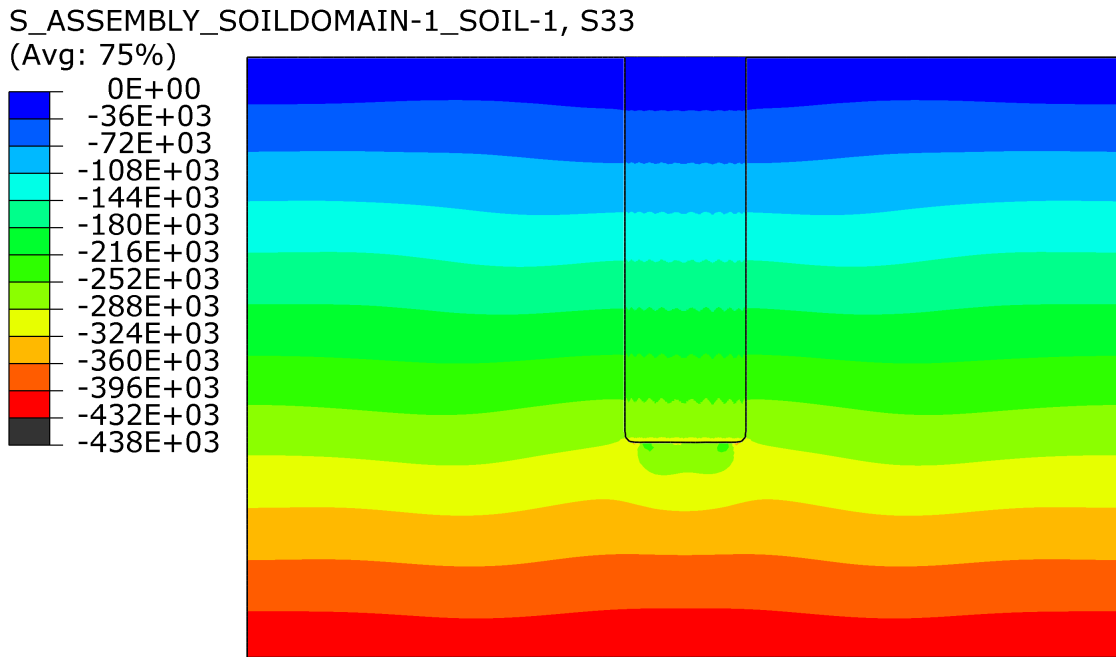


Figure C.2: Initial stresses in monopile pushover FE-analysis. Contours are showing effective vertical stress, σ'_v , in Pa. The monopile is hidden.

